Title
Sub-wavelength resonant structures at microwave and optical frequencies

Permalink
https://escholarship.org/uc/item/3th147ss

Author
Simić, Aleksandar

Publication Date
2011

Peer reviewed|Thesis/dissertation

UNIVERSITY OF CALIFORNIA, SAN DIEGO

Sub-Wavelength Resonant Structures at Microwave and Optical Frequencies

A dissertation submitted in partial satisfaction of the
requirements for the degree
Doctor of Philosophy

in

Physics

by

Aleksandar Simić

Committee in charge:

Professor Yeshaiahu Fainman, Chair
Professor Sheldon Schultz, Co-Chair
Professor Leonid V. Butov
Professor Vitaliy Lomakin
Professor Clifford M. Surko

2011

The dissertation of Aleksandar Simić is approved, and it is acceptable in quality and form for publication on microfilm and electronically:

Co-Chair

Chair

University of California, San Diego

2011

DEDICATION

To my children Ekatarina and Nikola, and my wife Blaženka.

I am *so* happy to have you.

EPIGRAPH

The important thing is
not to stop questioning.
— Albert Einstein

TABLE OF CONTENTS

LIST OF FIGURES

LIST OF TABLES

ACKNOWLEDGEMENTS

There are many people who selflessly helped and supported me along this academic journey. Without their kindness, encouragement and help, this dissertation would remain but a dream. First, I would like to thank my adviser Prof. Yeshaiahu Fainman for giving me the time, space and resources I needed for this work. I am truly grateful for your trust and for giving me free reign in the lab. Without that, I would not be the experimentalist I am today.

I would also like to thank my co-adviser, Prof. Sheldon Schultz for teaching me to trust my intuition in physics. The ability to, for a short time, witness your incredible insight and pick a few of your pearls of wisdom was a priceless gift to me. Thank you. I also want to thank other members of the Schultz Group, David Vier and Roger Isaacson for their support and encouragement.

To my fellow members of the Uno Group, without you this process would have been infinitely harder and a lot less fun. Thank you for being there to share both the joys and the frustrations of grad student life. Thank you for all the things you taught me and all the opportunities you gave me to teach you. Through this communication of ideas my scientific understanding improved immensely. Above all, your friendship is something that will stay with me forever.

Thank you to my friends and colleagues at Physics and Electrical Engineering departments. Knowing you, and having you in my life made me a better person.

Lastly, I want to thank my family for supporting me every step of this long, and at times difficult, journey. Thank you for believing in me and for giving me the strength to carry on when I had my moments of doubt and pain. Thank you for being kind loving and considerate. I would have never persevered in this endeavor if it wasn't for you and your selfless support.

This dissertation was prepared with LaTeX using the unofficial UCSD Doctoral Dissertation Template (`http://ucsd-thesis.googlecode.com`).

Chapter 2, in part, is a reprint of the material as it appears in "Experimental confirmation of negative phase change in negative index material planar samples," D. Vier, D. R. Fredkin, A. Simic, S. Schultz, and M. Tanielian, *Applied Physics*

Letters, vol. 86, no. 24, p. 241908, 2005. The dissertation author was the primary co-investigator and coauthor of this paper.

Chapter 3, in full, is a reprint of the material as it appears in "Room-temperature subwavelength metallo-dielectric lasers," M. Nezhad, A. Simic, O. Bondarenko, B. Slutsky, A. Mizrahi, L. Feng, V. Lomakin, and Y. Fainman, *Nature Photonics*, vol. 4, no. 6, pp. 395–399, 2010. The dissertation author was the primary co-investigator and coauthor of this paper.

Chapter 5, in full, is a reprint of the material as it appears in "Wafer bonded subwavelength metallo-dielectric laser," O. Bondarenko, A. Simic, Q. Gu, J. H. Lee, B. Slutsky, M. P. Nezhad, and Y. Fainman, *IEEE Photonics Journal*, vol. 3, no. 3, pp. 608–616, 2011. The dissertation author was the primary co-investigator and coauthor of this paper.

Chapter 6, in full, has been submitted for publication of the material as it may appear in "Thresholdless Nanoscale Coaxial Lasers," M. Khajavikhan, A. Simic, M. Katz, J. H. Lee, B. Slutsky, A. Mizrahi, V. Lomakin and Y. Fainman, *Nature*. The dissertation author was the primary co-investigator and coauthor of this paper.

VITA

2004	B.S. in Physics *summa cum laude*, San Diego State University
2006	M.S. in Physics, University of California, San Diego
2011	Ph.D. in Physics, University of California, San Diego

PUBLICATIONS

D. Vier, D. R. Fredkin, A. Simic, S. Schultz, and M. Tanielian, "Experimental confirmation of negative phase change in negative index material planar samples," *Applied Physics Letters*, vol. 86, no. 24, p. 241908, 2005.

M. Nezhad, A. Simic, O. Bondarenko, B. Slutsky, A. Mizrahi, L. Feng, V. Lomakin, and Y. Fainman, "Room-temperature subwavelength metallo-dielectric lasers," *Nature Photonics*, vol. 4, no. 6, pp. 395–399, 2010.

S. Zamek, A. Mizrahi, L. Feng, A. Simic, and Y. Fainman, "On-chip waveguide resonator with metallic mirrors," *Optics letters*, vol. 35, no. 4, pp. 598–600, 2010.

O. Bondarenko, A. Simic, Q. Gu, J. H. Lee, B. Slutsky, M. P. Nezhad, and Y. Fainman, "Wafer bonded subwavelength metallo-dielectric laser," *IEEE Photonics Journal*, vol. 3, no. 3, pp. 608–616, 2011.

F. Gholami, S. Zlatanovic, A. Simic, L. Liu, D. Borlaug, N. Alic, M. Nezhad, Y. Fainman, and S. Radic, "Third-order nonlinearity in silicon beyond 2,350 nm," *Applied Physics Letters*, vol. 99, p. 081102, 2011.

M. Nezhad, O. Bondarenko, M. Khajavikhan, A. Simic, and Y. Fainman, "Etch-free low loss silicon waveguides using hydrogen silsesquioxane oxidation masks," *Optics Express*, vol. 19, no. 20, pp. 18827–18832, 2011.

J. H. Lee, M. Khajavikhan, A. Simic, Q. Gu, O. Bondarenko, B. Slutsky, M. P. Nezhad and Y. Fainman, "Electrically pumped sub-wavelength metallodielectric pedestal pillar lasers," *Optics Express*, vol. 19, no. 22, pp. 21524–21531, 2011.

M. Khajavikhan, A. Simic, M. Kats, J. H. Lee, B. Slutsky, A. Mizrahi, V. Lomakin and Y. Fainman, "Thresholdless Nanoscale Coaxial Lasers" *Nature* (submitted)

ABSTRACT OF THE DISSERTATION

Sub-Wavelength Resonant Structures at Microwave and Optical Frequencies

by

Aleksandar Simić

Doctor of Philosophy in Physics

University of California, San Diego, 2011

Professor Yeshaiahu Fainman, Chair
Professor Sheldon Schultz, Co-Chair

Sub-wavelength scale resonant structures have been at the forefront of physics and engineering in the past decade. They offer a path for creation of new materials and great advancements in the field of photonics. This dissertation deals with design, fabrication and characterization of sub-wavelength resonant structures. In the first part, we investigate the application of passive sub-wavelength resonators in meta-materials — materials that have electromagnetic properties otherwise unattainable in nature. We develop a technique for characterization of negative index meta-materials by free-space measurement of the phase change in the meta-material. We also discuss the application of sub-wavelength resonators to highly efficient antenna design.

In the second part of the dissertation we focus on active sub-wavelength resonant structures, specifically nanolasers. We present a first truly sub-wavelength nanolaser operating at the room temperature and later investigate cryogenic operation of this laser design. We also offer a new, highly compatible, fabrication approach that could enable the integration of nanolasers in various silicon photonic devices. Lastly, we show a coaxial nanolaser that offers some new and truly unique features. For one it is the first sub-wavelength laser that operates at continuous wave at room temperature. More importantly, it exhibits single mode, thresholdless lasing at cryogenic temperatures. We discuss the significance and the implications of these results.

Chapter 1

Introduction

1.1 Sub-wavelength scale resonators

Resonance is a fundament concept in physics, studied and analyzed from the times of Galileo onward [1]. It occurs in all types of waves (be it mechanical, acoustic, electromagnetic, etc.) and it manifests itself by the increased amplitude of said waves at particular (resonant) frequency. From a quantum mechanical point of view, resonance is ubiquitous because of de Broglie's relation [2] and particle–wave duality. In this dissertation however, we limit ourselves to the discussion of electromagnetic resonance (in particular optical resonance in later chapters) and manmade structures that facilitate this resonance, i.e. resonators. Furthermore, we limit our discussion to the resonators whose physical size is smaller then their resonant wavelength ($\lambda = c/\nu$ where c is the speed of light, λ wavelength and ν frequency).

1.1.1 Passive sub-wavelength resonators

The first attempts in realization of passive (no gain) sub-wavelength electromagnetic resonant structures can be tied to the work by Pendry [3][1] in which

---

[1] For the sake of historical accuracy, we note that the earliest use of sub-wavelength resonant structures dates back to the Middle Ages. Artisans back then used metallic nano-particles ($\sim$ 100 nm size) by impregnating them in glass to achieve vibrant colors in stained glass on churches and cathedrals. The color is due to localized surface plasmon resonance (LSPR) excited by the incident sunlight. Depending on the ϵ_{metal} value and the particle size, the resonant wavelength

he proposed the use of metallic (conductive, non-magnetic) split-ring resonators (SRR) shown in Figure 1.1, to create a material with a *magnetic* response (having magnetic permeability $\mu_{\mathit{eff}} \neq 1$). This proposition, of course, relies on effective medium theory by which the macroscopic electromagnetic properties of a material can be calculated from those of the microscopic constituent elements as long as the size of the individual microscopic element is smaller than the radiation wavelength of interest.

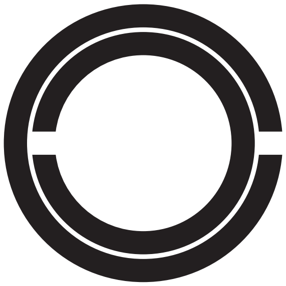

Figure 1.1: Illustration of the split ring resonator (SRR) proposed by Pendry. One can draw the LC-circuit analogy where the curved part of the SRR provides the inductance, while the gap gives rise to capacitance.

The benefit of this new magnetic material is that one can tailor the magnetic response (by altering the SRR design parameters), and achieve values of effective permeability that are not available in naturally occurring materials. This idea was first experimentally realized at the University of California San Diego, where a material was created (using the SRR and a wire grid), that for a certain band of frequencies, exhibited simultaneously negative permeability and negative permittivity, thereby having a negative index of refraction [4, 5]. This seminal work essentially spawned a new field of research in metamaterials, i.e. artificial materials that exhibit electromagnetic properties not found in nature. In the past decade upwards of 6,000 peer reviewed journal papers on the topic were published. Although initial metamaterials were limited to GHz frequencies due to fabrication challenges, there are some more recent reports of metamaterials at THz frequencies [6–8] and even at optical frequencies [9–11]. One of the often cited exciting

---

(color) changes. Underlying physics was unknown back then and it was only explained in the 1990's. Surface plasmon resonance however is beyond the scope of this dissertation.

promises of negative index materials (NIMs) is the realization of a so called “superlens” predicted by Pendry [12], where a thin slab of NIM, can produce a near-field image which is not diffraction limited due to the inclusion of both propagating and evanescent waves in the image formation. But meta-materials allow for much more than that. Because of the range of the achievable values of permittivity and permeability, meta-materials revolutionized conformal optic [13, 14], which most notably lead to realization of the invisibility cloak [15] where a carefully designed meta-material shell completely shields the object inside from the electromagnetic radiation, albeit of quite limited bandwidth. Sub-wavelength resonant structures are responsible for the realization of all these amazing ideas.

1.1.2 Active sub-wavelength resonators

When discussing active resonant structures, lasers are arguably the most important class of such resonators. Much like other technology, lasers have been getting smaller and more user-friendly ever since their discovery. This scaling down enabled laser integration in various devices. Indeed, lasers today are ubiquitous and can be found from laser-pointers to sophisticated biomedical diagnostic equipment, from games to sophisticated weapons, from advanced automotive technology to backbone hubs that our telecommunications and internet are relying on. For most of these applications the miniaturization of lasers played an important if not the crucial role.

The first laser miniaturization came with the discovery of solid state lasers (laser diodes) [16, 17] in which the device size was reduced from meter to millimeter scale. Discovery of vertical-cavity surface-emitting laser (VCSEL) [18, 19] enabled even further miniaturization, down to tens of micrometers scale. More recently, micro-scale whispering-gallery mode (WGM) lasers were achieved in micro-disks [20, 21] and micro-spheres [22]. Yet another advancement in miniaturization came with the use of 2D photonic crystals (PC) [23, 24] which lead to very tight optical mode confinement although the physical size of the laser was still several microns across. The first truly nano-scale lasers where realized only few years ago [25] with something of a paradigm shift away from WGM and PC designs earlier mentioned, in that they used metal to tightly confine the radiation. This latest wave of laser miniaturization is a lot more challenging then the previous ones because now we are dealing with the fundamental limitations imposed by the laws of physics, namely the diffraction limit. At the same time, this provides an exciting opportunity to conduct research in fundamental experimental physics in the ways that were not possible before. These nanolasers pave the way for examining atom-field interactions in truly nano-scale, ultra-small structures, which was thus far experimentally unattainable.

1.2 Dissertation organization

In this dissertation we aim to discuss the design fabrication and above else characterization of sub-wavelength resonators. The dissertation consists of two parts. First, we discuss passive sub-wavelength resonators in the RF part of the spectrum from the meta-material standpoint. In Chapter 2 we discuss the methods of characterization and verification of negative refractive index in meta-materials, specifically by phase measurement of a plane wave transmitted through a meta-material slab. Another exciting application of sub-wavelength resonators, highly efficient narrow-band antennas, is discussed in the Appendix A. There we discuss design objectives, fabrication methods and characterization results of such antennae.

In the second part (the bulk) of this dissertation, we focus our attention on active (with gain) sub-wavelength structures that operate at the optical (more accurately near-IR) frequencies. In Chapter 2 we discuss the design, fabrication and characterization of a sub-wavelength laser that operates at room temperature.

In Chapter 4 we explore the benefits and challenges of cryogenic operation of such nanolasers. We look at the tradeoff between the cavity size and the temperature of operation, and at different peculiarities that arise when nanolasers are cooled down.

In Chapter 5 we present a novel technique of fabrication of nanolasers using wafer bonding. This is a crucial step in making these lasers CMOS-compatible and integrating them with existing silicon photonic circuit elements.

In Chapter 6 we look at a completely different nanolaser geometry that enables us to drastically reduce the size of the laser. More importantly, this enables us to create a thresholdless laser which holds promise for amazing advancements in the silicon photonics field.

Lastly, in Chapter 7 we offer future directions for continual research on the topic of nanolasers, and summarize the material presented in this dissertation.

Chapter 2

Experimental confirmation of negative phase change in planar negative index material samples

2.1 Introduction

It is well understood that macroscopic electromagnetic material properties can be calculated knowing the constituent materials and their relative proportions. This approach in solid state physics is called the Effective Medium Theory (EMT) or the Effective Medium Approximation (EMA) and the requirement for its validity is that irregularities and distribution of constituent materials must be on a scale much smaller then the wavelength of the electromagnetic radiation that is used for interrogation [26, 27]. It was recently discovered that one can engineer such materials so that they exhibit properties not otherwise available in the natural-occurring materials. John Pendry suggested that by using metallic wires, one can engineer materials that exhibit negative effective permittivity (ϵ) at microwave frequencies [28]. Later, he suggested that by using metallic split ring resonators one can engineer materials with negative effective permeability (μ) [3]. Combining the two approaches into a periodic meta-material comprised of unit cells, containing metal wires and split ring resonators, and designing them carefully, it was shown that a material could be designed such that it has a microwave frequency band where the real parts of both (ϵ_{eff}) and (μ_{eff}) were simultaneously negative, which opened up the entirely new class of materials whose index of refraction can be negative [4]. In 1968, Veselago [29] predicted that if a material with dually negative permittivity and permeability could be found it would have totally new electromagnetic wave properties, including: (*i*) A negative index of refraction and (*ii*) a phase velocity with sign opposite to that of the group velocity.[1] He emphasized that this meant the phase of an electromagnetic wave propagating through a properly designed sample would accumulate negatively, i.e., opposite to that which occurs in all traditional materials. Veselago termed that relationship "Left-handed materials", which are now increasingly called NIM (Negative Index Materials). The first experimental report confirming a negative index of refraction used a wedge sample for a classical Snell's Law experiment and interpretation [5]. The reality of NIM has since been extensively confirmed by other groups [35, 36]. While these new reports confirmed "negative index", there have been no reports of far field measurements of the expected negative phase change accumulated by a transmitted plane wave propagating through a planar NIM sample.

2.2 Characterization

2.2.1 Methods of confirming the negative index

There are four ways (experiments) that we can think of to experimentally verify the negative index of refraction, each one with its strengths and weaknesses. The first approach is a classical Snell's law experiment with a wedge [36] (Figure 2.1a). Here, depending on the sign of the refractive index of the wedge, the incoming plane wave will refract on the opposite side of the normal, hence demonstrating the negative index of refraction. This is a robust and convincing experiment with one major drawback, which is that the sample needs to be made into a

---

[1] It is important to note that Veselago was not the first one to theorize about the materials in which group and phase velocities are of the opposite sign. Earlier references include [30–33] and great historical review is presented in [34].

wedge. This can be quite challenging, especially at THz frequencies, where current fabrication techniques allow for planar samples only.

The second possibility is another classical Snell's law experiment, lateral displacement of a beam propagating, at an angle, through a slab (Figure 2.1b). Again, depending on the sign of the refractive index of a slab, lateral displacement will occur on the opposite side of the incident beam. This is another elegant and simple experiment, but its results do not uniquely point to a negative index. It has been shown [37, 38] that, under certain conditions, a positive index slab can exhibit negative refraction, and a negative index slab can exhibit positive lateral shift. In other words, this experiment alone does not conclusively prove the sign of the refractive index of the slab.

The third experimental approach is to design a resonant cavity of thickness $w < \lambda/2$ composed of positive index material and negative index material [39] (Figure 2.1c). Because phase change accumulates in opposite directions in the negative and positive index materials, if we design the cavity carefully we can achieve that optical path lengths ($n \cdot d$) for the two materials in the cavity are *exactly* equal but of opposite signs. This effectively makes the effective path length zero, and thus the phase of the wave on two ends of the cavity exactly equal — the resonance condition. Note that it is physically impossible to build a resonant cavity whose length is less than $\lambda/2$ where λ is a wavelength in the medium. This is a quite elegant approach but it suffers from a major problem. If we are to build such a cavity, it is very hard to unequivocally prove that we actually have a resonant cavity. One way, depending on the reflectors at its ends, is to send a plane wave on one side of the cavity and detect it on the other. Then by sweeping the frequency we may observe a transmission dip at the resonant frequency. The problem here is to conclusively prove that this absorption is due to the resonance and not something else (material properties for example). A better way would be to introduce a probe in the cavity and measure phase along the length of the cavity and observe its buildup in PIM section, and its reduction in the NIM section of the resonator. Besides being technically challenging, the perturbation within the cavity caused by the probe, could diminish its performance.

Lastly, we can attempt a far-field phase measurement of a plane wave transmitted through a slab of material (Figure 2.1d). Depending on the sign of the refractive index, this phase change $\Delta\phi$ will also have a corresponding sign. This is the ultimate proof of negative index of refraction and it is compatible with planar samples (unlike the wedge method), it is infinitely scalable, and it can handle thin (even sub-wavelength) samples. This is the method we are proposing here, and we will treat it in more detail.

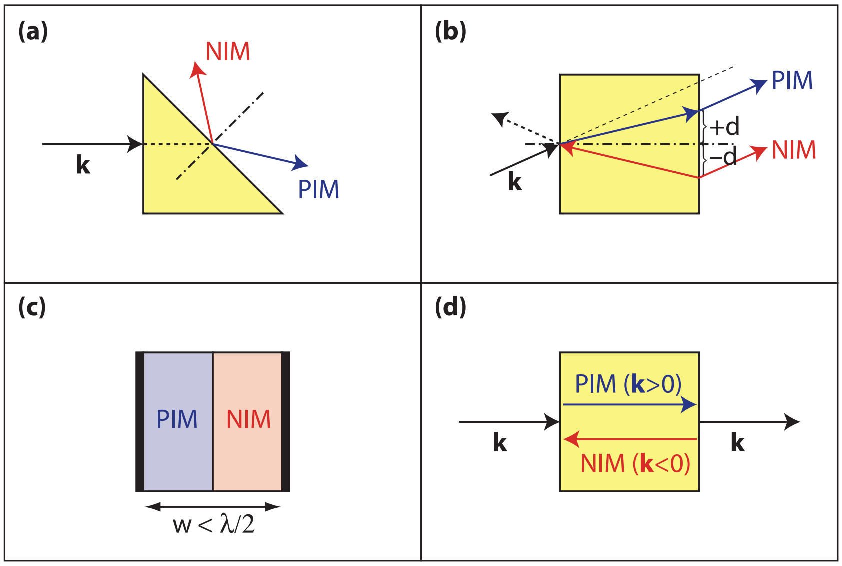

Figure 2.1: Various experimental approaches for verification of negative index: **(a)** Wedge experiment — beam will be refracted on the opposite side of normal for NIM and PIM material. **(b)** Lateral shift of the incident beam will have a different sign corresponding to that of the refractive index. **(c)** PIM/NIM resonant cavity of with $w < \lambda/2$ which is only possible if there is NIM slap as a part of the resonant cavity. **(d)** Transmitted phase change measurement — phase accumulated through a slab will have a sign that corresponds to that of refractive index of the slab.

2.2.2 Experimental setup and calibration

Figure 2.2 is a representation of our measurement system. A pair of P-band (12 – 18 GHz) horns spaced ∼ 200 cm apart is used as the source and for detection. The samples are placed between the horns in an aperture in a wall of the absorber as shown. The measurements of the S parameters as a function of frequency are obtained using an Agilent 8722ES vector network analyzer.

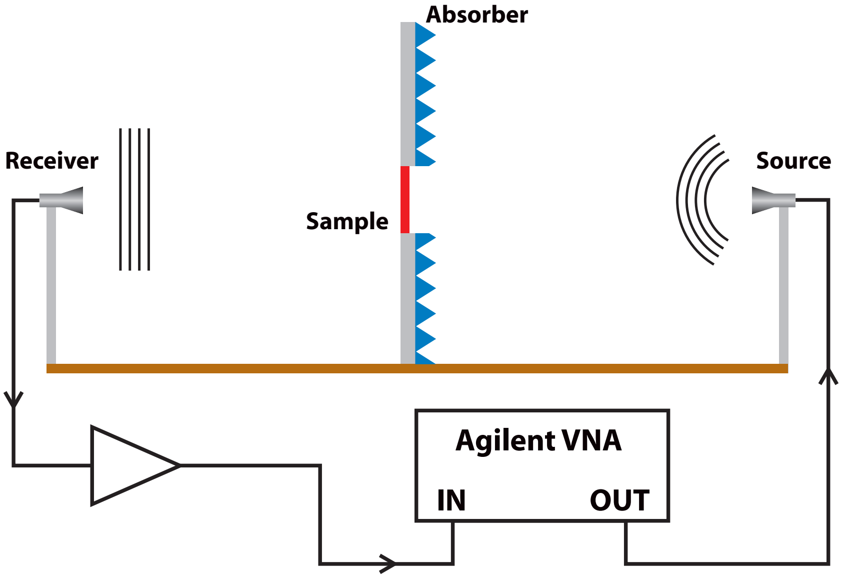

Figure 2.2: Free-space transmitted phase measurement system consists of a pair of P-band ($12-18\,\mathrm{GHz}$) horns (a transmitter and a receiver) spaced $2\,\mathrm{m}$ apart, and a wall covered with absorber with a square aperture for mounting the samples. Receiving horn is followed by a low-noise amplifier, and both horns are connected to a vector network analyzer.

In Figure 2.3, we present one example of several studies which were made for calibration and verification of the measurements of the phase change of the transmitted beam (S_{21}). A series of Teflon sheets (each 0.25 in thick) were tightly stacked and placed in the aperture, and the phase change of S_{21} between source and detector was measured as a function of total Teflon thickness at a frequency of 10 GHz. We emphasize that what is plotted in Figure 2.3 is the phase change at each frequency relative to the “no sample” condition. As can be seen, the experimental points (red) exhibit an excellent agreement with the predicted phase change (line in Figure 2.3) calculated from a simple relation $\Delta\phi = (n-1)k_0L$ where k_0 is the free-space wave vector, $n = 1.44$ is the refractive index of Teflon, and L is the thickness of the Teflon sheets.

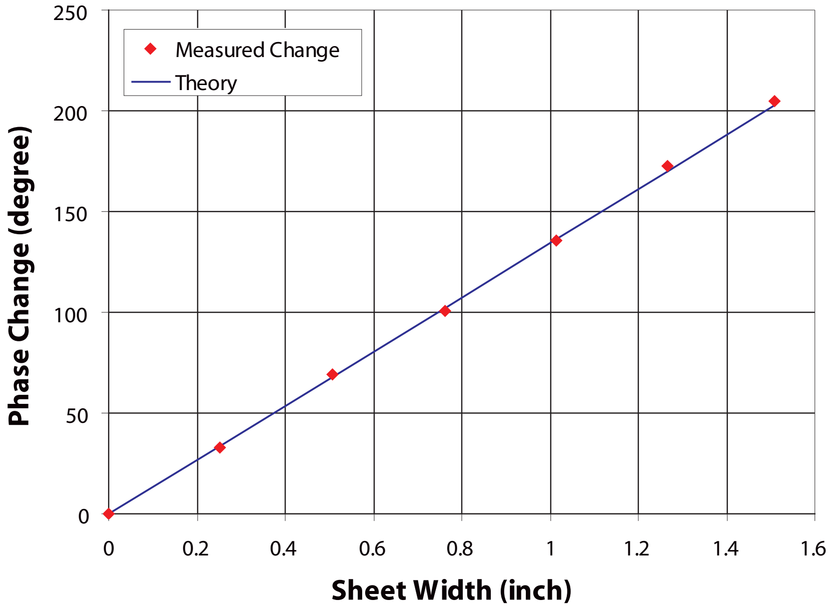

Figure 2.3: A series of Teflon sheets of varying thickness were used for the setup calibration. Theoretical curve is calculated from the relation $\Delta\phi = (n-1)k_0L$ with $n = 1.44$

2.2.3 Experimental results and discussion

In Figure 2.4, we present (red curve) the experimental magnitude of the transmitted wave S_{21} versus frequency from 13.5 to 16 GHz for a NIM sample. The sample (15 cm×14 cm cross section) was fabricated as described in [36], and is made with a dual SRR and two wires per unit cell. For all data shown, the sample thickness is 3 unit cells (1 cm). The blue curve is a result of a numerical S-matrix calculation made utilizing Ansoft's HFSS V8.0 software. Except for a slight frequency shift, the experiment and simulation agree well, as shown by the blue dashed line, which is the simulation result shifted by +0.15 GHz. We note that finding small frequency shifts between the numerical simulation and the measured properties for the presently made samples is quite common. This is mainly due to slight imperfections in sample fabrication process. We also note for our analysis that follows, that the maximum in $|S_{21}|$ is 0.9, indicating that in the region near 14.2 GHz the impedance match is very close to 1 for normal incidence.

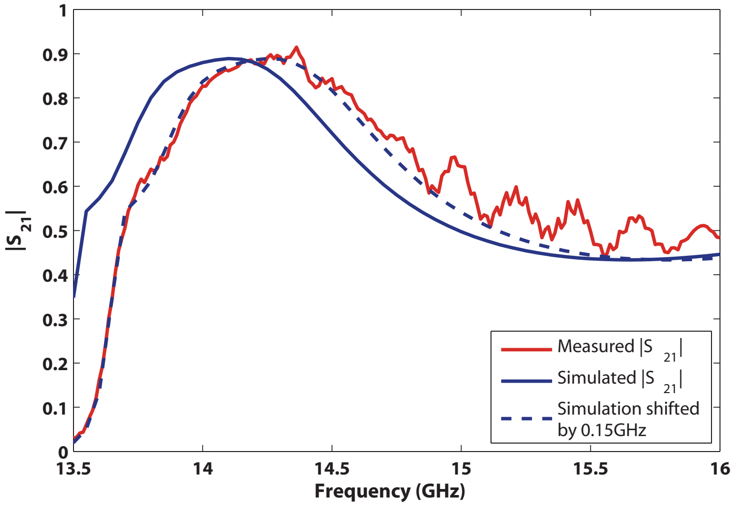

Figure 2.4: $|S_{21}|$ vs. frequency for experimental data (red curve), simulation data (blue curve), and simulation data shifted by 0.15 GHz (dashed blue curve).

In Figure 2.5, we plot the raw data (dotted curve) exactly as presented by the Agilent VNA for the phase change of S_{21} with respect to the no sample condition (an air path). The phase change of S_{21} as measured by the Agilent VNA or otherwise determined via simulations, is only defined modulo 360°. Thus, any 360° phase discontinuity should be corrected. In Figure 2.5 (dashed red curve), the discontinuity at 13.7 GHz can be removed by a 360° adjustment of the data points on either side. However, the phase change data can still be off by another integer multiple of 360°. We emphasize two key premises for being able to correctly assign these 360° corrections without the need for any additional experimental information: (*i*) The frequencyŰphase change data under consideration always lie within the first Brillouin zone (corresponding to the lowest NIM passband mode of the system) so the phase shift of one unit cell is between ±180°, and (*ii*) there are appropriate numerical simulation data available to confirm the magnitude of the expected phase change for one unit cell at a frequency near the condition $Z/Z_0 \sim 1$, $n \sim -1$. In our HFSS simulation, we confirmed that these two conditions, as designed, occurred at a frequency of 14 GHz. Since our unit cell was 3.33 cm, a phase shift of $\sim |56°|$ occurs for the wave traveling in either the $n = +1$ or $n = -1$ state. The phase change for the NIM sample (relative to no sample) when $n = -1$ is given by twice this number or $\sim -112°$ per cell. For three cells, this amounts to $\sim -336°$. We confirmed that after applying a 360° correction, our HFSS simulation of a three-cell sample correctly corresponded to the phase change as shown in Figure 2.5 (blue curve), and then applied the same correction to the experimental phase change data, resulting in the solid red curve of Figure 2.5. (To avoid confusion, we do not make the 0.15 GHz frequency shift that was illustrated in Figure 2.4.)[2] We do emphasize at this point that the algebraic sign of the experimental phase change (and simulation) correspond to negative values as expected.

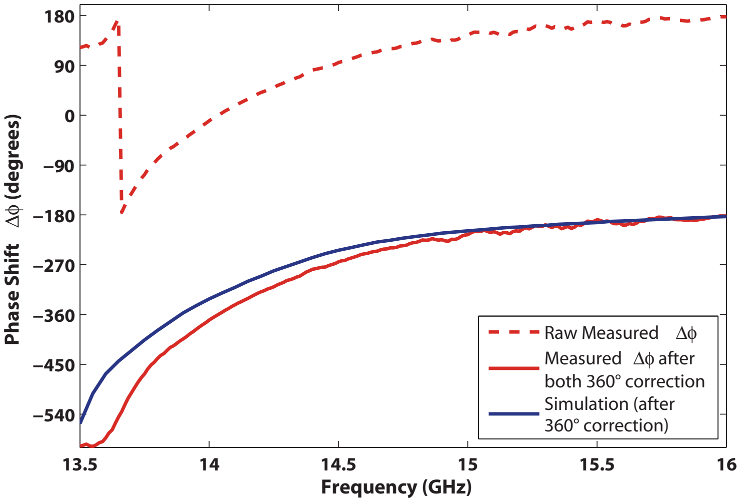

Figure 2.5: Phase change of $|S_{21}|$ vs frequency (a) raw experimental data (dashed red curve), (b) experimental data with 360° corrections (solid red curve), and (c) simulation data with 360° corrections (blue curve).

In Figure 2.6, we present the refractive index n versus frequency determined in three ways: (*i*) (red curve), n is determined using the experimental phase difference data of Figure 2.5 from the relation $\Delta\phi = (n-1)k_0L$, (*ii*) (blue curve) n is determined from the full numerical simulation S-matrix via the retrieval method (for details, see Appendix B), and (*iii*) (black dots) n is experimentally measured via SnellŠs law experiments on a 12° wedge sample [36]. It is clear that if one does

---

[2] Using HFSS, we have also performed eigenmode calculations and determined the lowest pass-band of the NIM-band structure whose dispersion yields an indexŰfrequency relation in agreement with the full S-matrix simulation of Figure 2.6.

apply a 0.15 GHz shift to the simulation data, then over the index range from -2.5 to -0.5, there is a quite satisfactory agreement for all three data sets.

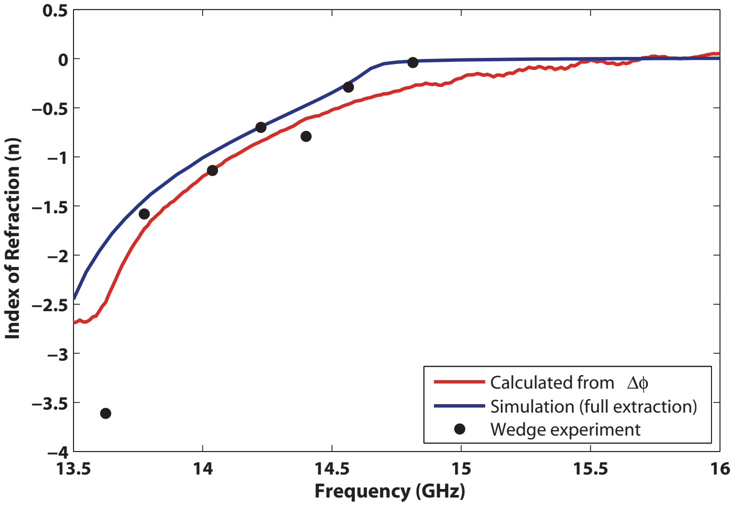

Figure 2.6: Refractive index n vs frequency (a) calculated from measured phase (red curve), (b) from full numerical simulation of the S matrix (blue curve), and (c) measured in the wedge experiment (black dots) [36].

2.3 Conclusion

From the agreement between the three data sets presented in Figure 2.6, we conclude that we have confirmed the accumulation of a negative phase change for a NIM sample in the frequency range of 13.6–14.6 GHz. We note that while the full S-matrix numerical simulation correctly displays a kink near $n = 0$ at 14.75 GHz (indicating the upper edge of the negative index band), our deduced values of n from the phase data do not. The simple expression $\Delta\phi = (n-1)k_0L$ is no longer qualitatively valid for the $n \approx 0$ region, or for $n < -2.5$ as the sample is far from matched in those regions. Despite this limitation, we suggest that the careful determination of the correct phase change through test samples via the analysis illustrated herein, and in the frequency region where the surface impedance is closely matched to free space, is a rigorous test for confirmation of the negative index property without the need for a wedge sample. Because it is a far field range measurement, the technique can be applied at arbitrarily high frequencies, where the possibility of making phase measurements within the sample [40] is no longer practical.

Chapter 2, in part, is a reprint of the material as it appears in “Experimental confirmation of negative phase change in negative index material planar samples,” D. Vier, D. R. Fredkin, A. Simic, S. Schultz, and M. Tanielian, *Applied Physics Letters*, vol. 86, no. 24, p. 241908, 2005. The dissertation author was the primary co-investigator and coauthor of this paper.

Chapter 3

Room-temperature sub-wavelength metallo-dielectric lasers

3.1 Introduction

Achieving the most compact footprint for photonic components is an important factor in the design of integrated optical devices. Like most other photonic components, the minimum size for a laser is ultimately governed by λ_0, the free-space wavelength. For example, as the size of a conventional Fabry-Pérot semiconductor laser is scaled down in all three dimensions towards λ_0, three effects adversely influence the lasing process. First, the round trip path of the optical wave in the gain medium is shortened. Second, radiative losses from the end mirrors are increased. Third, the lateral field confinement in the resonator waveguide is reduced, resulting in less overlap of the optical mode with the gain medium. All these effects serve to increase the lasing threshold, and lasing cannot therefore be achieved below a certain size limit. By allowing the laser size to increase in one or two dimensions, it is possible to reduce the physical size of the laser in the remaining dimension(s) to values below this limit. For example, the disk thickness in whispering-gallery-mode (WGM) lasers [20] can be reduced to a fraction of the free-space wavelength [21], but to compensate for this thickness reduction the disk diameter should be increased accordingly. The ultimate challenge in this respect is concurrent reduction of the resonator size in all three dimensions, while still satisfying the requirements for lasing action.

The size of an optical cavity can be defined using different metrics (for example, the physical dimensions of the cavity or the size of the optical mode). However, if the goal of size reduction is to increase the integration density (for example, in a laser array), the effective cavity size should account for both the overall physical dimensions of the resonator and the spread of the optical mode beyond the physical boundary of the resonator. By this token, most conventional dielectric laser cavities are not amenable to dense integration because they either have a large physical footprint or a large effective mode. For example, distributed Bragg resonators [41] and photonic-crystal cavities [42] (both of which can be designed to have very small mode volumes) have physical footprints that are many wavelengths in size, due to the several Bragg layers or lattice periods that are required for maintaining high finesse. On the other hand, it has been demonstrated that the diameter of thick (λ_0/n) micro-disk lasers can be reduced below their free-space emission wavelength [43]; however, the spatial spread of the resultant modes (which have low azimuthal numbers owing to the small disk diameters) into the surrounding space beyond the physical boundaries of the disks may lead to mode coupling and formation of "photonic molecules" in closely spaced disks [44]. To illustrate the case, the M = 4 WGM for a semiconductor disk with radius $r_c = 460\,\text{nm}$ and height $h_c = 480\,\text{nm}$ (Figure 3.1a) is shown in Figure 3.1b, clearly indicating the radiative nature of the mode and its spatial spread, which, as mentioned, can lead to mode coupling with nearby structures.

3.2 Design

One approach for alleviating these issues is to incorporate metals into the structure of dielectric cavities, because metals can suppress leaky optical modes and effectively isolate them from their neighboring environment. The modes in

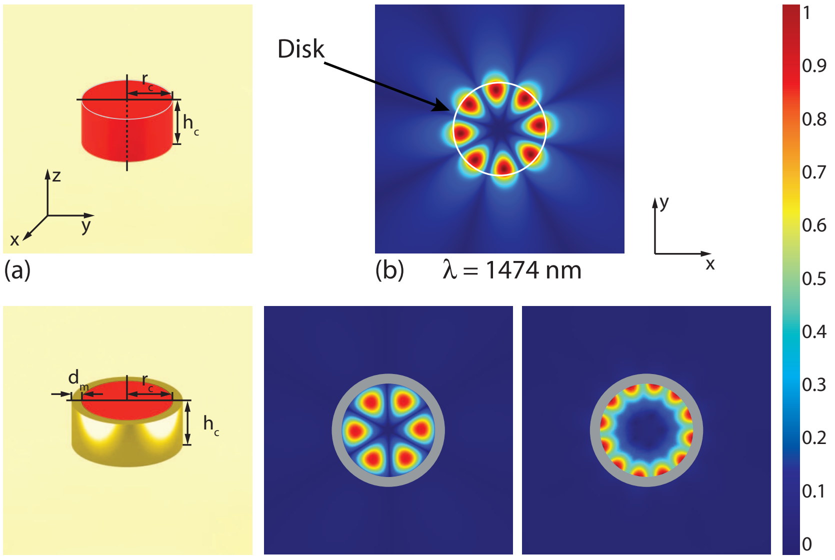

(a) (b) $\lambda = 1474$ nm

(c) (d) $\lambda = 1532$ nm (e)

Figure 3.1: **(a)** A thick semiconductor disk ($r_c = 460\,\text{nm}$, $h_c = 480\,\text{nm}$, $n_{semi} = 3.4$) and its $M = 4$ whispering-gallery resonance **(b)** are shown. Note the spatial spread of the mode compared to the actual disk size. **(c − e)** The same disk encased in an optically thick ($d_m = 100\,\text{nm}$) gold shield **(c)** will have well-confined reflective **(d)** and plasmonic **(e)** modes, but with much higher mode losses. |E| is shown in all cases, and the section plane is horizontal and through the middle of the cylinder.

these metallo-dielectric cavities can be grouped into two main categories: (*i*) surface bound (that is, surface plasmon polariton (SPP)) resonant modes and (*ii*) conventional resonant modes, resulting purely from reflections within the metal cavity. Although they are highly confined, the disadvantage of plasmonic modes is their high loss, which is caused by the relatively large mode overlap of the optical field with the metal (compared to the reflective case). Owing to the high Joule loss at telecommunication and visible wavelengths, the lasing gain threshold for such cavities can be very large. On the other hand, the negative permittivity of metals not only allows them to support SPP modes, but also enables them to act as efficient mirrors. This leads to the second class of metallo-dielectric cavity modes, which can be viewed as lossy approximations of the modes in a perfectly conducting metal cavity. Because the mode volume overlap with the metal is usually smaller than in the plasmonic case, in this type of cavity it is possible to achieve higher Q factors and lower lasing gain thresholds, albeit at the expense of reduced mode confinement (compared to plasmonic modes). In general, both types of mode can exist in a real metal cavity. Embedding the aforementioned gain disk in a gold shield (Figure 3.1c) effectively confines the resonant modes while increasing Joule losses. As discussed, the surface-bound plasmonic mode (Figure 3.1e) has both a higher M number and higher losses (M = 6, Q = 36) compared to the non-plasmonic mode (Figure 3.1d, M = 3, Q = 183).

It should be noted that even though the metal shield is the source of Joule loss, the large refractive index of the semiconductor core ($n_{semi} \approx 3.4$) aggravates the problem and increases both the plasmonic and Fresnel reflection losses. For SPP propagation on a (planar) semiconductor–metal interface, the threshold gain for lossless propagation is proportional to n_{semi}^3 [45]. This means that, even though high-Q plasmonic modes can exist inside metal cavities with low-index cores (for example, silica, $n = 1.48$ [46]), using this approach to create a purely plasmonic, room-temperature semiconductor laser at telecommunication wavelengths will be very challenging, due to the order-of-magnitude increase in gain threshold.

One solution for overcoming the metal loss obstacle is to reduce the temperature of operation. This will have two coinciding benefits, a reduction of the Joule losses in the metal and an increase in the amount of achievable semiconductor gain. Recently Hill and colleagues [25] have demonstrated cryogenic lasing from gold-coated semiconductor cores with diameters as small as 210 nm. However, in this case the metal is directly deposited on the semiconductor core (with a 10 nm SiN insulation layer between; Figure 3.2a, left). As a result, owing to the large overlap of the mode with the metal, the estimated room-temperature cavity Q is quite low. The best case is ~ 180 for a silver coating (assuming the best reported value for the permittivity of silver [47]). This corresponds to an overall gain threshold of $\sim 1{,}700\,\mathrm{cm}^{-1}$ and is quite challenging to achieve at room temperature. Even though this device lases when cooled to cryogenic temperatures, it would be challenging to achieve room-temperature lasing with the same approach and a similarly sized cavity, due to the constraints imposed by the amount of available semiconductor gain and metal losses. The gain coefficient reported for optically pumped bulk InGaAsP emitting at 1.55 µm is reported to be $\sim 200\,\mathrm{cm}^{-1}$ [48]. Electrically pumped multiple quantum wells (MQWs), on the other hand, have been reported to have higher material gain coefficients of over $1{,}000\,\mathrm{cm}^{-1}$ [49]. Also, recent results obtained from Fabry-Pérot-type metallic nanolasers at room temperature indicate that this level of gain is also achievable from bulk InGaAs [50]. However, even if the required gain is achievable at room temperature, efficient operation of the device would still be a challenge due to thermal heating and non-radiative recombination processes (for example, Auger recombination). In particular, to operate a densely packed array of such devices, thermal management would be a major concern, given the requisite intense pumping levels. Consequently, it is extremely important to optimize the cavity design so that the gain threshold is minimized.

3.3 Design and Simulation

Previously, we have predicted that by incorporating a dielectric shield layer between the metal and the semiconductor (Figure 3.2a, right) and optimizing the dielectric thickness, the gain threshold of the laser can be substantially reduced so that it is amenable to operation at room temperature [51]. The benefit stems from the tendency of the low-index shield to push the electromagnetic mode towards the high-index inner core and away from the metal walls, reducing the mode–metal overlap and hence the Joule loss. Excessive shield thickness can be detrimental, because the shield uses up space within the device that would otherwise be filled with the gain. For a fixed total waveguide radius R_{tot} and for each waveguide mode, an optimal shield thickness Δ (with the corresponding gain core radius $r_c = R_{tot} - \Delta$) exists that minimizes the threshold gain [51]. This is illustrated in Figure 3.2b for the TE_{01} mode and $R_{tot} = 460\,\mathrm{nm}$ (the same device footprint as in Figure 3.1), using silica ($n = 1.46$) as the shield layer. It can be seen that the optimally sized shield ($\Delta \approx 200\,\mathrm{nm}$) reduces the gain requirement several fold relative to a metal-clad device of equal diameter but without the shield ($\Delta = 0$). Furthermore, one can ensure, by proper design, that the mode of interest is in cutoff in the upper and lower sections of the waveguide, where the core is only

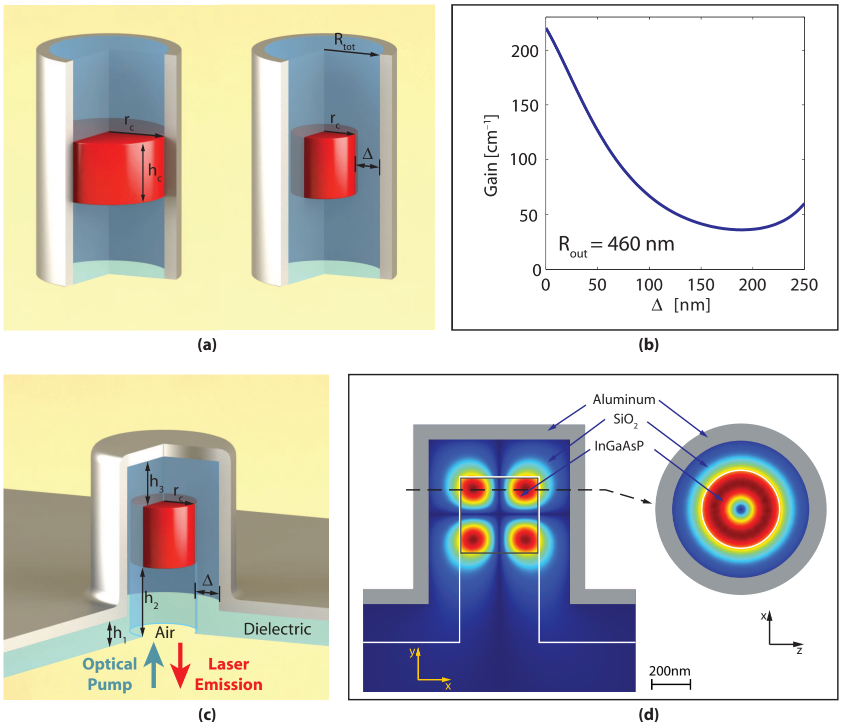

(a) (b) (c) (d)

Figure 3.2: **(a)** Metal-coated gain disk with vertical confinement provided by low-index waveguide cutoff sections (left panel) as demonstrated by Hill and colleagues [25]. Same structure, but including a dielectric shield layer of thickness Δ (right panel). **(b)** Variation of gain threshold of the composite gain/dielectric/metal waveguide as the dielectric shield thickness Δ is changed, assuming a fixed total radius $R_{tot} = 460\,\text{nm}$ [51]. **(c)** Practical realization of the laser cavity for compatibility with planar fabrication techniques. The air gap at the bottom of the laser is formed after a selective etch of the InP substrate. **(d)** Cross-sections of |E| for the TE_{012} mode of the cavity. In the designed cavity the values for h_1, h_2 and h_3 are 200, 550 and 250 nm, respectively.

composed of dielectric with no high-index core (Figure 3.2a). When this is the case, the structure acts as a three-dimensional optical resonator [51].

The conceptual diagram in Figure 3.2a implies that the upper and lower waveguide sections, where the mode is in cutoff, extend to infinity. In practice, we truncate the guide some distance above and below the gain section Figure 3.2c, far enough so that the energy leakage resulting from this truncation is minor. The light escaping from the lower section is used as the laser output, and the upper section is capped with metal for unidirectional emission and fabrication process compatibility. Also, owing to a selective etch step in our fabrication process, the lower cutoff section ends up comprising a composite core with an air column directly underlying the gain block (instead of a solid silica core). This does not compromise the performance of the resonator; in fact, it makes the cutoff in the lower section more severe. Figure Figure 3.2d shows two cross-sections of |E| for the TE_{012} mode of the resonator in Figure Figure 3.2c.

The resulting room-temperature Q of this cavity is $\sim$ 1,030 (assuming gold, $\epsilon = -95.9 - 11i$ [52], for the metal shield), with a resonance at 1.55 µm and a gain threshold of only 130 cm^{-1}. Note that both the physical size and modal size of this cavity are smaller than the wavelength of emission. Assuming a minimum metal shield thickness of 70 nm (which is twice the skin depth), the diameter and height of this laser are 1.1 and 1.35 µm, respectively. Also, in addition to having a low gain threshold, the laser is optically isolated from any structure placed next to it.

3.4 Fabrication

The shielded laser structure was fabricated from an InGaAsP MQW gain layer grown on InP. Hydrogen silsesquioxane (HSQ) electron-beam resist was patterned into arrays of dots (Figure 3.3a) using a Raith 50 electron-beam writer, and the size of the dots was varied by changing the pattern size and/or the electron-beam dosage. Cylindrical structures were then etched using $CH_4/H_2/Ar$ reactive ion etching (RIE) (Figure 3.3b). Using an optimized and calibrated plasma-enhanced chemical vapor deposition (PECVD) process, the silica shield layer was grown to a thickness of $\sim$ 200 nm (Figure 3.3c). Note that the outline of the embedded gain core is visible through the silica layer. In practice, the low adhesion of gold to silica caused separation of the dielectric portion of the structure from the metal layer. Fortunately, aluminium exhibits has better adhesion properties, and at the wavelength of interest its optical properties are very close to gold.[1] A layer of aluminum with a minimal thickness of 70 nm was sputtered over the silica-covered pillars (Figure 3.3d). The sample was then bonded on the upper side to a glass slide using SU-8, and the InP substrate was subsequently removed

---

[1] The cavity Q of the resonator with an aluminum coating ($\epsilon = -238.5 + 44.7i$ [52]) is 1,004, which compares with 1,030 for gold.

in a selective HCl etch, leaving an air void under the structure. Figure 3.3e shows the tilted bottom view of an air void, with the lower face of the gain core visible inside. Figure 3.3f shows the normal bottom view (with enhanced contrast levels) of a similar void. The faint outline of the silica shield is discernible in this image, verifying the 200 nm thickness of the shield. (Further details of the fabrication process are presented in Section 3.7.3.)

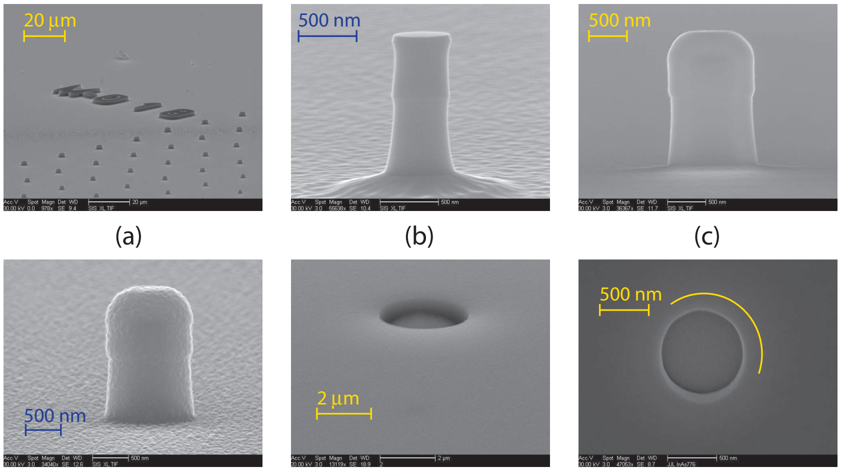

(a) (b) (c)

(d) (e) (f)

Figure 3.3: **(a)** Array of electron-beam patterned HSQ resist dots. **(b)** RIE etched pillar after oxygen plasma and buffered oxide etch cleaning. The faint bump in the middle indicates the boundary between the InGaAsP and InP layers. **(c)** Etched pillar after PECVD of silica. The outline of the semiconductor pillar can be seen through the silica layer. **(d)** Silica-covered pillar after undergoing aluminium sputtering (70nm). **(e)** Tilted bottom view of one of the samples after a selective InP etch with HCl. The surface is composed of PECVD deposited silica. The hole corresponds to the air hole shown in the diagram of Figure 3.2d. **(f)** Contrast-enhanced normal bottom view of a cavity. The circular outline around the air hole is due to the dielectric shield and agrees well with the target dielectric shield thickness of 200 nm.

3.5 Characterization

For optical pumping we used a 1,064 nm pulsed fibre laser operating at a repetition rate of 300 kHz and a pulse width of 12 ns. The pump beam was delivered to the samples using a ×20 or ×50 long-working-distance objective, which also collected the emitted light. To estimate the amount of pump power absorbed by the core, a full three-dimensional finite-element analysis was carried out over a range of core sizes (see Section 3.7.1 for details of calculations). Using a double 4–f imaging system in conjunction with a pump filter (Semrock RazorEdge long wavelength pass), the samples were imaged onto either an IR InGaAs camera (Indigo Alpha NIR) or a monochromator (Spectral Products DK480) with a resolution of 0.35 nm and equipped with a cooled InGaAs detector in a lock-in detection configuration. Owing to the electron-beam writing process, the samples were slightly elliptical. The major and minor diameters of the gain core for the particular sample under test were measured to be 490 and 420 nm, respectively.

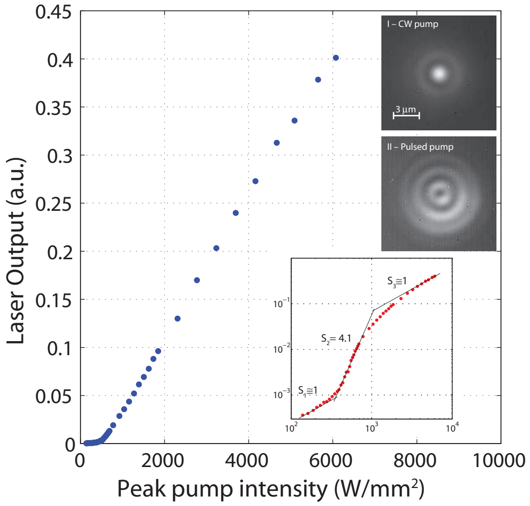

Figure 3.4: Light–light curve for a nanolaser with major and minor core diameters of 490 nm and 420 nm (blue dots), respectively. The same data set is shown as a log–log plot (bottom inset, red symbols) together with the slopes for the PL, ASE and lasing regions. Also shown are the images of the defocused emitted beam cross-section (taken ∼ 10 µm away from the nanolaser exit aperture) for (I) c.w. pumping and (II) pulsed pumping. The appearance of the higher-contrast fringes indicates increased coherence due to lasing.

In Figure 3.4 the light–light curve corresponding to a laser emitting at 1,430 nm is presented (blue symbols), which shows a slope change indicating the onset of lasing at an external threshold pump intensity of ∼ 700 W/mm^2. The same data set is shown in a log–log plot (Figure 3.4, red inset graph), with the slopes of different regions of operation indicated on the plot. The S-shaped curve clearly shows the transition from photoluminescence (PL) to amplified spontaneous emission (ASE) and finally into the lasing regime. Also shown in Figure 3.4 are the emission patterns of the defocused laser image captured with the IR camera, corresponding to continuous-wave (3.4, inset (I)) and pulsed (3.4, inset (II)) pumping situations. The average pump intensity in each case was approximately equal to $8\,\mathrm{W/mm^2}$. In the c.w. case, only broad PL emission occurs, owing to the low peak intensity. However, when the pump is switched to pulsed mode, lasing is achieved due to the 278-fold increase in peak power. At the same time, the defocused image forms a distinct spatial mode with increased fringe contrast, which is an indication of increased spatial coherence and is further evidence of lasing. The polarization of the emission has a strong linear component, which is due to the slight ellipticity of the gain core (see Section 3.7.4 for more details).

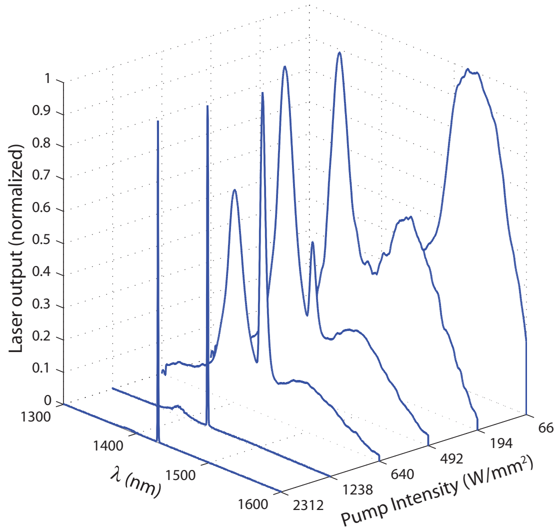

Figure 3.5: Evolution of the emission spectra from PL over ASE to lasing.

Figure 3.5 shows the evolution of the emission, from a broad PL spectrum to a pair of competing ASE peaks and finally into a narrow lasing line at 1,430 nm. The measured linewidth of this particular laser was 0.9 nm; however linewidths as small as 0.5 nm were measured for other samples in the same size range.

Another way to verify the soundness and accuracy of the design and fabrication processes is to match the lasing wavelength with the target resonance of the cavity. However, owing to the high pump intensity, the refractive index of the gain core can vary substantially from its quiescent value and this can considerably shift the lasing line from its target wavelength. Using the measured results from an array of lasers with slightly different sizes (which were measured individually using a scanning electron microscope, SEM) and exact three-dimensional finite-element modelling of each of the gain cores, the refractive index of the gain medium under pumping conditions was estimated at each lasing point (Figure 3.6, green symbols and error bars).

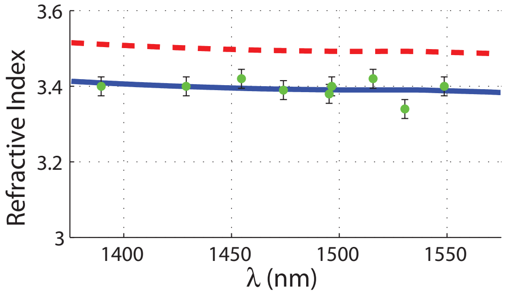

Figure 3.6: Effective refractive indices (green symbols) of the pumped MQW gain medium at lasing wavelengths, back-calculated from lasing spectra obtained from an array of nanolasers. Error bars were calculated assuming ±5 nm error in measuring the disk diameters from the SEM images. The dashed red curve shows the effective refractive index of the unpumped MQW layer, as measured by a Filmetrics interferometric analyzer. The blue curve is offset from the red by a constant amount (0.102 RIU), which was chosen for best fit to the lasing data. The index reduction is consistent with the estimated free-carrier effects.

Assuming a uniform drop over the spectrum of interest and using a least-squares fit of these data points, the estimated refractive index drop is ~ 0.102 refractive index units (RIU) (least-squares fit) lower than that reported by interferometric multilayer measurements of the unpatterned wafers under low illumination intensity (Figure 3.6, red dashed line). We attribute this shift to be mainly due to free carrier effects (a combination of bandfilling, bandgap shrinkage and free carrier absorption), for which the net effect at the estimated carrier density ($\sim 1.2 \times 10^{19}\,\mathrm{cm}^{-3}$ for a 520 nm diameter core) is expected to cause a refractive index drop of $\sim 0.1\,\mathrm{RIU}$ [53] (see Section 3.7.1 for details of carrier density estimation). Also, a slight additional contribution (at most $-0.004\,\mathrm{RIU}$) may also be present due to compressive pressure on the gain cores, which is exerted by the thermal shrinkage of the aluminium layer after deposition in the sputtering chamber (see Section 3.7.1).

3.6 Conclusion

In conclusion, we have demonstrated room-temperature lasing from subwavelength metallo-dielectric resonators. In addition to reducing the size below the emission wavelength in all three dimensions, the metal layer isolates the cavity from its outer environment. Extending the current design approach to an electrically pumped structure may have practical applications such as dense optical interconnects [54] and laser arrays for optical trapping and manipulation of particles [55], both of which are currently limited by the larger size and lateral coupling effects in vertical-cavity surface-emitting laser (VCSEL) arrays. It should be noted that a characteristic of this laser design is that it allows the placement of two coherent sources in very close proximity while allowing them to operate independently with no cross-coupling. According to the Rayleigh criterion, two point sources that are placed closer than $0.61\,(\lambda/\mathrm{NA})$ cannot be resolved into separate spots in the image plane (where λ and NA are the wavelength and numerical aperture of the imaging system, respectively). This places an upper bound on the maximum packing density of a free-space optical interconnect system. For an imaging system with $\mathrm{NA}=0.8$ and operating at $1.55\,\mu\mathrm{m}$, the Rayleigh distance is $\sim 1.2\,\mu\mathrm{m}$, which is slightly larger than the minimum spacing achievable with this nanolaser ($\sim 1.1\,\mu\mathrm{m}$). Crossing the Rayleigh limit implies that arrays of this type of nanolaser can potentially reach the diffraction-imposed maximum bound on interconnect density. It should be stressed that passing this limit might also be advantageous for potential near-field applications that may benefit from further reduction in the nanolaser size. However, it should also be noted that, due to the physical limits imposed on the size of resonators incorporating conventional reflective resonances (such as the current nanolaser design), using this approach to reduce the resonator dimensions to sizes far below $\lambda_0/2n$ ($\sim$ 200 nm, assuming λ_0=1,550 nm and n=3.4) is not feasible and the solution will most probably lie in the realm of plasmonic resonant devices [56], assuming that the high room-temperature loss in such cavities can be efficiently surmounted.

The small size of the cavity may also enable the implementation of high-speed directly modulated lasers through spontaneous emission enhancement by means of the Purcell effect [57]. The estimated Purcell factor for the current design lies between 19 and 41 (see Section 3.7.2). Using silver instead of aluminium is expected to improve the threshold characteristics of these lasers because of its superior optical properties. With a silver shield, the estimated Q-factor for the same cavity at room temperature is $\sim$ 3,350, the gain threshold is only $\sim 50\,\mathrm{cm}^{-1}$ and the estimated Purcell factor range lies between 62 and 137. Furthermore, given that the current resonator design is readily scalable to longer wavelengths (due to the improved optical properties of metals in the infrared), it may also be applied to develop planar arrays of metallo-dielectric quantum-cascade lasers that are integrated with metallic beam-forming elements [58] and can be used for high-resolution imaging in the mid- and far-infrared regions of the spectrum.

3.7 Methods and additional material

3.7.1 Simulations

The resonant modes and gain thresholds were found using COMSOL's 2-D and 3-D eigenmode solvers. The analysis of pump penetration and absorption in the cavity was done using the scattered field formulation for plane wave illumination in COMSOL. The optical constants of the metals were obtained from Palik [52] and Johnson and Christy [47]. The optical constants of the MQW gain medium were measured using an infrared thin film measurement system (Filmetrics 20®) and were in good agreement with values cited in the literature [59].

Since the lasers are designed to be optically pumped, pump penetration into the core is an important factor to be considered, given the small size of the input aperture. For pumping we used a 1,064 nm pulsed fiber laser operating at 300 kHz repetition rate and 12 ns pulse width. The pump beam was delivered to the samples using a ×20 or ×50 long working-distance objective which also collected the emitted light. In order to estimate the amount of pump power absorbed by the core, a full 3-D finite element analysis was carried out over a range of core sizes (with fixed dielectric shield thickness), assuming illumination with a plane wave at a pump wavelength of 1,064 nm and a peak illumination intensity of 1 kW/mm^2 (Figure 3.7a, solid blue curve). As shown, the total power absorbed in the core exhibits oscillations at small core sizes, which flatten out as the core size increases. These oscillatory features are also present when a perfect conductor is substituted for the aluminum layer (Figure 3.7a, dashed blue curve), eliminating the possibility that this phenomenon is a manifestation of surface plasmon related effects (e.g. extraordinary transmission through a metallic aperture [60]) and indicating that the resonant behavior is due to simple resonance of the pump inside the metallic cavity (which is stronger for smaller core sizes, since a smaller proportion of the core is absorptive). Interestingly, for smaller core sizes a significant proportion of the pump power is funneled through the silica layer and absorbed through the sidewall of the gain core (Figure 3.7b), which is an indirect benefit of using the shield layer. The red curve in Figure 3.7a shows the generated carrier density for a peak pump intensity of 700 W/mm^2 and a (rectangular) 12 ns pump pulse width.

Estimation of the carrier density was performed using the rate Equation 3.1 assuming a carrier dependent recombination lifetime $\tau_r = (B_0 N_c)^{-1}$, where N_c is the carrier density, $B_0 = 1 \times 10^{-10}\,\mathrm{cm}^3/\mathrm{s}$ [61] and $\phi_0(t)$ is the incoming photon flux signal, calculated from the pump peak power.

$$\frac{dN_c(t)}{dt} = \phi_i(t) - B_0 N_0^2(t) \tag{3.1}$$

The refractive index drop due to carrier effects was estimated using results derived in [53]. Depending on the carrier density level, the effects of band filling, bandgap shrinkage and free carrier absorption can induce a positive or negative refractive index change, depending on the wavelength and the dominating process(es). For InGaAsP at 1.55 µm and for the high carrier densities estimated in our case (about $1.2 \times 10^{19}\,\mathrm{cm}^{-3}$ for a core diameter of 520 nm), the combination of band filling and

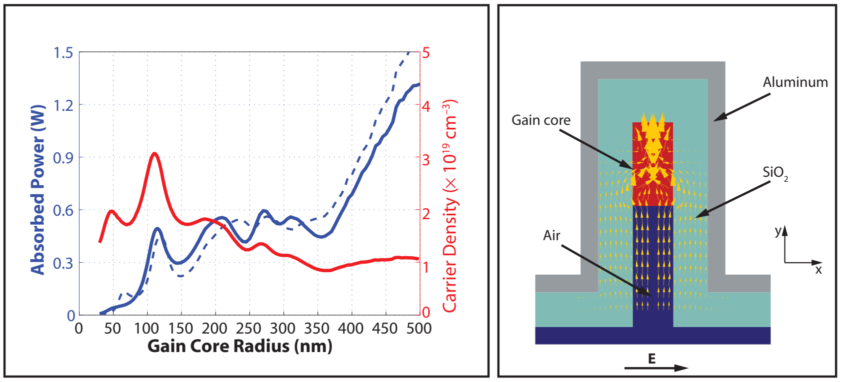

(a)

(b)

Figure 3.7: **(a)** Results of 3-D FEM simulations showing the absorbed pump power in the gain core as the size of the core is varied (blue curves). The core height is 480 nm and the solid and dashed curves correspond to aluminum and perfect conductor metal shields, respectively. The pump wavelength is 1,064 nm, polarized in the x direction and the incident intensity is assumed to be 1 kW/mm^2. The red curve shows the estimated threshold carrier density assuming 12 nm pulses. The pump power is assumed to be the threshold value of 700 W/mm^2. **(b)** Pump power flow (yellow arrows) showing how the dielectric shield funnels the pump beam through the sides of the gain disk. The core radius in this case is 116 nm, corresponding to the first absorption peak for an aluminum shell (solid blue line in **(a)**)

free carrier absorption dominates the bandgap shrinkage effect, resulting in an estimated net drop of approximately 0.1 in the refractive index [53].

Another phenomenon that may contribute to refractive index decrease is the compressive pressure exerted by the sputtered aluminum shield after it cools down to room temperature. Even though a 70 nm layer of aluminum is sufficient to create optical confinement, the actual sample was covered with an additional one micron layer of aluminum for better heat sinking. This metal layer will have a larger thermal contraction than the silica/InGaAsP core and will exert compressive pressure on it, which will result in a drop in the InGaAsP refractive index. However, we believe this effect to be negligible in our structures. As the device cools, the difference in thermal contraction (24 ppm/°C for aluminum vs. 5 ppm/°C for both silica and InGaAsP) is accommodated partly by compression of silica/InGaAsP core, and partly by compression of nearby aluminum. Even if all of the compression occurred in the core, it would amount to just 0.0019 for a 100 °C drop in temperature. Assuming the Young modulus of the core to be nominally $E = 70\,\mathrm{GPa}$, the stress corresponding to this small compression would be less than 0.14 GPa, and the effect of this small stress on the refractive index less than 0.004 [62, 63].

3.7.2 Purcell factor estimation

Cavity-induced enhancement of spontaneous emission into a resonant mode relative to spontaneous emission in bulk material (the Purcell factor) can be estimated as [64]:

$$F_{cav} = \frac{Q\lambda_{cav}^3\zeta}{4\pi^2 n_{bulk}^3 V_{eff}}, \quad V_{eff} = \frac{1}{n_{bulk}^2}\iiint n(\mathbf{r})^2|\mathbf{f}(\mathbf{r})|d^3\mathbf{r}, \quad \zeta = \frac{|\mathbf{d}\cdot\mathbf{f}(\mathbf{r_e})|^2}{\frac{1}{3}|\mathbf{d}|^2} \tag{3.2}$$

where bulk n is the refractive index of the bulk material used as reference (in this case InGaAsP, $n_{bulk} = 3.53$), Q is the (unpumped) quality factor, λ_{cav} is the free-space wavelength of the resonance, and V_{eff} and ζ account respectively for the electric field concentration and the location of emitters with respect to the field; $\mathbf{f}(\mathbf{r})$ is the mode field profile, $\mathbf{r_e}$ is the location of the emitter, and $\mathbf{d}$ is its dipole moment. Assuming, as in Hill et al. [25], random orientation of dipole moments, $\zeta = |\mathbf{f}(\mathbf{r_e})|^2$. The scaling of $\mathbf{f}(\mathbf{r_e})$ is arbitrary and has no effect on F_{cav}; it is usually chosen so that $\mathbf{f}(\mathbf{r_e}) = 1$ at the field antinode [50, 64]. With this convention, V_{eff} for the mode shown in 3.2d evaluates to $0.05\,\mu\mathrm{m}^3$ (Q=1,004, $\lambda_{cav} = 1.538\,\mu\mathrm{m}$, cavity dimensions $r_c = 260\,\mathrm{nm}$, $\Delta = 200\,\mathrm{nm}$, gain block height $h_c = 480\,\mathrm{nm}$). The carriers are not all located at field antinodes (which would have produced $\zeta = 1$), but neither are they uniformly distributed over the gain volume, because intensive recombination at the antinodes draws carrier diffusion toward that region [25]. We thus expect ζ to take an intermediate value between unity and the volume average $\frac{1}{V_{gain}}\iiint_{V_{gain}}|\mathbf{f}(\mathbf{r})|^2 d^3\mathbf{r} = 0.456$ (where V_{gain} is the gain volume), yielding the Purcell factor F_{cav} between 19 and 41.

3.7.3 Fabrication

The (undoped) gain layer was grown on an InP wafer in the InGaAsP quaternary system using MOCVD (fabricated at OEpic Inc.). Both bulk gain and

MQWs were used and both exhibited lasing, but the measured results presented are all from the MQW samples. The MQW was comprised of 16 10nm thick wells ($\mathrm{In_{x=0.560}Ga_{1\text{-}x}As_{y=0.938}P_{1\text{-}y}}$) embedded in 17 20 nm thick barriers ($\mathrm{In_{x=0.734}Ga_{1\text{-}x}}$ $\mathrm{As_{y=0.571}P_{1\text{-}y}}$), with a PL emission peak at 1,546 nm. The nanolaser fabrication process consisted of the following steps: 1) HSQ resist was spun onto the InGaAsP/InP wafer and patterned into dots via e-beam lithography in a Raith 50 e-beam writer; 2) The dots were etched into pillars using a $\mathrm{CH_4/H_2/Ar}$(4:20:20 sccm) RIE process in a Trion etcher at 150 W and 30 mT; 3) Subsequently, the samples were cleaned with $\mathrm{O_2}$ plasma and a buffered oxide etch; 4) silica was deposited on the pillars via $\mathrm{SiH_4/N_2O}$ PECVD; 5) The metallization was done using a Denton 18 sputter coater. Initially gold was used for the metal layer but its weak adhesion properties caused the gain disks to fall out of their metal shell in later steps. Simulations showed that the use of an intermediate adhesion layer such as titanium would cause a drastic drop in the cavity Q. Therefore aluminum was used directly, since at 1,550 nm its optical properties are on a par with gold, but it has much better adhesion; 6) After covering the metal coated pillars with SU-8 polymer and bonding to a glass substrate, the InP substrate was removed with a selective HCl etch in the final step of the process.

3.7.4 Characterization results

Measurement of the light–light curves and the spectral evolution of the laser emission was performed on a sample with major and minor diameters of 490 nm and 420 nm, respectively. The pump was focused to a spot size of approximately 8µm×8µm in diameter (FWHM) with a ×20 long working-distance objective. The pump laser was a 1,064 nm fiber laser operating in either CW mode or pulsed mode (300 kHz and pulse width of 12 ns). During the measurement, the stability of the measurement system was found to be better than 0.25% per hour. The data points were obtained by integrating the emission spectrum over a 20 nm window centered around the lasing peak (from 1,420 nm to 1,440 nm). To observe the spatial coherence of the beam after the onset of lasing, ×50 long working-distance objective was used. The sample was defocused from the object plane of the imaging system by approximately 10 µm (away from the objective) and the resulting diffracted mode pattern was imaged onto the camera. The transition from PL (using a CW pump) to lasing (using a pulsed pump) is dramatically shown by the appearance of Airy-like patterns which indicate the increase of emission coherence. The null feature at the center of the defocused pattern may be a result of a TE_{01} lasing mode (which also has a null in the center), but other effects (such as imaging aberrations) may also be the source of this feature.

The polarization of the emitted beam is elliptical, with a large portion of the lasing power residing in one polarization. This does not agree with the expected azimuthal polarization of a TE_{01} lasing mode. The reason for this discrepancy is due to the slight ellipticity of the structures which affects the emitted beam in two ways. First, the ellipticity splits the degenerate TE_{01} mode and results in a slightly elliptical lasing mode in the gain core section. Secondly, the elliptic metal coated dielectric section that connects the gain core to free space acts as a weak polarizer and preferentially transmits one polarization, resulting in a rather strong linearly polarized component at the exit aperture of the laser.

For the index of refraction estimation, nine different lasers were selected and pumped with a large area beam (approximately 30 µm×30 µm in diameter). The major and minor diameters of the nine lasing samples were individually measured using SEM measurements of their base apertures. The gain core was modeled as a three layer stack of elliptical truncated cones to account for the etch profile and slight RIE induced erosion of the core. Then the resonant eigenmodes for each sample were found using a nominal refractive index derived from the unpumped dispersion curve (Figure 3.6, red dashed curve). Based on the estimated gain spectrum of the material, the location of the modes and their lasing threshold, the most likely eigenmode for lasing was found for each cavity and the refractive index was perturbed so that the eigenmode coincided with its corresponding experimental lasing line, resulting in the green data points in Figure 3.6. It is interesting to note that even though for each sample several different eigenmodes were possible lasing candidates, in every case the process of finding the best eigenmode resulted in one of the non-degenerate TE_{012}-like modes being chosen, indicating that the optimized cavity shield thickness is (to some extent) insensitive to variations of the core size. The error bars were calculated assuming a 5 nm error in measuring the laser diameter. Using a least squares fit over the set of lasing points and assuming a constant refractive index drop across the spectrum of interest, the unpumped dispersion curve was down shifted by 0.102 RIU, resulting in the pumped dispersion curve (solid blue line in Figure 3.6).

Chapter 3, in full, is a reprint of the material as it appears in "Room-temperature subwavelength metallo-dielectric lasers," M. Nezhad, A. Simic, O. Bondarenko, B. Slutsky, A. Mizrahi, L. Feng, V. Lomakin, and Y. Fainman, *Nature Photonics*, vol. 4, no. 6, pp. 395–399, 2010. The dissertation author was the primary co-investigator and coauthor of this paper.

Chapter 4

Cryogenic operation of nanolaser structures

4.1 Introduction

In Chapter 3 we demonstrated how one can design, fabricate and characterize sub-wavelength scale lasers that operate at the room temperature. We were, however, also faced with a great deal of difficulties in the process. First and foremost was the issue of heat buildup in the laser cavity. As we showed, the active core is surrounded by SiO_2 which is a poor heat conducting material, especially when grown in thin films ($100 - 500\,\mathrm{nm}$) [65] such as we have here. The resulting heat buildup can degrade the optical gain [66]. This degradation means that higher pump power is needed to achieve the necessary gain for lasing, which in turn generates even more heat and degrades the optical gain even further, which leads to a permanent damage and in some instances catastrophic failure of the devices. For that reason, reliable multiple measurements of the same sample are impossible. This gain degradation affects smaller cavities much more than the large ones, and this is why we were able to confirm room temperature lasing only in barely sub-wavelength structures (recall that our device had $d/\lambda \approx 0.9$).

To investigate these problems further we decided to look at the performance of our devices at cryogenic temperatures. We wanted to investigate the implication of low temperature on the size of lasing devices. We also wanted to see if the degradation of performance with prolonged exposure to higher pump powers is still present at these temperatures. This chapter deals with these efforts and their results.

4.2 Advantages of cryogenic operation

Cryogenic operation of micro/nano lasers is generally desirable due to reduction of the thermal noise. Namely, the amplitudes of the vibrational modes are drastically reduced (phonons completely vanish at 0 K), which affects electromagnetic performance of both metals and semiconductor gain material. In metals, conductivity is increased, making metals behave more like a perfect conductor [67]. At the same time optical (Joule) losses in the field-metal interaction are reduced. In active semiconductors, such as III-V multiple quantum well structures (MQW), benefits of the cryogenic operation are increased gain [68], lower inherent losses, and narrowing of the gain spectrum. Narrowing of the emission spectrum occurs because of the lower number of allowed transitions from conduction to valence band, while lower loss increases photon emission (reduced reabsorption). Both of these features are clearly visible in Figure 4.1a where a 500 nm bulk InGaAsP layer was optically excited by a 1,064 nm laser operating in the continuous wave (CW) regime, while the sample was cooled from 295 K down to 45 K. Figure 4.1b is showing the increase in emission peak (normalized to the one at room temperature) and there it can be seen that the peak emission at liquid nitrogen temperature (77 K) is three times higher than at the room temperature.

There is another important effect to be noticed in Figure 4.1a, and that is the blue-shift (increased band-gap) of the photoluminescence (PL) that occurs as the sample is cooled down. In our case, the peak of the PL spectrum shifts towards blue by 60 nm as the sample is cooled down from room temperature to 45 K. This is more clearly represented in Figure 4.2 where data from Figure 4.1 was used to illustrate this blue-shift. This shift is mostly due to the crystal lattice contraction at lower temperatures which in turn affects electron-lattice interaction,

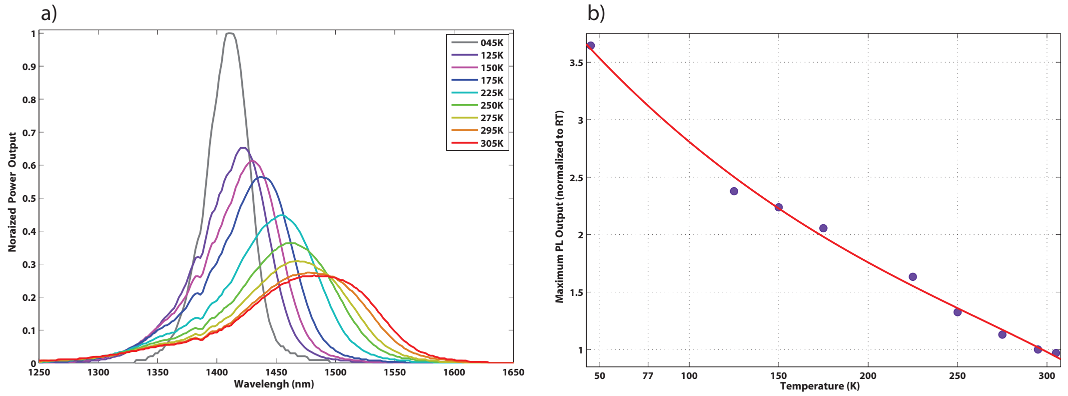

Figure 4.1: **(a)** Photoluminescence (PL) spectrum of 500 nm thick layer of bulk InGaAsP as a function of temperature. InGaAsP was optically excited using a 1,064 nm CW laser; **(b)** Maximum PL output of figure **(a)** as a function of temperature (red line represents a fit). Data is normalized to PL output at room temperature so that benefit of cooling is apparent.

altering the band gap. The red line in Figure 4.2 represents a theoretical fit to an empirical model of band gap dependence on temperature for semiconductors [69]. This dependence is is given as $E_g = E_0 - \alpha T^2/(T + \beta)$ where α and β are fitting parameters, often called Varshni parameters (with positive value for most semiconductors), and E_0 is the band gap at 0 K. Our fit yields coefficients that agree well with the published data [70–72], given that the band gap of $\mathrm{In_xGa_{1\text{-}x}As_yP_{1\text{-}y}}$ varies with composition (values of x and y).

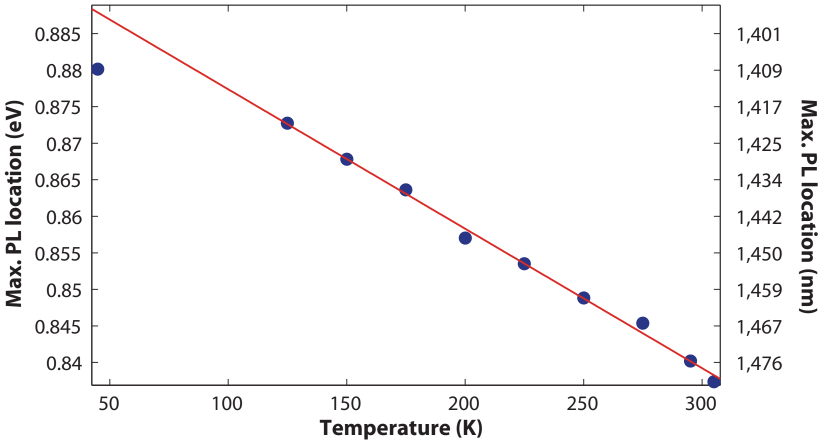

Figure 4.2: Peak of photoluminescence (PL) spectrum from Figure 4.1 as a function of temperature. Red line represents a theoretical fit [69].

4.3 Experimental results of cryogenic operation

The preceding section outlined the reasons behind our interest in performance of our nanolasers at low temperatures. We expect the performance of the lasers to be improved in (*i*) lowering the lasing threshold of the particular structures as they are cooled down (due to lower loss and higher gain), and (*ii*) reducing the minimum size for laser operation. The first experiment we performed was to verify the prediction about the lower lasing threshold. Figure 4.3a shows light-light curves at several temperatures for a sample with $D_{core} \approx 1\,\mu\text{m}$. As expected, the lasing threshold is significantly lower at 77 K than at room temperature. This point is nicely summarized in Figure 4.3b where we can see that threshold pump power is reduced by a factor of *ten* as we cool the sample from room temperature down to 77 K. Another conclusion that can be drawn, also as expected, is that the efficiency of the nanolaser is improved with the reduction of temperature. This is evident by the steepening of the lasing part of the L-L curves. The same is true, to a lesser extent, for the PL part of the curve. Since the laser power is measured in arbitrary units, it is not possible to know the absolute efficiency. For more information about the difficulties in the absolute power measurements of the nanolaser output see Appendix C.

4.3.1 Temperature vs. size tradeoff

In our attempt to fully understand the tradeoff between the size of the laser and the temperature at which it operates we investigated the performance of an entire array of samples of varying sizes (Figure 4.4) at room temperature (295 K) and liquid nitrogen (77 K).

Generally speaking, the color map in Figure 4.4 shows exactly the expected behavior. Larger lasers (circle diameter in figure corresponds to the sample size) are able to lase at room temperature (indicated by red color), but for sizes below $D_{core} \approx 350\,\text{nm}$ the threshold gain requirements are such that can only be satisfied at low temperature (indicated by blue color). Black color in Figure 4.4 indicates the samples that were too small to lase even at the 77 K. There are, however,

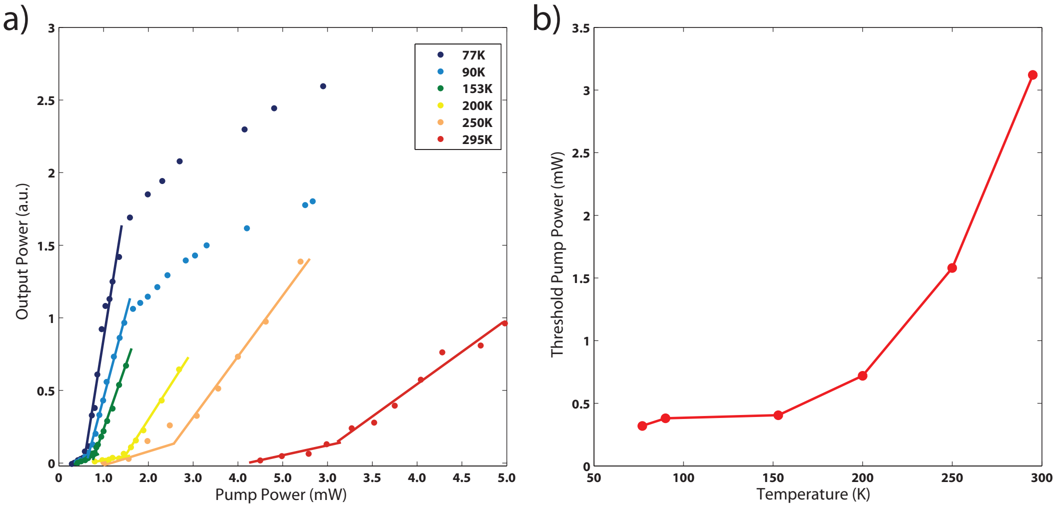

Figure 4.3: **(a)** Light-light curves for nanolaser with D_{core} ≈1 µm at different temperatures. Note the lower threshold and improved lasing efficiency (steeper curve) as the temperature drops. Also note the saturation that occurs at higher pump powers for at 77 and 95 K. **(b)** Lasing threshold pump power as a function of temperature for the same structure. Threshold is reduced by a factor of 10 when sample is cooled from 295 K to 77 K

peculiarities that surface upon closer inspection. Figure 4.5 shows a sample of collected data sorted in four columns (subset of the same data is presented in Table 4.1 for greater clarity). First, there is a range of core sizes for which lasers operate at room temperature. This is precisely what was expected given the results presented in Chapter 3. More surprising were two lasers with D_{core} in the 600 − 700 nm range that only operate at 77 K, even though different lasers with smaller size operate at room temperature. The reason for that is that, as noted before, the gain spectrum blue-shifts with the reduced temperature. So if the modes supported by a particular cavity are in the spectral region that has little gain available at room temperature (gain maximum at RT is at 1,550 nm), then as the sample is cooled and gain becomes available, lasing becomes possible.

A more interesting example is that of the sample with $D_{core} = 604$ nm. Here we have a sample that only operates at room temperature, but it does not operate at 77 K, which is somewhat counterintuitive. One would expect everything that works at room temperature to work at 77 K with improved performance. As

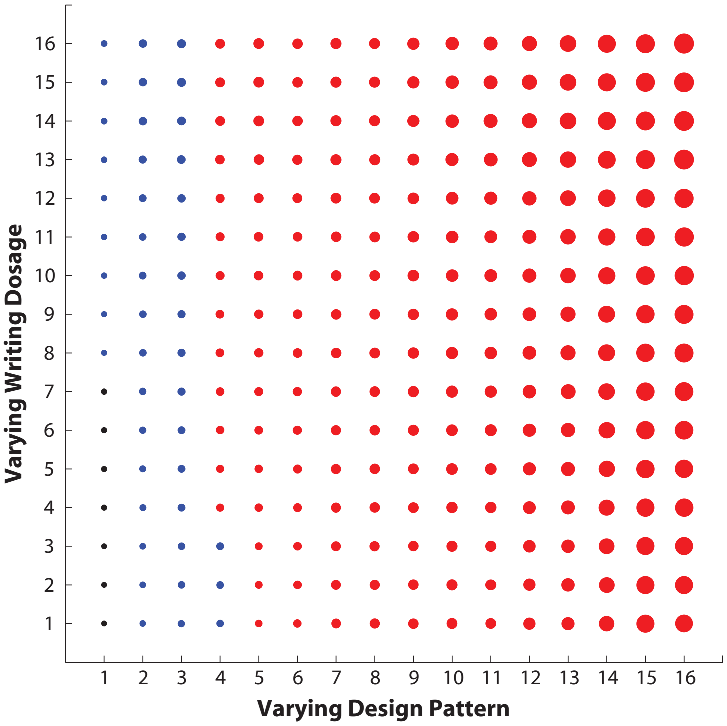

Figure 4.4: Size (D_{core}) map of the array of nanolasers (individual samples are drawn to scale (relative to one another), while the separation between the samples is much larger in reality). Each of the 16 columns was written with a different size (large steps), and each of the rows was written using different dosage in the e-beam, which introduced small size variations. Resulting pattern has values of D_{core} from 260 nm (lower left corner) to 980 nm (upper right corner). Red is used for samples that lased at 295 K, blue for the samples that only lased at 77 K and black for the samples that didn't lase at all.

Table 4.1: Laser size vs. temperature tradeoff — selection of data from Figure 4.5

D_{core} (nm)	284	357	457	554	604	687	756	844	951
77 K	✓	✓	✓	✓	×	✓	✓	✓	✓
295 K	×	✓	✓	✓	✓	×	✓	✓	✓

we can see, that is not necessarily the case. The reason for this peculiarity is again the spectral shift in gain spectrum with reduced temperature, and this can be seen in Figure 4.6. Here the lasing peak at 295 K occurs at 1,605 nm which is towards the tail end of the gain spectrum at room temperature. So it is not the most efficient laser at room temperature, but it still has enough gain to work.

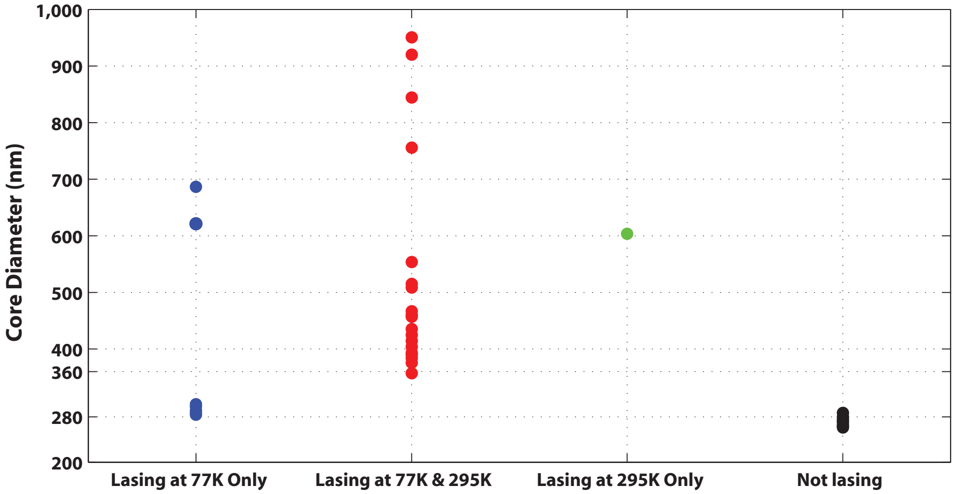

Figure 4.5: Size vs. Temperature — each point represents an individually measured laser cavity of different size (y-axis), which falls in one of the four lasing categories (x-axis). The unexpected category is the lasers that *only* lase at room temperature.

At 77 K however, with gain blue-shifted by $\sim$ 75 nm (Figure 4.1a[1]) there was not enough gain available to sustain the lasing for the 1,605 nm mode, and the mode at 1,440 nm proved to be too lossy to achieve lasing.

4.3.2 Lasing results at 77 K

Even with these peculiarities, low temperature operation is certainly beneficial for the pursuit of smallest laser that can work. It is important however to consider the drawbacks just outlined when judging these benefits. Still, looking at Figures 4.4 and 4.5 and Table 4.1, we can indeed see that there are small lasers that operate at 77 K which stand no chance of lasing at room temperature. The smallest laser that operated at 77 K had a gain core diameter $D_{core} = 284\,\text{nm}$, with total diameter amounting to 840 nm. These results are summarized in Figure 4.7.

---

[1] Although data presented in Figure 4.1 is taken for 500 nm layer of bulk InGaAsP, and lasers measured here were fabricated using InGaAsP MQW structure, roughly the same magnitude of blue-shift of PL was measured when sample was cooled down to 77 K.

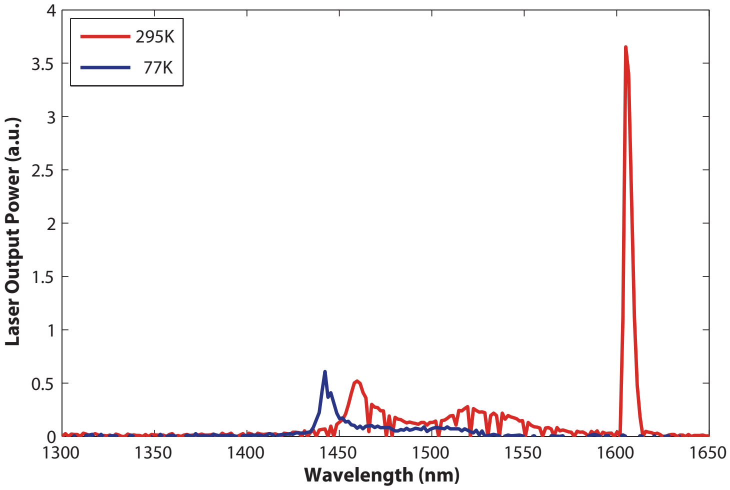

Figure 4.6: Emission spectra for $D_{core} = 604\,\text{nm}$ laser at 295 K and 77 K. Supported mode dictated by the cavity geometry is at long wavelength (1,600 nm) and thus sees no gain when it is cooled down due to blue-shift.

Spectral evolution clearly shows a gradual transition from a rather broad photoluminescence spectrum over emerging amplified spontaneous emission peak to a final narrow lasing peak that dominates the entire spectrum. The inset in Figure 4.7b shows the spectrum of the lasing line at high resolution. It is obvious that the spectrum is in great agreement with the predicted Lorenzian line shape, and that the line is quite narrow ($\Delta\lambda = 1.26\,\text{nm}$) considering the size of the device.

The light-light curve by itself is less convincing, and that is due to the very gradual transition from PL to lasing which is quite common in lasers at these scales. One important thing to note is the total diameter of the device $D_{total} = 840\,\text{nm}$. This is considerably more than the core diameter due to an unnecessarily large SiO_2 shield. The problem is that our fabrication technique (as outlined in Chapter 3) is such that we deposit uniform SiO_2 shield over the entire array of samples with different core sizes (as shown in Figure 4.4). Since the thickness of the shield is optimized for room temperature operation of larger lasers, these smaller scale lasers end up with a total size that is needlessly large. Moreover, the heights of the dielectric and air plugs (Figure 3.2c) are also universally defined for the entire sample array, which makes them taller than needed for the small lasers. This in

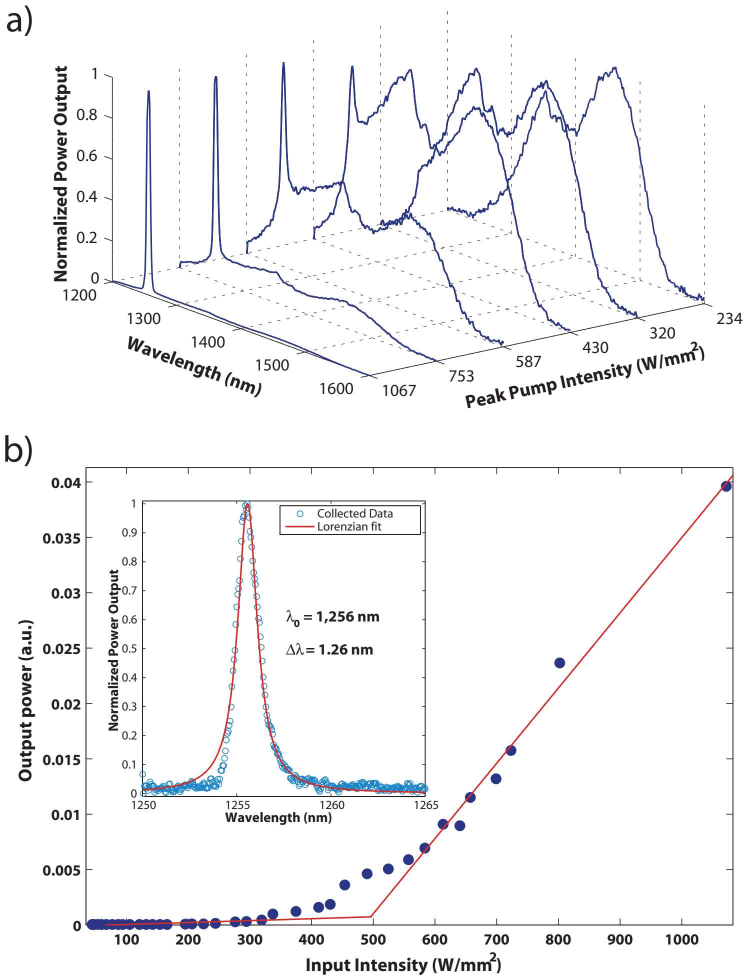

Figure 4.7: (a) Spectral evolution of a $D_{core} = 284\,\text{nm}$ laser operating at 77 K. Spectrum transitions from broad emission PL at lower pump powers to emergence of the ASE peak to a narrow lasing line at the end. (b) Light-light curve is shown. Transition between the PL and lasing parts is rather gradual which is common with lasers of this size. Inset shows a narrow Lorenzian shaped line with $\Delta\lambda = 1.26\,\text{nm}$ centered at 1,256 nm.

turn creates problems with pump penetration into (as seen in Figure 3.7) and light extraction from the lasing cavity, making the laser seem artificially less efficient.

4.4 Discussion and conclusion

It is somewhat difficult to judge the overall benefits of low temperature operation of nanolasers. First, it depends on what is meant by “low temperature”. Here we presented the data on only two temperatures, 295 K and 77 K. It would be ideal to have a more comprehensive study covering the gradient of temperatures between the two points we chose, and examine how the lasing threshold changes with size and temperature. Unfortunately, we could not make such a study due to the following problems.

4.4.1 Degradation of nanolaser performance with time

The first and probably most significant problem is the degradation of the laser performance with usage. In other words, we are unable to perform the nondestructive measurements needed for such a detailed characterization. At best, laser performance diminishes after (sometimes even during) the measurements, and at worst the laser simply burns out. The reasons for this effect remain unclear. Cryogenic operation helps somewhat by lowering the metal loss, improving the gain and thus reducing the pump power requirements. Another benefit is reduced ambient temperature which leads to less heat buildup in the gain core. However, this heat buildup has also to do with the thermal conductivity of the gain material and its surroundings [65] (SiO_2 and air), and there is little that can be done to help that. One option is to use a better thermal conductor for the dielectric shield, such as Al_2O_3, but this fabrication technique was not available to us at the time of these experiments. Another possibility is modifying the fabrication technique to eliminate the air gap and replace it with SiO_2, and Chapter 5 deals with that endeavor in great detail.

Use of shorter pump pulses can seem beneficial too, but that creates a different set of problems. With our optical pump operating at 10 ns and 300 kHz repetition rate, the pulses are still sufficiently short to reduce heating, but long enough (compared to the repetition rate) not to affect the signal to noise ratio too badly (in our case we have a factor of 277). If the pulses were to go down to ps range, not only would SNR suffer, but we would start encountering nonlinear effects.

One possibility, although not perfect, would be to fabricate an array with many identical samples. That way, at least in theory, since all of them are the same, when one dies, we simply move to the next one and continue the measurements. Even if we allow for some small variations due to fabrication process, with enough samples we could statistically treat the data and get what we need. The problem however is that at these scales, even errors of $5 - 10\,\mathrm{nm}$ in fabrication profoundly alter the electromagnetic properties of these devices. To test the fabrication repeatability (and demonstrate lack thereof) we wrote two identical arrays (such as depicted in Figure 4.4) labeled "a" and "b", one next to another ($\sim 400\mu\mathrm{m}$ apart) on the same gain chip. All of the fabrication steps were performed on the entire chip at once, meaning that two finished samples underwent *exactly* the same fabrication process. To test this, we compared the optical performance of pairs of samples with exactly the same nominal size that are located on a different array ("a" or "b"). A small selection of these results is presented in Figure 4.8.

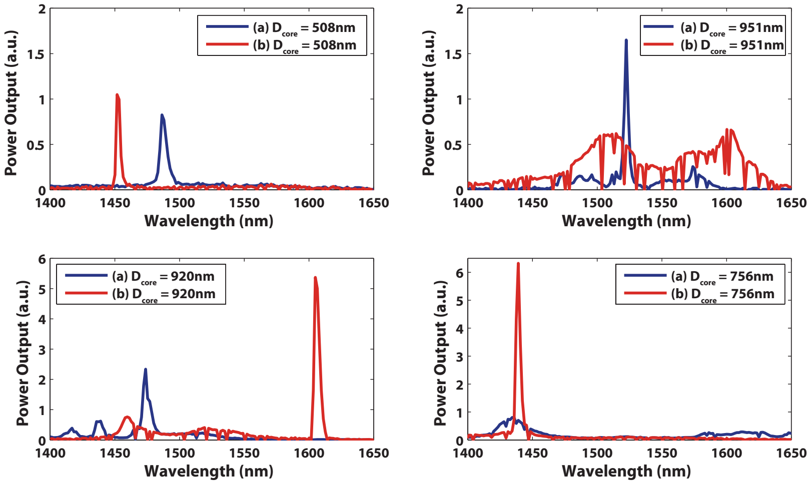

Figure 4.8: Emission spectra from four pairs of nominally identical nanolasers. All nanolaser labeled with (a) and colored blue are from one array (as in Figure 4.4), while the others are form the second array. Both arrays are written at the same time on the same chip, one next to another, and processed *identically*. Yet, performance across the patterns is vastly different.

Unfortunately, the results are discouraging. They prove that with our current fabrication process we are unable to produce exactly the same nanolaser twice, so any hope for measurement over multiple samples of the same size is unsubstantiated. In Figure 4.8 we see varying degrees of agreement between the spectra taken from two sample arrays. From reasonable agreement (top-left) where the lasing peak shifted "only" by 40 nm over the situations where peak is in the same place but lases only on one of the samples (bottom-right), to wildly different (~ 120 nm) lasing peak locations to complete failure of one of the samples to produce any stimulated emission. This proves that different samples, even if they are nominally the same size, and processed and fabricated *identically*, at the same time (eliminating the fluctuation in machine performance), cannot be compared head-to-head. So this coupled with the decay problem we already discussed places a stringent limit on the type and number of the experiments we can perform.

4.4.2 Lasing at different modes at 77 K

Another problem we encountered that makes it hard to directly compare the performance of the given nanolaser at room temperature and at 77 K is that some times lasing occurs at a different mode as the temperature is lowered. This is a result of change in the gain profile as a function of temperature as we discussed before, and the fact that these nanolaser cavities, depending on the particular geometry, can support several modes. Figure 4.9 shows two different nanolasers, one with $D_{core} = 357\,\text{nm}$ (solid lines), and another with $D_{core} = 457\,\text{nm}$ (dashed lines), characterized at two temperatures. The smaller laser lases at the same mode at both temperatures, thus enabling us to say exactly how much improvement did the cooling bring. The same comparison in the larger nanolaser it is a bit trickier, since it operates at different modes at two temperatures.

Another interesting possibility is multi-mode operation of the nanolasers. If the geometry is large enough to support several distinct modes that all fall within the gain spectrum, and additionally these modes have little or no physical overlap in the gain medium (their electromagnetic fields don't occupy the same physical space within the gain core), it is possible for more than one of these modes to

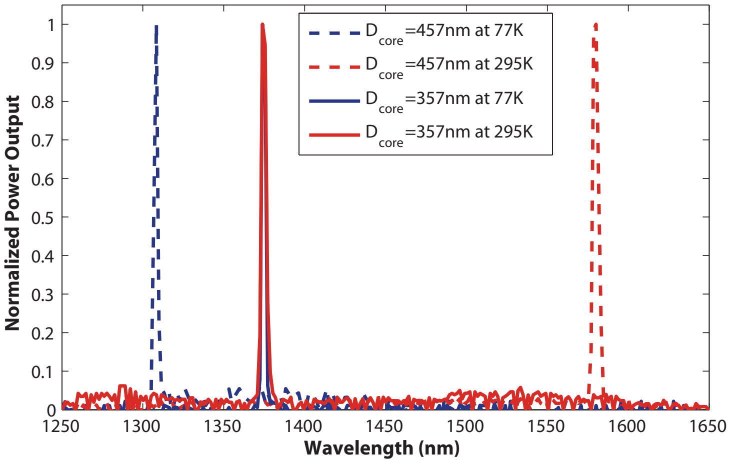

Figure 4.9: Emission spectra from two nanolasers taken at 295 K (red lines) and 77 K (blue lines). Nanolaser with $D_{core} = 357\,\text{nm}$ (solid lines) lases at the same wavelength (1,376 nm) both at room temperature and at the liquid nitrogen. Larger nanolaser ($D_{core} = 457\,\text{nm}$ — dashed lines) however lases at two distinct modes at two different temperatures, due to the blue-shift of the gain spectrum as the sample is cooled down.

actually lase simultaneously. This is in large part due to the lower metal loss and higher gain that is available to us at cryogenic temperatures. Spectra for one such laser ($D_{core} \approx 1\mu\text{m}$) are presented in Figure 4.10. Here we see, as the pump power is increased, first the PL peak at 1,420 nm, then first lasing peak emerges at 1,377 nm followed by the emergence of another peak at 1,352 nm, and at the end a third peak appears at 1,501 nm. With multiple lasing peaks competing for the same available gain, it becomes impossible to accurately judge the benefit brought by cooling the sample down to 77 K.

4.4.3 Conclusion

We set out to investigate the operation of these nanolasers at cryogenic temperatures, with its benefits and challenges. While lower temperature certainly improved the gain of the semiconductor and reduced the loss of the metal, it also brought about some complications. As we saw, characteristics of nanolaser performance often also changed, making it hard to directly compare and quantify

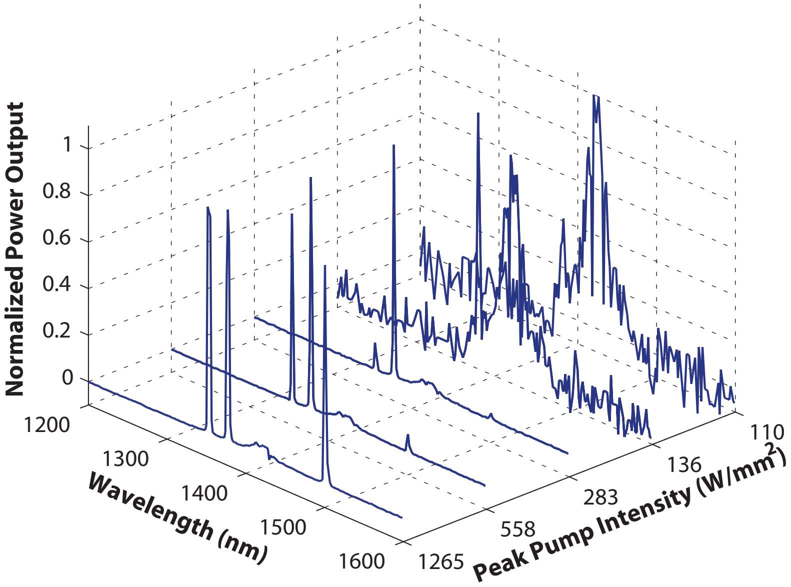

Figure 4.10: Emission spectra from two nanolasers taken at 295 K (red lines) and 77 K (blue lines). Nanolaser with $D_{core} = 357\,\mathrm{nm}$ (solid lines) lases at the same wavelength (1,376 nm) both at room temperature and at the liquid nitrogen. Larger nanolaser ($D_{core} = 457\,\mathrm{nm}$ — dashed lines) however lases at two distinct modes at two different temperatures, due to the blue-shift of the gain spectrum as the sample is cooled down.

the benefit of cooling. Additionally, operation at 77 K is acceptable in the lab environment, but for real-world practical use it may be too cumbersome. Even if we were to use thermoelectric coolers, to reduce the operational temperature of these nanolasers to say 240 K (−33 °C) we still have a number of issues to deal with, such as moisture condensation and freezing which would considerably degrade the performance. But on the positive side, low temperature operation certainly opens a pathway to exploration of interesting new properties of these nanolasers.

Chapter 5

Wafer bonded sub-wavelength metallo-dielectric laser

5.1 Introduction

Realization of silicon compatible active optical components is critical for creating integrated silicon photonic circuits, and a major step towards integration with CMOS-compatible platforms. Silicon has good thermoconductive properties, high quality oxide, low cost, and is available in high quality wafers, making it invaluable for integrated electrical circuits and waveguides. Unfortunately, the indirect bandgap of silicon poses a fundamental barrier to enabling light amplification and stimulated emission in this material. Successful advances toward overcoming this limitation include demonstration of silicon Raman lasers [73] and light emission in silicon-based nanoengineered materials [74]. However, Raman laser operation is based on optical scattering, which makes it essentially limited to operation under external optical pumping. Silicon nanostructures, in turn, suffer from low gain, and therefore, low efficiency.

An alternative solution is to build hybrid optical devices through integration of III-V gain with silicon [75] using wafer bonding. III-V semiconductor compounds offer the benefits of a direct energy bandgap with wide achievable range, and high carrier mobility. This makes the III-V material system optimal for active optical elements and logical devices such as lasers, switches, and modulators. In addition to integration with silicon, another major goal of current photonics research is to reduce device footprints. Miniaturization is of great importance for the realization of compact photonic circuits for optical interconnects on-chip optical communication and sensing. Many applications often require high density packaging of laser structures, and therefore three dimensional minimization of the lasers is ultimately desired.

To date, several different sub-wavelength lasing structures were reported by a few research groups [24, 25, 56, 76–78], but integration of sub-wavelength lasers with passive silicon photonics still remains a challenge. Earlier we demonstrated room-temperature operation in sub-wavelength metallo-dielectric lasers [51, 77], where the dielectric shield between metal cavity and InGaAsP gain core allows us to achieve lasing at room temperature through metal loss reduction [51]. However, building a practical ultra-compact on-chip device prompts us to address a few issues that include integration of the optical gain material with a silicon-on-insulator (SOI) wafer, assembly of an electrically injected laser cavity and laser-to-waveguide mode coupling. In the original design, the nanolaser is optically pumped and mounted on a glass slide with the output light propagating in free space (Figure 5.1a). The wafer bonding approach offers a path to realization of an electrically pumped sub-wavelength laser with vertical mode coupling to a silicon photonic waveguide by means of a slanted mirror, for example [79].

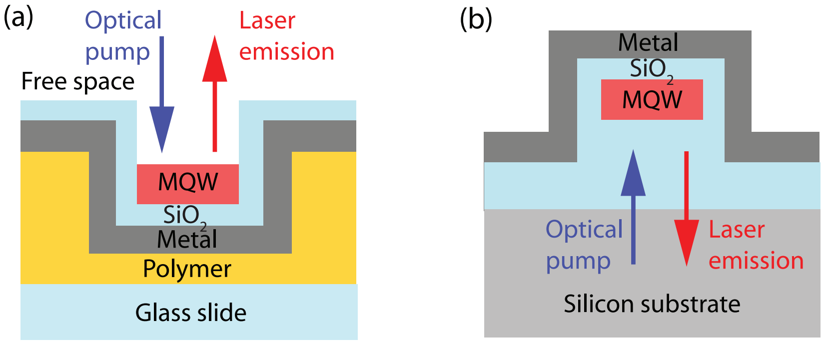

Figure 5.1: **(a)** Scheme of the original sub-wavelength metallo-dielectric laser setup as from [77]; **(b)** Scheme of a wafer bonded metallo-dielectric laser to be reported in this paper.

In order to exclusively investigate wafer bonding problems, we choose to keep the original cavity mode of the optically pumped nanolaser [77] intact. Thus, the III-V-to-silicon wafer bonding has to be mediated by low refractive index material, such as SiO_2, to achieve vertical mode confinement (Figure 5.1b). The mediator layer has to be thick enough to reproduce the 500 nm air plug in the original design. Next, we need to select a reliable and versatile wafer bonding method, which could be used for both III-V-to-Si and III-V-to-SiO_2/Si integration.

The wide variety of available wafer bonding techniques includes fusion bonding, anodic bonding, solder bonding, eutectic bonding, thermocompression bonding, direct metal-to-metal bonding, ultrasonic bonding, low-temperature melting glass bonding, and adhesive bonding [80]. Our choice was determined by the cavity design, which required a direct low temperature (below 400 °C) bond of an InGaAsP multiple quantum well (MQW) active layer to a silicon base. Conventional high temperature direct wafer bonding (fusion bonding) is known to have an adverse effect on the III-V layer quality due to a thermal expansion constant mismatch of the bonded materials. Some of the available low temperature wafer bonding methods may be useful, but would require additional studies of the bonding mediator's optical and material properties (adhesive wafer bonding), its possible chemical interaction with the gain layer (anodic wafer bonding) and incorporation of these new layers into the original nanolaser model.

Recently, Liang et al. reported a plasma assisted wafer bonding method [81,82], which they successfully used for realization SOI-compatible optoelectronic devices [75]. Hence, in this work we demonstrate a silicon-compatible metallo-dielectric nanolaser and investigate the feasibility of this fabrication approach for integration of the device with silicon photonics platform.

5.2 Design and Simulations

Microdisk resonators with conventional whispering gallery mode (WGM) designs can be reduced to sub-wavelength scale [43], but the corresponding mode for the small structure is loosely bound, such that its evanescent tail is spread far beyond the physical resonator boundaries. This creates two problems. First, it increases the threshold requirements since the mode/gain overlap is reduced. Second, coupling between the modes of neighboring resonators makes the WGM resonators unsuitable for densely packed laser arrays. These issues can be solved by enclosing the semiconductor resonator in a metal cavity [25]. While the metal cavity introduces strong mode confinement and thereby increases the mode-gain overlap, it also introduces high Ohmic losses. The last circumstance poses a difficulty on the way to room temperature lasing in sub-wavelength metallic resonators.

Our approach to overcoming the metal losses is to incorporate a dielectric shield layer between the metal and semiconductor [51]. The shield thickness can be optimized for a fixed outer diameter of the laser. For an optimum shield thickness the losses reduce such that threshold gain is small enough for room temperature operation. In this case, we are still benefiting from the metal confinement, but the dielectric shield separates the largest portion of the mode, concentrated in the high index gain core (~ 3.5 for bulk InGaAsP), from direct interaction with the metal. Excessive shield thickness is detrimental, because the dielectric layer takes space that could otherwise be filled with the gain medium.

Here we attempt to adapt this approach for an InGaAsP MQW gain layer, wafer bonded to SiO_2/Si (silicon wafer with thermally grown silicon dioxide layer), using our original design for the InGaAsP/InP material system. Figure 5.2a shows a schematic of a sample metallo-dielectric nanolaser, optimized for minimum lasing threshold at a nominal wavelength of 1,550 nm and outer radius of the resonator $R_{out} = 460\,\mathrm{nm}$. For a structure of these dimensions, the optimal shield thickness (Δ) and gain core radius (R_{core}) are 200 nm and 250 nm, respectively [51]. The gain core of the laser consists of InGaAsP with MQW (the actual composition of the gain layer is summarized in Table 5.1. A layer of metal (silver) confines the electromagnetic fields within the cavity. The gain is separated from the metal by a shield layer of low-index dielectric (SiO_2). The dielectric regions with low effective index above and below the gain cylinder (“plugs”) provide vertical confinement of the resonator mode, as the lasing mode is in cutoff there. The lower plug is comprised of thermal SiO_2, in contrast to the original air plug from our previous work. This setup does not introduce any significant changes in the design, since the refractive index of SiO_2 is only slightly higher (1.46 versus unity for air). Finite element method (FEM) simulation of the laser resonator is shown in Figure 5.2b. The dielectric layer has been optimized for the TE_{012} mode, which has higher wavelength cutoff compared to the other lower order modes, but has the lowest achievable threshold gain of $36\,\mathrm{cm}^{-1}$ for the designed structure [51].

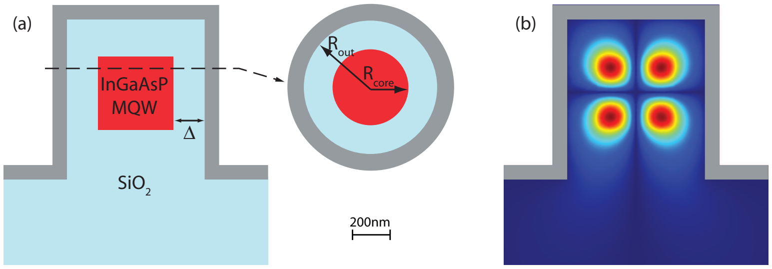

Figure 5.2: **(a)** Schematic drawing of the wafer bonded metallo-dielectric resonator design; **(b)** FEM simulation of TE_{012} mode in metallo-dielectric resonator with $R_{out} = 460\,\mathrm{nm}$, optimized for 1,550 nm wavelength.

5.3 Fabrication

The wafer bonded sub-wavelength metallo-dielectric structures are fabricated from an InGaAsP multiple quantum well gain layer, bonded to a silicon wafer with a SiO_2 layer on top. The complete fabrication scheme is outlined in Figure 5.3. The silicon wafers have a 6 µm thermally grown oxide layer on the surface. The MQW InGaAsP/InP wafer was ordered from OEpic Semiconductor, Inc. This gain layer is comprised of 16, 10 nm thick, wells ($In_{x=0.560}Ga_{1\text{-}x}As_{y=0.938}P_{1\text{-}y}$) embedded in 17, 20nm thick, barriers ($In_{x=0.734}Ga_{1\text{-}x}As_{y=0.571}P_{1\text{-}y}$), epitaxially grown on an InP substrate, $\sim$ 500 nm thickness in total (Table 5.1). InGaAsP MQW active layer bonding to the SiO_2/Si was accomplished through low temperature plasma assisted wafer bonding (Figure 5.3a – c). The process is adapted from the III-V-to-Si bonding procedure recently developed by Liang et al. [81, 82] and is described below.

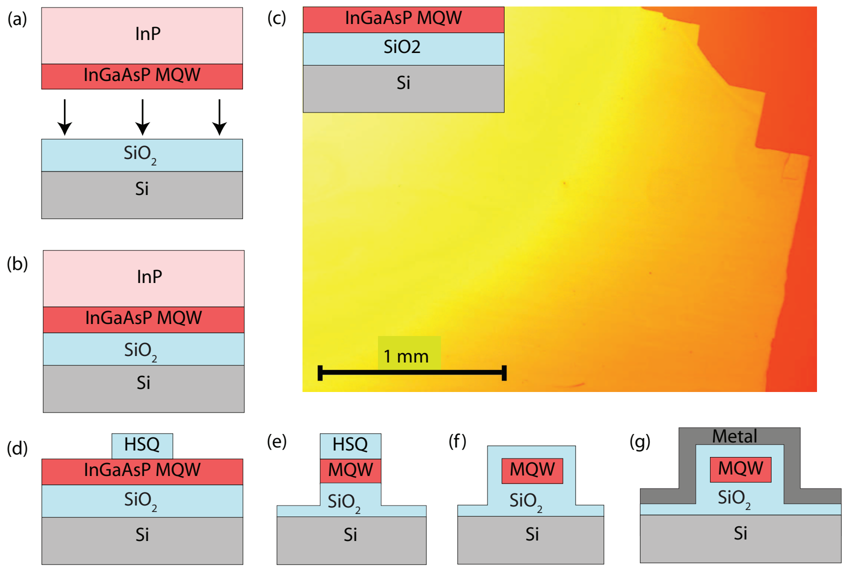

Figure 5.3: Fabrication steps of a wafer bonded metallo-dielectric laser: **(a)** wafer bonding of InGaAsP to SiO_2/SI, **(b)** resultant InP/InGaAsP/SiO_2/Si structure, **(c)** wet etching of InP substrate and the optical microscope image of 500 nm InGaAsP MQW layer bonded to SiO_2/Si chip; **(d)** e-beam lithography patterning; **(e)** laser pillar after two step RIE of InGaAsP and SiO_2 ; **(f)** PECVD of SiO_2 shield; **(g)** metal sputtering (silver)

Table 5.1: Multiple quantum well InGaAsP/InP epitaxial structure

Name	Material	Thickness (Å)	Number of layers
Capping layer	InP	100	1
Active region	$In_{x=0.734}Ga_{1\text{-}x}As_{y=0.571}P_{1\text{-}y}$	200	16
	$In_{x=0.560}Ga_{1\text{-}x}As_{y=0.938}P_{1\text{-}y}$	100	16
	$In_{x=0.734}Ga_{1\text{-}x}As_{y=0.571}P_{1\text{-}y}$	200	1
Substrate	InP	∼ 325 µm	1

The wafer bonding is performed for an InGaAsP/InP chip of $\sim 1\,\text{cm}^2$ area and a SiO_2/Si chip of $\sim 2\,\text{cm}^2$ area. The low temperature bonding starts with ultrasonication of the cleaved wafers in solvents to remove all particles that would inhibit interaction between the surfaces. InGaAsP/InP is dipped in HCl for 10 seconds prior to the wafer bonding to remove the InP capping layer. Ultrasonication in acetone and isopropanol (IPA), followed by thorough DI water rinse are necessary to eliminate particles from the bonding surfaces. This is a crucial step, since a single 1 µm size particle results in an unbonded area of 1 cm^2 [83]. Next, the surfaces are to be stripped of native oxides, organic, and ionic contaminations. The chemical treatment is performed using standard RCA clean (NH_4OH:H_2O_2:H_2O=1:2:10) for 10 minutes at 65 − 75 °C on the InGaAsP/InP chip, and modified RCA clean (HCl:H_2O_2:H_2O =0.2:1:5) for 10 minutes at 80 °C on the SiO_2/Si chip. Then, the InGaAsP/InP chip is immersed into NH_4OH to remove any native oxides and small contaminations left from the previous step, while SiO_2/Si is treated in H_2SO_4:H_2O (3:1) for 10 minutes to strip any traces of organic contaminants. The chemical clean is followed by ultrasonication in acetone, IPA, careful DI water rinse and drying in N_2 flow.

After cleaning, both chips undergo O_2 plasma surface activation in a Trion reactive ion etch (RIE) chamber with 20 mTorr pressure, 30 sccm O_2 flux and 50 W RF power for 45 seconds. The oxygen plasma treatment is immediately followed by a brief rinse in DI water to passivate the active surfaces with hydroxyl (–OH) groups. The water flow also takes away any new particles that may have accumulated during the plasma activation. Next, nitrogen flow-dried chips are manually mated. The Van der Waals force between the –OH groups promotes spontaneous mating of activated surfaces. The pair is annealed for 17 hours at 300 °C in an oven to form strong covalent bonding and encourage out-diffusion of the H_2O and H_2 byproducts through the thick SiO_2 layer from the InGaAsP/SiO_2 interface. Lastly, the InP carrier substrate is selectively etched by HCl from the bonded sample to obtain the composite InGaAs/SiO_2/Si structure (Figure 5.3c).

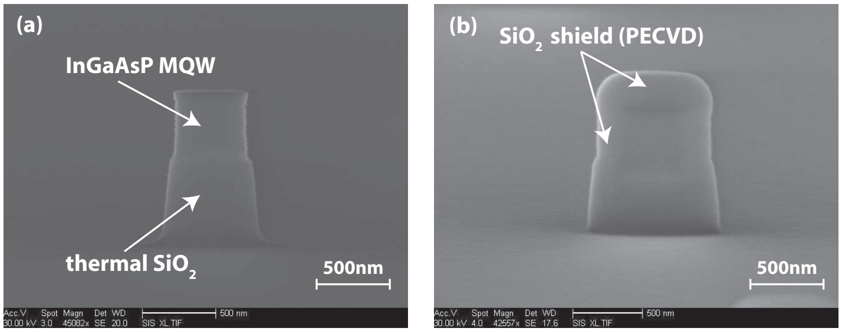

Figure 5.4: SEM micrographs of: **(a)** a laser pillar after two step RIE, and **(b)** the same pillar after PECVD of 200 nm thick SiO_2 layer.

The next step is to perform a double step reactive ion etch (RIE), which has to be carried out on the gain layer and SiO_2 using appropriate etching chemistry for each of the two materials. E-beam lithographic processing was performed on hydrogen silsesquioxane (HSQ) negative resist to create a mask (Figure 5.3d). This is followed by the two-step RIE to form the cylindrical gain core and bottom SiO_2 plug. First, the 500 nm thick InGaAsP MQW layer is dry etched in CH_4:H_2:Ar (4:40:20 sccm) chemistry. Then the SiO_2 layer undergoes CHF_3/Ar (25/25 sccm) RIE to obtain a 500 nm tall SiO_2 post (Figure 5.33e depicts a schematic drawing of the structure after both these steps are performed). The HSQ mask is removed during the last fabrication step along with SiO_2, since its chemical composition is quite similar to that of SiO_2. Next the sample is treated in microwave oxygen plasma (Tepla 100) to eliminate polymer buildup. An SEM image of a sample laser after the cleaning is presented in Figure 5.4a. Next, PECVD of 200 nm thick SiO_2 is carried out to form the low index shield around the InGaAsP core (Figure 5.3f). Corresponding SEM image is shown in Figure 5.4b. In the final step we sputtered silver using a Denton Discovery 18 sputterer on the sample to complete a laser cavity (Figure 5.3g).

5.4 Measurements

We use a standard micro-photoluminescence setup for optical characterization of the wafer bonded nanolasers [77]. For optical pumping we employ 1,064 nm pulsed fiber laser which has a repetition rate of 300 kHz and 12 ns pulse width. The pump beam was focused down to an approximately 8 µm diameter spot size (FWHM), at the sample aperture plane, using 20× microscope objective. The beam intensity profile was observed using an IR InGaAs camera (Indigo Alpha NIR). The profile, together with the measured pump power, allowed us to estimate the peak pump intensity. The light emitted by a nanolaser is collected with the same objective and passed to the detection system. Using a double 4-f imaging system in conjunction with a pump filter (Semrock RazorEdge long wavelength pass), the samples are imaged onto either the IR camera, an electrically cooled In-

GaAs detector, or a monochromator (Spectral Products DK480) with a resolution of 0.35 nm, equipped with a cooled InGaAs detector in a lock-in detection configuration. Total power measurements for the light-light curves are performed using an InGaAs detector. The monochromator is utilized for high resolution measurements in lasing mode to obtain the stimulated emission peak linewidth. Optical measurements at 77 K are performed using a Janis ST-500 cryogenic chamber.

The resonant modes of the structures were found to deviate from the design 1,550 nm wavelength by over 100 nm due to a variety of fabrication factors including slight ellipticity, deviation from nominal size, sidewall curvature, etc. For characterization, we selected devices with resonant modes close 1,550 nm where the InGaAsP MQW material has maximum gain, since these devices may be expected to perform best. Permanent performance degradation has been observed in most devices after prolonged exposure to high pump powers. We speculate that high pump powers cause damage to the gain core. Since the light-light curves provide more conclusive evidence of lasing than linewidth measurements, we have carried out light-light measurement first. This made subsequent linewidth measurements unreliable in some cases, particularly for smaller devices.

We observed room temperature lasing from a sample with approximate gain core radius $R_{core} \approx 450\,\text{nm}$ and peak wavelength of 1,496 nm. A kink in the linear scale light-light curve (Figure 5.5) indicates the onset of lasing at the external threshold pump intensity of $1{,}100\,\text{W/mm}^2$. The same data set is shown in a log-log plot in the inset graph. For an ideal laser the S-shaped curve represents the transition from photoluminescence (PL) mode (the lower linear section with slope 1) through amplified spontaneous emission (ASE) mode (linear section with a slope steeper than 1) into stimulated emission mode (also slope 1). The unity slope indicates a linear dependence of output power on input pump power. The stimulated emission spectrum (the upper inset in Figure 5.5) has been measured after the light-light curve, and is probably affected by material degradation discussed earlier. Other similar sized devices exhibited room temperature linewidths between ~ 1.5 and 5 nm.

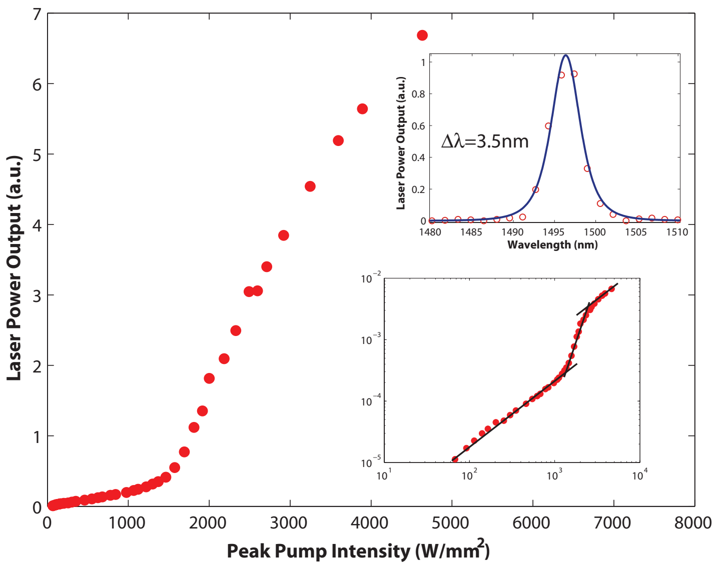

Figure 5.5: Room temperature light-light curve for a nanolaser with gain core radius of $R_{core} = 450\,\mathrm{nm}$. The same data set is shown in the bottom inset as a log-log plot. The upper inset is the lasing spectrum taken with spectrometer; measured linewidth is 3.5 nm

Room temperature lasing from smaller samples ($R_{core} \approx 250\,\mathrm{nm}$) exhibited severe drop of the stimulated emission peak intensity over time, especially after the samples had been subjected to high pump powers. That prevented reliable light-light curve measurements of small (sub-wavelength) samples. To achieve lasing at lower pumping levels, we also performed optical measurements at 77 K, with samples placed in a cryogenic chamber. The light-light curves for both $R_{core} \approx 450\,\mathrm{nm}$ (Figure 5.6) and 250 nm (Figure 5.7) are presented, with the corresponding log-log curves on the inset graphs.

For the nanolaser with $R_{core} \approx 450\,\mathrm{nm}$ and peak wavelength of 1,508 nm, the threshold at 77 K is reduced to 100 W/mm^2, which is approximately 10 times lower compared to the RT results for a sample of the same geometry. The linewidth is measured to be 0.35 nm, from the high-resolution spectrum shown on the upper inset of Figure 5.6. The significant linewidth narrowing at 77 K compared to the room temperature width is an expected phenomenon, which originates from reduced cavity losses, increased output power [84] and smaller linewidth enhance-

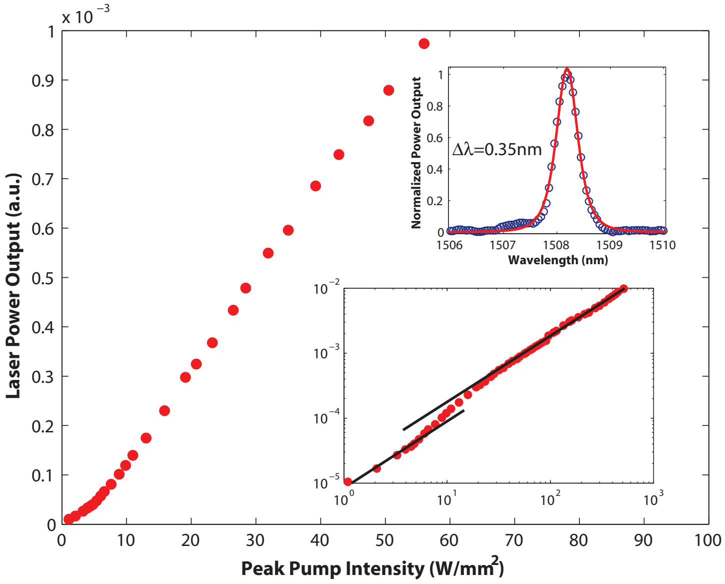

Figure 5.6: The light-light curve for a nanolaser with gain core radius of $R_{core} = 450\,\mathrm{nm}$ at 77 K. The same data set is shown in the bottom inset graph as a log-log plot. The upper inset is the lasing spectrum taken with monochromator; measured linewidth is 0.35 nm

ment factor [85]. The smooth ASE transition region and reduced threshold pump density of the S-curve at 77 K result from increased material gain, suppressed spectral broadening, enhanced cavity Q and much lower non-radiative recombination rates at cryogenic temperatures [84, 86].

For the 250 nm sample the lasing wavelength at 77 K is 1,527 nm and the threshold is about 12 W/mm^2, as shown in Figure 5.7. The emission spectrum of this sample, measured after the light-light curve, was severely affected by material degradation and is not shown. The slope of the PL-related linear part of the log-log curve (inset of Figure 5.7) is around 1.2, in contrast to the samples with $R_{core} \approx 450\,\mathrm{nm}$ for which the slope is close to unity. The PL region slope larger than unity indicates that a significant fraction of recombination events is caused by single-particle non-radiative processes, such as surface recombination [87]. In the smaller nanolasers, surface recombination is likely to be responsible for the high PL slope, since the ratio of the gain core surface area to its volume for the sample with $R_{core} \approx 250\,\mathrm{nm}$ is much greater than the surface/volume ratio for

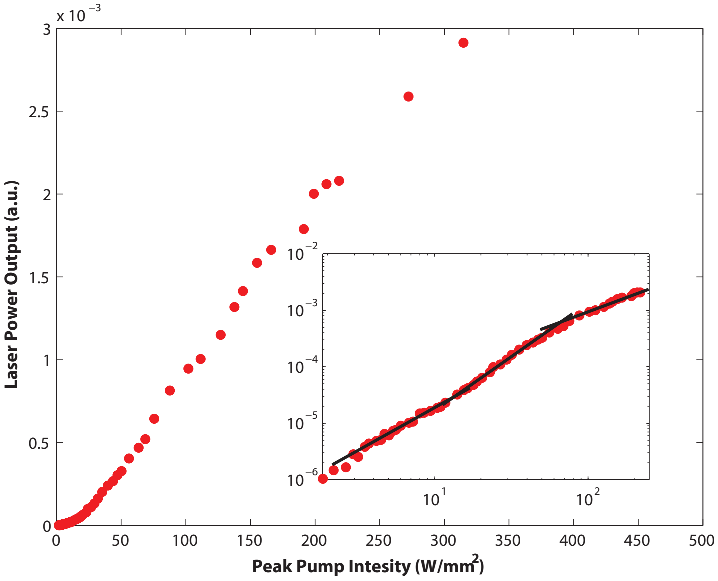

Figure 5.7: The light-light curve for a nanolaser with gain core radius of $R_{core} \approx 250\,\text{nm}$ at 77 K with the corresponding log-log plot in the inset graph.

the sample with $R_{core} \approx 450\,\text{nm}$ and thereby, must introduce many more non-radiative recombination centers. Along with the problem of dramatic drop in stimulated emission intensity under optical pumping at room temperature, this is an interesting issue to be further investigated.

5.5 Conclusion

In this paper we demonstrate a wafer bonded sub-wavelength scale laser that can be integrated onto a silicon platform. We observe room temperature lasing from near-sub-wavelength structures with gain core radius $R_{core} \approx 450\,\text{nm}$ and cryogenic temperature operation for sub-wavelength structures with $R_{core} \approx 250\,\text{nm}$. The results for the optically pumped lasers are expected to improve through further optimization of the fabrication process. We believe that our approach to realization of sub-wavelength scale coherent sources, combined with the latest III-V-to-Si wafer bonding solutions, is a promising path for the realization of highly integrated and miniaturized room temperature silicon photonic devices. In addition, our unique metal-dielectric resonator design is of interest for a number of applications, such as on-chip communication, optical interconnects, sensing and storage.

Chapter 5, in full, is a reprint of the material as it appears in “Wafer bonded sub-wavelength metallo-dielectric laser,” O. Bondarenko, A. Simic, Q. Gu, J. H. Lee, B. Slutsky, M. P. Nezhad, and Y. Fainman, *IEEE Photonics Journal*, vol. 3, no. 3, pp. 608–616, 2011. The dissertation author was the primary co-investigator and coauthor of this paper.

Chapter 6

Thresholdless nanoscale coaxial lasers

6.1 Introduction

Nanolasers are an emerging field of science, with a wide range of applications from on-chip optical communication to imaging, sensing, spectroscopy, and lithography. Lasing had long been demonstrated in large-scale cavities, however, as the size of cavity shrinks, the faster reduction of optical gain compared to cavity losses poses a serious challenge in achieving lasing. A paradigm shift came, rooted in the seminal work of Purcell [88] on the role of small cavities in altering photon emission characteristics of the gain medium, and therefore relaxing the conditions for lasing in small cavities [89]. This has since inspired the quest for the "ultimate nanolaser", a scalable, low threshold, efficient source of radiation that operates at room-temperature, and occupies a small area on chip [90].

There are currently two main approaches in designing nanolasers. The first approach utilizes dielectric based structures. Dielectrics have low loss at optical frequencies and can be designed as multi-layer stacks to provide strong optical feedback. Examples for such structures are vertical cavity surface emitting lasers (VCSELs) [91], micro/nano disks [20], and photonic band-gap lasers [23, 24, 92]. There are, however, several drawbacks in using dielectric-based nanolasers.

They are either large in size or their mode extends far out of the gain region, and thus they exhibit poor gain-mode overlap. Furthermore, light confinement with dielectrics, either by total internal reflection or stop-band reflection, entails inherent scalability limitation. The second approach in designing nanolasers uses metals in the cavities. In recent years, nanoscale metallic [25], plasmonic [56,93,94] and metallo-dielectric [51, 77] cavities have shown to confine light in ultra-small volumes and to improve the gain-mode spatial overlap. Moreover, metal cavities offer better thermal management in comparison to dielectric cavities and are more suitable for electrical pumping. However, metal-based nanolasers require high threshold pump power because of the significant absorption loss of the metals at optical frequencies. The high threshold of metal based lasers can be reduced by designing a cavity that enhances the coupling of spontaneous emission into the lasing mode. Ultimately, the threshold constraint can be completely eliminated by reaching the so-called thresholdless lasing, which occurs when every photon emitted by the gain medium is funneled into the lasing mode [89].

6.2 Design, simulation and fabrication

Here we report the first demonstration of lasing in metal based nanoscale coaxial cavities. Inspired by the coaxial resonators used in the microwave domain [95], we present the smallest nanolaser to date that operates in the *continuous wave* regime at *room-temperature*. Furthermore, we designed a nanoscale coaxial cavity that fulfills the conditions for thresholdless lasing which we observe at cryogenic temperatures. This first demonstration of thresholdless lasing from a broadband gain medium in a cavity of sub-wavelength size in all three-dimensions emphasizes the significance of the nanoscale coaxial structures for future applications.

The coaxial laser cavity is portrayed in Figure 6.1a. At the heart of the cavity lies a coaxial waveguide that is composed of a metallic rod enclosed by a metal coated semiconductor ring [96, 97]. To form a cavity, the coaxial waveguide is capped at both ends with thin low index dielectric plugs. The upper plug is made of silicon dioxide and is covered by silver. The lower plug, which channels

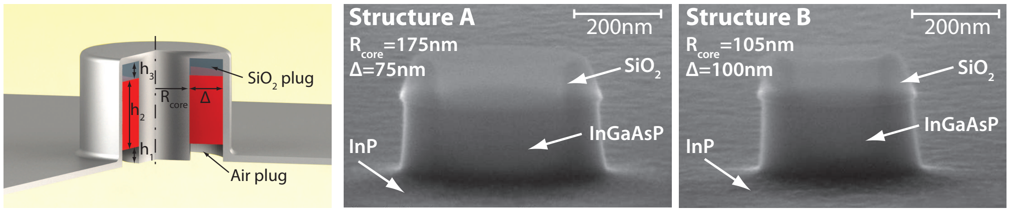

(a) **(b)** **(c)**

Figure 6.1: **(a)** Schematic of a coaxial laser cavity. **(b)** and **(c)** SEM micrographs of the constituent rings in *Structure A* and *Structure B*, respectively. The side view of the rings comprising the coaxial structures are seen. The rings consist of SiO_2 on top and quantum wells gain region underneath.

light out of the laser cavity and allows the penetration of the pump beam in, is filled with air. The metal in the coaxial cavity is placed in direct contact with the semiconductor to ensure a large overlap between the mode and the emitters of the gain medium. In addition, the metallic coating serves as a heat sink.

To reduce the lasing threshold, the coaxial structures are carefully designed to maximize the benefits from the modification of the spontaneous emission due to Purcell effect. Because of their small sizes, the modal content of the nanoscale coaxial cavities has intrinsic sparsity which is a key requirement to obtain high spontaneous emission coupling into the lasing mode. Their modal content can be further modified by tailoring the geometry, i.e. the radius of the core, the width of the ring, and the height of the low index plugs, bearing in mind that the number of modes that may participate in the lasing process is ultimately limited to those that are within the gain bandwidth of the semiconductor active material. The semiconductor gain medium used in this work is composed of six quantum wells of $\mathrm{In_{x=0.734}Ga_{1\text{-}x}As_{y=0.57}P_{1\text{-}y}}$ (10 nm thick) / $\mathrm{In_{x=0.56}Ga_{1\text{-}x}As_{y=0.938}P_{1\text{-}y}}$ (20 nm thick), resulting in a gain bandwidth that spans from 1.26 µm to 1.59 µm at room-temperature, and from 1.27 µm to 1.53 µm at 4.5 K [98].

We consider below two different geometries based on the schematic of Figure 6.1a. The first, which we refer to as *Structure A*, has an inner core radius of $R_{core} = 175$ nm, gain medium ring of $\Delta = 75$ nm, lower plug height of $h_1 = 20$ nm, gain medium height of $h_2 = 210$ nm, and upper plug height of $h_3 = 30$ nm. *Structure B* is smaller in diameter having $R_{core} = 100$ nm, and $\Delta = 100$ nm. The heights of the plugs and gain medium are identical to those of *Structure A*. The two structures are fabricated using standard nanofabrication techniques. Figure 6.1b and c show the SEM micrographs of the constituent rings in *Structure A* and *Structure B*, respectively. For the details of the fabrication procedure see subsection 6.5.1.

In Figure 6.2 we present the modal content of the two structures at a temperature of 4.5 K, modeled using the Finite Element Method (FEM).[1] Figure 6.2a shows that for *Structure A* the fundamental TEM-like mode and the two degenerate HE_{11} modes are within the gain bandwidth of the active material. This simulation was also repeated for *Structure A* with room-temperature parameters (not shown). The two degenerate HE_{11} modes are red shifted to 1,400 nm, and exhibit a reduced quality factor of $Q \approx 35$ compared to $Q \approx 47$ at 4.5 K. The TEM-like mode is red shifted to 1,520 nm with $Q \approx 53$ compared to $Q \approx 120$ at 4.5 K.[2]

Structure B, as shown in Figure 6.2b, supports only the fundamental TEM-like mode at a temperature of 4.5 K. The quality factor of this mode at $Q \approx 265$, is higher than that of *Structure A*. In general, the metal coating and the small aperture of the nanoscale coaxial cavity inhibit the gain emitters from coupling into the continuum of the free-space radiation modes [100, 101]. Hence, the single mode cavity of *Structure B* exhibits very high spontaneous emission coupling factor ($\beta \rightarrow 1$), thereby operating very close to the ideal thresholdless laser [102]. This is in contrast to *Structure A* in which the spontaneous emission is distributed between three modes of the cavity.

It should be noted that the central wavelength of the modes is very sensitive to the size of the cavity. Variations as small as a few nanometers in diameter may cause a shift of tens of nanometers in the spectral location of the modes. This means that our existing fabrication and characterization tools do not allow to predict the exact location of the modes in the output spectrum of the fabricated structures before performing the optical measurements.

---

[1] For analytical modeling of coaxial nanostructures see Appendix C

[2] In the FEM simulation of devices operating at 4.5 K, we used $\epsilon_{silver} = -120.43 - 0.03073i$ [25, 47], $\epsilon_{gain} = 11.15$ [77, 99], $\epsilon_{InP} = 9.49$ [99], $\epsilon_{SiO_2} = 2.1$ and $\epsilon_{air} = 1$. For the devices operating at room-temperature, the permittivities that differ from those at 4.5 K are $\epsilon_{silver} = -120.43 - 3.073i$ [25], $\epsilon_{gain} = 11.56$ [77] and $\epsilon_{InP} = 9.86$ [99].

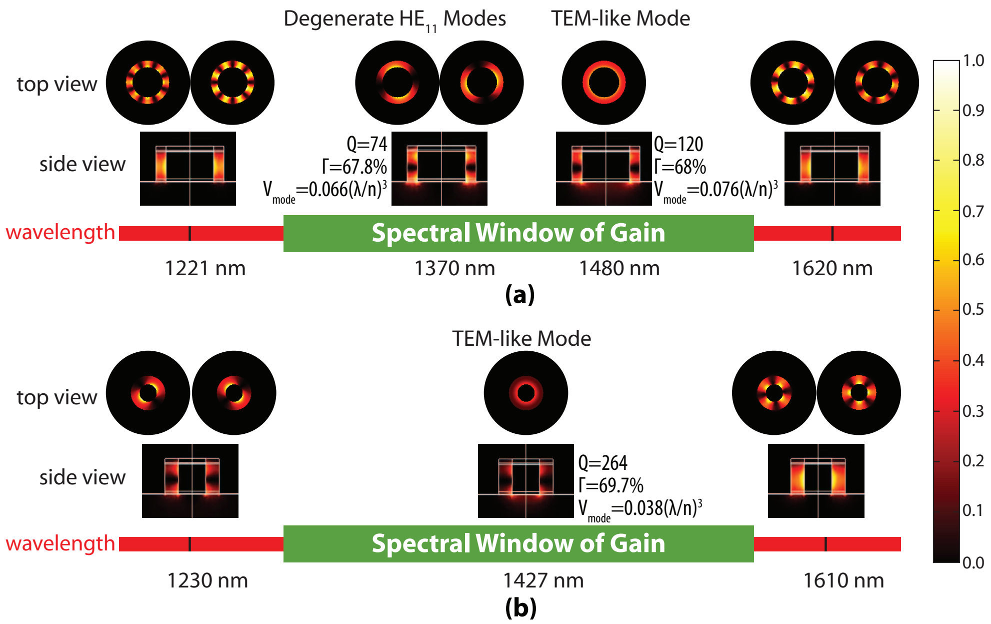

Figure 6.2: **(a)** The modal spectrum of the cavity of *Structure A* at a temperature of 4.5 K. This cavity supports a pair of HE_{11} degenerate modes and the fundamental TEM-like mode. **(b)** The modal spectrum of the cavity of *Structure B*. This cavity only supports the fundamental TEM-like mode in the gain bandwidth of the quantum wells. In the figures, Q is the quality factor of the mode, Γ is the mode-gain overlap, and V_{mode} is the modal volume.

6.3 Characterization and analysis

The characterization of the nanoscale coaxial lasers was performed under optical pumping with a 1,064 nm laser beam. For details of the measurement system see subsection 6.5.2. We used continuous wave pumping up to an incident power of about 25 µW on the aperture of the cavities. Figure 6.3 shows the emission characteristics of the nanoscale coaxial laser of *Structure A* operating at 4.5 K (light-light curve in frame (a), and spectrum evolution in frame (b)) and at room-temperature (light-light curve in frame (c) and spectrum evolution in frame (d)). The light-light curves of Figures 6.3a and 6.3c show standard lasing behavior where spontaneous emission dominates at lower pump powers (referred to as PL) and stimulated emission is dominant at higher pump powers (referred to as Lasing). The PL and Lasing regions are connected through a pronounced transient region called amplified spontaneous emission (ASE) [103]. In Figures 6.3b and 6.3d the maxima that are discerned at low pump powers reflect the modification of spontaneous emission spectrum by the cavity resonances depicted in Figure 6.2a. The linewidth of the lasers shown in the insets of Figures 6.3a and 6.3c narrows with the inverse of the output power at lower pump levels (the solid trend line). This is in agreement with the well-known Schawlow-Townes formula for the laser operating below threshold [104]. Around threshold, the rapid increase of the gain-index coupling in semiconductor lasers slows down the narrowing of the linewidth, until carrier pinning resumes the Schawlow-Townes inverse power narrowing rate [105,106]. The mechanisms affecting the linewidth above threshold, especially for lasers with high spontaneous emission coupling to the lasing mode, are still a subject of research and addressing them is beyond the scope of this paper [107,108].

A rate-equation model is adopted to study the dynamics of the photon-carriers interaction. For details of the rate-equation model see subsection 6.5.3. The light-light curves obtained from the rate equation model for the laser of *Structure A* are shown by solid blue lines in Figures 6.3a and 6.3c. For the laser operating at 4.5 K, by fitting the experimental data to the rate equation model, we found that almost 20 percent of the spontaneous emission is coupled to the lasing mode (mode with the highest quality factor). At room-temperature, the non-radiative recombination processes, surface and Auger, dominate, and as the carriers are lost through the non-radiative channels, the ASE kink is more pronounced, and the threshold shifts to the slightly higher pump powers.

Next, we measure the emission characteristics of *Structure B*. According to our electromagnetic analysis this structure operates as a thresholdless laser, as only one non-degenerate mode resides within the gain medium emission bandwidth. The emission characteristics of *Structure B* at a temperature of 4.5 K are shown in Figure 6.4. The light-light curve of Figure 6.4a that follows a straight line with no pronounced kink agrees with the thresholdless lasing hypothesis [104]. The thresholdless behavior further manifests itself in the spectrum evolution, seen in Figure 6.4b, where a single narrow Lorentzian emission is obtained over the entire five-orders-of-magnitude range of pump power. This range spans from the first

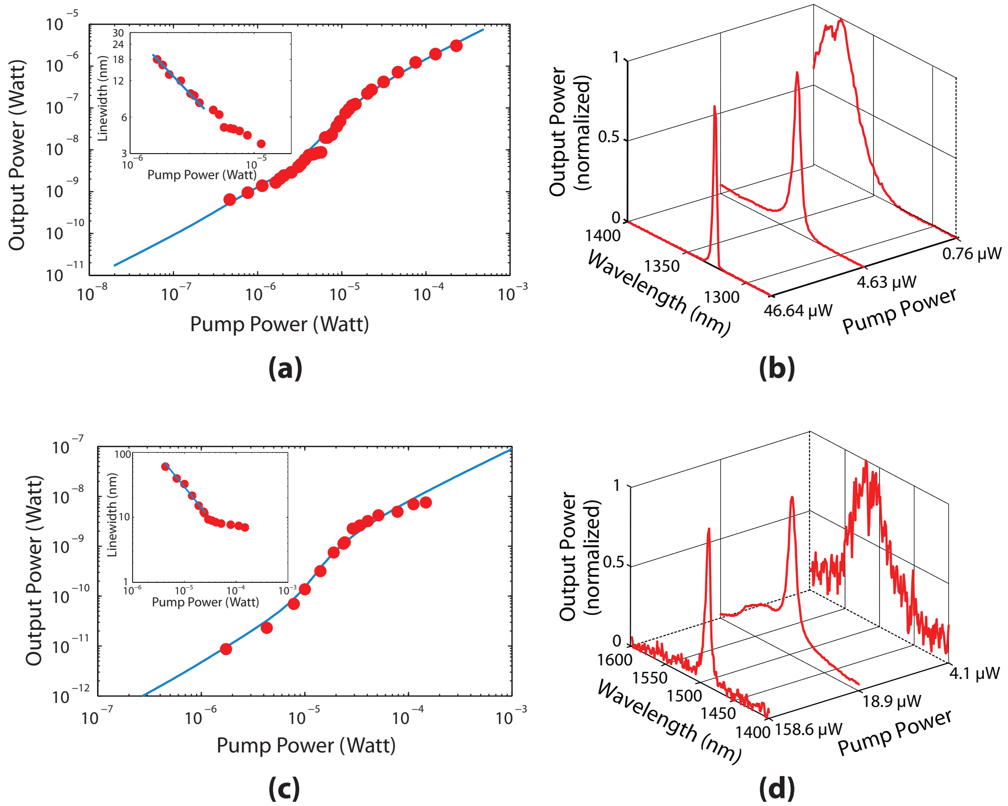

(a) **(b)** **(c)** **(d)**

Figure 6.3: Lasing in *Structure A*. **(a)** Light-light curve, **(b)** Spectrum evolution at a temperature of 4.5 K, **(c)** Light-light curve, and **(d)** Spectrum evolution at room-temperature. The pump power is calculated as the fraction of the power incident on the laser aperture. The solid curves in **(a)** and **(c)** are the best fit to the rate equation model. The insets show the linewidth vs. pump power. The resolution of the spectrometer was set to 3.3 nm.

signal detected above the measurement system noise floor at 720 pW pump power, to the highest pump power of more than 100 μW. Since the emission spectrum of the gain medium is broad, the observed spectrum is attributed to the cavity mode, with the linewidth at low pump powers of about 5 nm that agrees well with the calculated quality factor (Q) of the TEM-like mode. The linewidth depicted in the inset of Figure 6.4a is almost constant and does not narrow inversely with the output power as predicted by Schawlow-Townes formula at lower pump levels, meaning that the linewidth shows no subthreshold behavior [107, 108]. To the best of our knowledge, this linewidth behavior has never been reported in any other laser, and it may be the signature of thresholdless lasers. Finally, our rate equation model best fits to the experimental data if 95 percent of the spontaneous emission is coupled to the lasing mode ($\beta = 0.95$). At room-temperature *Structure B* supports more than one mode and it no longer fulfills the conditions for thresholdless lasing.

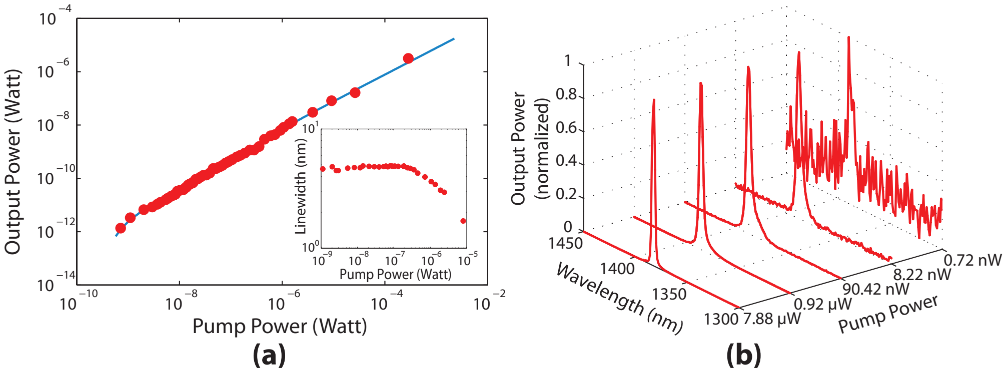

Figure 6.4: Thresholdless lasing in *Structure B*. **(a)** Light-light curve at a temperature of 4.5 K, **(b)** Spectrum evolution at a temperature of 4.5 K. The pump power is calculated as the fraction of the power incident on the laser aperture. The solid curve in **(a)** is the best fit to the rate equation model. The insets show the linewidth vs. pump power. The resolution of the spectrometer was set to 1.6 nm.

6.4 Conclusion

In summary, we have demonstrated both room-temperature, continuous wave lasing and low temperature thresholdless lasing in a genuinely broadband semiconductor gain setting with our nanoscale coaxial cavities. Owing to the fundamental TEM-like mode with no cut-off, these cavities show ultra-small mode confinement, offer large mode-emitter overlap that results in an optimum utilization of the pump power, and provide multifold scalability. Further developments towards electrical pumping of thresholdless nanoscale coaxial lasers that can operate at room-temperature is on the way. Finally, it should be emphasized that the implication of our work is twofold. Firstly, the demonstrated nanoscale coaxial lasers have a great potential for future nano-photonic circuits on a chip. Secondly, the single mode thresholdless coaxial lasers pave the way towards in-depth study of the relatively unexplored physics of atom-field interaction and carrier dynamics in ultra-small lasers.

6.5 Methods and additional materials

6.5.1 Fabrication

The nanoscale coaxial cavities are fabricated using standard nano-fabrication techniques. The gain consists of six quantum wells of $\mathrm{In}_{x=0.734}\mathrm{Ga}_{1\text{-}x}\mathrm{As}_{y=0.57}\mathrm{P}_{1\text{-}y}$ (20 nm) / $\mathrm{In}_{x=0.56}\mathrm{Ga}_{1\text{-}x}\mathrm{As}_{y=0.938}\mathrm{P}_{1\text{-}y}$ (10 nm) with overall height of 200 nm grown on p-type InP substrate (fabricated at OEpic Semiconductors Inc.). For protection, the quantum wells are covered by a 10 nm thick InP over-layer. Hydrogen silsesquioxane (HSQ) solution in methyl isobutyl ketone (MIBK) is used as a negative tone inorganic electron beam resist. The concentration ratio of HSQ (FOX12) and MIBK is adjusted such that an almost 50 nm thick resist is spun on the wafer. The resist is then soft baked and rings with different inner radii and widths are written by electron beam exposure. The electron beam converts the HSQ resist to an amorphous structure similar to SiO_2. The patterned wafer is then immersed in tetramethylammonium hydroxide (TMAH) for 180 seconds and rinsed in isopropyl alcohol (IPA) for 60 seconds. The exposed HSQ serves as a mask for the subsequent reactive ion etching process that utilizes H_2:CH_4:Ar plasma with gas proportions of 40:4:20 sccm respectively, and operates with RIE power of 150 W at chamber pressure of 30 mT and temperature of 40 °C (Trion). After dry etching, the samples are studied under scanning electron microscope (SEM). Then the wafer is cleaned with oxygen plasma to remove organic contaminations and the polymers that are built up during the dry etch process. We used standard oxygen cleaning procedure with 50 sccm flow of O_2, and RIE power of 150 W at the chamber pressure of 50 mT and temperature of 40 °C (Trion). In the next step, the alloy of silver and aluminum (98%Ag + 2%Al) is deposited using e-beam evaporation technique. The sample is then glued upside down to a piece of silicon wafer with silver epoxy and is dipped in hydrochloric acid for approximately 45 minutes to remove the InP substrate and to open up the air-plug aperture.

6.5.2 Measurements

The nanoscale coaxial structures were optically pumped with 1064 nm laser beam (SPI fiber laser) focused to an area of $\sim 64\,\mu m^2$ on the sample surface. A microscope objective with a numerical aperture of 0.45 is used to focus the pump beam as well as to collect the output light from the samples. Alignment of the pump beam to the desired cavity was performed by imaging the sample surface, through two cascaded 4–f imaging systems, onto the IR CCD camera (Indigo Alpha), using a broadband IR light source. Lasing was observed both at room temperature and at 4.5 K under continuous wave (CW) and pulsed mode pumping (12 ns pulse width at 300 kHz repetition rate) conditions. Output spectra were obtained using a monochromator (CVI Digikrom DK480) in conjunction with an electrically cooled InGaAs detector (EOsystems) and digital lock-in amplifier (Stanford Research Systems). Monochromator resolution was set to 3.3 nm by opening up the slits. Relatively large slit size was chosen to avoid power loss at the monochromator input slit. In some measurements, linewidths (FWHM) smaller than 3.3 nm were measured with monochromator resolution set to 1.65 nm and 0.67 nm.

For the L-L curves, at lower pump levels, the data is collected under continuous wave pumping, because the sensitivity of our detection system is too low to detect the signals generated by pulsed pumping. At very high power levels, the data was collected under pulsed mode pumping due to the limited available CW power from the pump laser. Continuous wave and pulsed mode measurements were performed with adequate overlap in the $3 - 25\,\mu W$ pump power region to ensure the two sets of data after scaling are consistent. The reported pump power is calculated by taking the ratio of the nanoscale coaxial aperture to the pump laser spot size ($64\,\mu m^2$) and multiplying it by the total pump laser power. The reporting output power is calculated by integrating the power per unit of wavelength (1 nm) over the spectral extent of the mode. Finally, cryogenic measurements were performed by placing the fabricated structures in a continuous-flow microscopy cryostat (Janis ST-500) that was cooled with liquid helium to the temperature of 4.5 K.

6.5.3 Rate equation model

Assuming photon number S_i in each mode at frequency ω_i and the total carrier number N, the rate equations are as follows:

$$\begin{aligned}
\frac{dS_i}{dt} &= \left(\Gamma_i \int g_{(n,\omega)} L_{\omega-\omega_i} d\omega - \frac{\omega_i}{Q_i}\right) S_i + \Gamma_i \int e_{(n,\omega)} L_{\omega-\omega_i} d\omega \\
\frac{dN}{dt} &= \alpha_{p(n,\omega_p)} P - \sum_i \left(\Gamma_i \int g_{(n,\omega)} L_{\omega-\omega_i} d\omega\right) S_i \\
&\quad - \sum_i \Gamma_i \int e_{(n,\omega)} L_{\omega-\omega_i} d\omega - \frac{N}{\tau_r} - \frac{N}{\tau_n r}
\end{aligned} \tag{6.1}$$

where P is the pump photon number at frequency ω_p, $L_{\omega-\omega_i}$ is the normalized Lorentzian function centered at the cavity mode frequency and with width determined by the cavity mode quality factor (Q), obtained in the FEM simulation. As noted in the main text, small variation in the inner an outer diameter of the gain rings as well as the length of the plugs causes the central frequency of the cavity modes to shift. We find the frequency of the modes from the modal spectrum evolution (Figures 6.3 and 6.4) and incorporate them in our rate equation model. The quality factors are less sensitive to cavity dimensions and are taken from simulations (Figure 6.2) with no adjustment. The modal overlap Γ_i between the mode and the quantum wells (of the volume V_g) is also obtained from the FEM simulation. The spectral dependence of gain and spontaneous emission on the carrier density $n = N/V_g$, as well as the pump absorption coefficient, are calculated via the quantum wells gain model [109], assuming uniform distribution of carriers among the wells. The spontaneous emission rate into the free space modes is calculated via the free space density of states:

$$\tau_r^{-1} = \frac{1}{F} \int \frac{n^3 \omega^2}{\pi^2 c^3} \hat{e}_{(n,\omega)} d\omega \tag{6.2}$$

where the modified spontaneous emission $\hat{e}$ takes into account the random polarization of the field [110]. The factor F is a free parameter that quantifies the inhibition of the spontaneous emission into the free space modes, and it is varied to fit the shape of the experimental data. The non-radiative recombination lifetime accounts for surface and Auger recombination: $\tau_{nr}^{-1} = A\frac{s_g}{V_g} + Cn^2$ where s_g is the gain medium surface area. At room temperature the non-radiative recombination is dominant and determines the shape of the light-light curve. The values of the surface and Auger recombination coefficient that provide best fit to the experimental data are $A = 4.4\,\mathrm{m/s}$, $C = 9.8 \times 10^{40}\,\mathrm{m^6/s}$ which are very close to the reported surface and Auger recombination coefficients for InGaAsP given in literature [111, 112]. At the temperature of 4.5 K, and correspondingly lower carrier densities, Auger recombination is negligible compared to other terms on the RHS of Equation 6.1, and the surface recombination coefficient value is one hundred times smaller than at room temperature. The light-light behavior at low temperature is primarily determined by mode competition.

Finally the β parameter is calculated as the ratio of the spontaneous emission into the lasing mode at frequency ω_0 to all spontaneous emission:

$$\beta = \frac{\Gamma_0 \int e_{(n,\omega)} L_{\omega-\omega_i} d\omega}{\sum_{i\neq 0} \Gamma_i \int e_{(n,\omega)} L_{\omega-\omega_i} d\omega + \tau_r^{-1}} \tag{6.3}$$

The value of β is slightly dependant on the carrier density and the values given in this report are calculated at the carrier density of $n = 2 \times 10^{17}\,\mathrm{cm}^{-3}$.

Chapter 6, in full, has been submitted for publication of the material as it may appear in “Thresholdless Nanoscale Coaxial Lasers,” M. Khajavikhan, A. Simic, M. Katz, J. H. Lee, B. Slutsky, A. Mizrahi, V. Lomakin and Y. Fainman, *Nature*. The dissertation author was the primary co-investigator and coauthor of this paper.

Chapter 7

Future directions and conclusion

7.1 Future directions

Although this dissertation addressed design, fabrication, and characterization of a number of particular sub-wavelength resonant structures, there is still a lot of work to be done. This is true for both the design / fabrication aspect as well as the characterization process. Here we list three possibilities for extending the efforts and improving the results that this dissertation presented thus far.

7.1.1 Direct current injection nanolasers

All of the nanolasers we discussed so far were optically excited with a 1,064 nm laser beam. As it is discussed in Appendix C this brings about a number of difficulties. For one, estimation of the power absorbed in the gain core is difficult. First, we need to know exactly what is the intensity in the part of the pump-laser spot that coincides with the nanolaser we are pumping. This is difficult because the beam profile of the pump laser is not uniform, and it has “hot” and “cold” spots, so we can only *estimate* the actual intensity. Second issue is how much of the power incident at the aperture of the nanolaser is actually absorbed in the core. We addressed this issue in Chapter 3 (see figure 3.7 and the pertaining discussion), but the main factors were the geometry of the aperture (cavity) and depth (or height) of the air plug. The analysis presented in Chapter 3 is particular for that geometry, and one needs to repeat this process for every new design. Optical pumping also makes the direct power measurement of the emitted laser radiation extremely difficult. The main problem is that the minuscule power output of the nanolaser (sub nW) is comparable to the still significant residual power of the pump laser after filtering. So instead of using a power meter to directly measure the emitted power, we acquire (via a monochromator) a spectrum of emitted radiation from the nanolaser (here pump doesn't play a role as it is spectrally far from the nanolaser output), and by integrating the spectrum we estimate the total power output of the nanolaser, based on prior calibrations of the system. The uncertainty arises due to the polarization dependance of monochromator, and this makes accurate absolute power measurements extremely difficult (for more details see Appendix C).

Lastly, optical pumping of nanolasers in anything other then the lab testing environment is impractical. Hence the ultimate goal is to create a direct current injection (electrically driven) nanolaser. Only in that way we can envision the nanolaser integration with the current and future photonic circuits.

Design and fabrication

Design of a successful electrically pumped nanolaser is much more challenging than the optical one. On top of the cavity design challenges we faced in the case of optically pumped nanolasers, we now need to make sure that the constituent materials are electrically conductive and the band diagram of the heterostructure is designed such that the electron-hole recombination can take place in the gain layer of the heterostructure. On top of that, there needs to be a path for the light to exit the cavity, meaning that the constituent materials need to be transparent at the wavelengths of interest (around 1,550 nm). Lastly, the metal used as a resonator shield and the metal alloy used for the electrical contacts are different, and that introduces additional fabrication complexity. Figure 7.1a shows the schematic representation of the nanolaser cavity design (heterostructure composition was based on that of reference [25]). The design is clearly similar to the original optically-pumped design outlined in Chapter 3, but with some important modifications.

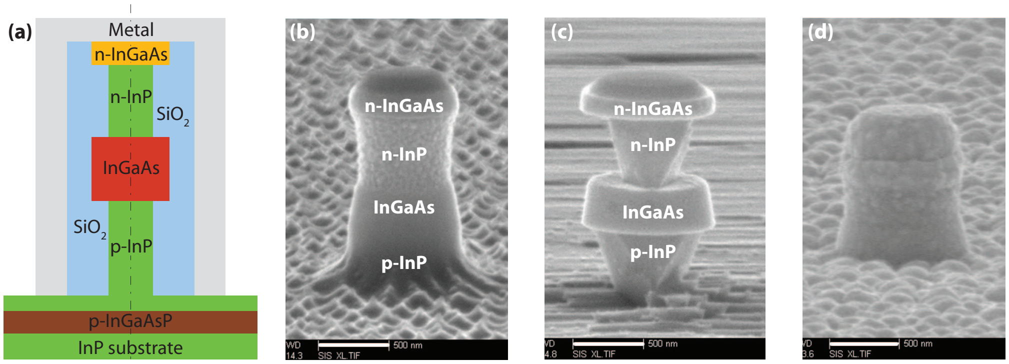

Figure 7.1: **(a)** Schematic representation of e-pumped nanolaser design. **(b)** SEM micrograph of an etched pillar. **(c)** SEM micrograph of a pillar after selective etching process. **(d)** SEM micrograph of a completed device prior to the fabrication of contacts.

First, the top and bottom plugs are now made of InP, unlike before when they were SiO_2 and air. Because the refractive index contrast is higher for InGaAs/SiO_2 than InGaAs/InP interface, to provide a cutoff and thus vertical mode confinement we needed to make the plug sections of the pillar narrower. This is achieved via a selective wet etching process, and the results can be seen in Figure 7.1c. Another difference is that the SiO_2 shield is now covering only sides of the structure, so that an electrical contact at the top of the pillar can be created. It should be immediately obvious that the fabrication is much more challenging then with the optically pumped design. After the shield metal deposition (Figure 7.1d), the final electrical contact pads and paths are made (not shown).

Characterization and discussion

Experimental characterization of the electrically pumped lasers is also more challenging (in some aspects at least) than that of the optically pumped devices. For details about the modifications to the experimental setup needed to accommodate the cryogenic characterization of electrically pumped nanolasers please see Appendix C. In the preliminary experiments we were able to confirm lasing from a slightly larger than wavelength device ($D_{core} \approx 2$µm) and those results are shown in Figure 7.2. Spectral evolution clearly shows the transition from a broad electroluminescence spectrum over the emerging lasing peak to a single narrow line ($\Delta\lambda = 0.26\,\text{nm}$ — Figure 7.2b inset) dominating the entire spectrum.

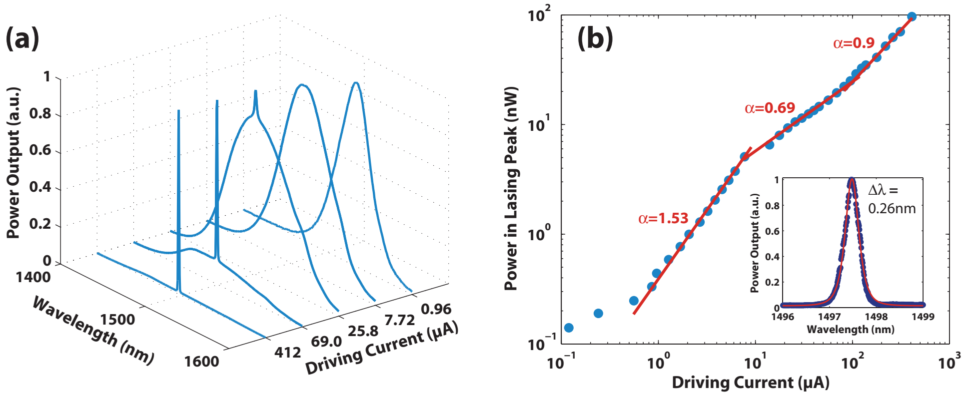

Figure 7.2: Lasing results from $D_{core} \approx 2\,\mu\text{m}$ electrically pumped laser. **(a)** Spectral evolution. **(b)** L-I curve shows an interesting behavior where the ASE (transition) region has a *lower* slope then the EL and lasing parts.

The L-I curve (Figure 7.2b) shows a peculiar behavior. In all of the previous lasing results reported in this dissertation we saw a logarithmic L-L curve to show distinct three regions. First, there is the below-threshold region where the slope is between 1 and 2 depending on the exact recombination mechanism taking place (see Chapter 5). This is followed by a transition region in which slope is higher then that of a previous region, and this is called amplified spontaneous emission region. Lastly we have the lasing region where slope flattens again to about 1. In all previously reported results the middle region had a *steeper* slope than the other two regions. Here we have the opposite case, where the middle region slope is only $\alpha = 0.69$. The explanation for this seemingly odd behavior lies in the fact that mode of the emission changes between the luminescence part and the lasing part. We can write the input-output power relation as $P_{out} = \eta P_{in}^{\alpha}$ which, after taking the logarithm of both sides, becomes $\log(P_{out}) = \log(\eta) + \alpha \log(P_{in})$, and that is what we plot in Figure 7.2b. So efficiency η dictates the vertical position of the particular line segment in Figure 7.2b, and if the efficiency changes from larger value in the luminescence region, to the smaller value in the lasing region, the only way to tie the two regions together is through a low slope central region.

But why would efficiency change with the change of the radiation mode? Since the laser emits into the substrate first and then into the air, a portion of the emitted power is lost due to total internal reflection. An additional portion of the emitted power goes uncollected due to the limited numerical aperture of the microscope objective used ($NA = 0.4$). This is summarized in Figure 7.3.

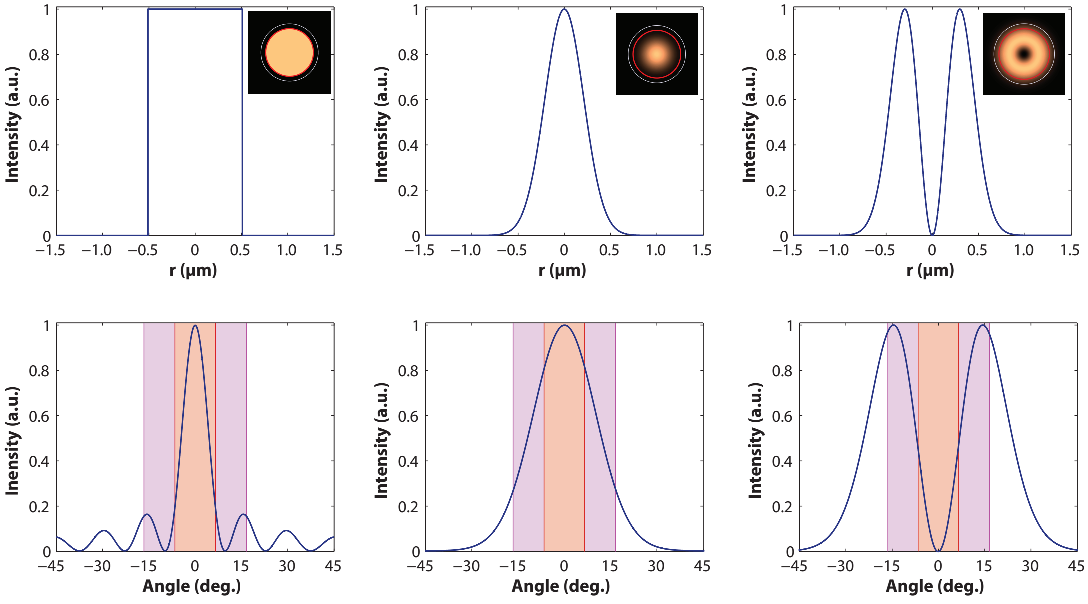

(a) (b) (c)

Figure 7.3: Depending on the assumed mode of radiation, a varying fraction of total emitted power is actually detected. The top row shows three assumed beam profiles **(a)** uniform, **(b)** gaussian and **(c)** Laguerre-gaussian (doughnut) mode. Insets show the same profiles in 2D with red line representing the bottom plug and white line representing SiO_2 shield. Bottom row shows the angular profile as the beam exits to free-space. Purple region represents the portion of light actually radiated out, and the red region represents the portion of the light actually detected due to limited numerical aperture of the microscope objective ($NA = 0.4$).

The top row of Figure 7.3 shows three different probable radial mode profiles. We imagine that the radiation in the luminescence region is uniformly distributed over the gain core, which we modeled by a flat-top distribution (Figure 7.3a) and gaussian distribution (Figure 7.3b). The lasing mode on the other hand is a whispering gallery mode, which we represented as a Laguerre-Gaussian distribution to a first approximation. The insets in the top row of Figure 7.3 show a 2D mode pattern, and red and white circles represent the gain and SiO_2 shield areas respectively. In the bottom row we show the angular distribution of the emitted light for all three cases mentioned above. The purple-shaded region represents the portion of the power that is transmitted out of the substrate while the red-shaded region represents the fraction of the power that is actually detected. It becomes clear upon comparing the bottom row figures, that we actually detect a much lower fraction of the lasing mode (4%) than that of the luminescence mode (32% for Gaussian and 38% for uniform), which explains the seemingly peculiar slopes of the S-shaped curve of Figure 7.2. It is important to note here that as we reduce the core diameter of the electrically pumped laser, we are bound to have even bigger problems with this changing efficiency, since the angular spread of the emitted light grows as the aperture shrinks. We also made some preliminary measurements of the sub-wavelength scale electrically pumped lasers, but those did not show conclusive evidence for lasing. We noticed linewidth narrowing, but not past $\sim 10\,\text{nm}$, and it needs to be further investigated why that is the case.

7.1.2 Measuring coherence

We presented in this thesis several different nanolaser designs and corresponding characterization results. One thing that was immediately apparent from these characterization results was that the behavior of nano-scale lasers can be different from that of conventional lasers. Because of relatively low Q values, linewidths are usually over a nanometer (sometimes several nanometers — Figure 6.3c inset). Light-light curves often don't have pronounced kink that separates spontaneous and stimulated emission part of the laser output (for example, Figure 4.7b). Even when light-light curves are presented in a logarithmic plot, they don't resemble a textbook example of a laser, with a spontaneous emission section with a slope of 1, a transition region with much steeper slope, ending with the lasing region whose slope is also 1. Figure 5.5 (inset) is an example of a laser that adheres well to the above prescribed recipe, while in Figure 5.7 (inset) these regions are harder to spot. It is also difficult to exactly model the lasing structure because many parameters are simply estimates (gain dielectric constant for example, exact geometry, etc.), so agreement between the model and the experiment is never perfect. All of these problems affect smaller lasers to a much greater degree than larger ones, which creates an additional problem in trying to push the design as small as we can.

The only way to prove, beyond any doubt, that the emission is actually stimulated rather than spontaneous is to measure the second (and/or higher) order coherence function $g^{(2)}(\tau)$. This is the holly grail of proofs of lasing, but it can be very challenging to measure (for detailed discussion please see Appendix F). Two main problems that we are facing are a broad linewidth that corresponds to $\sim$ps coherence time, and an emission wavelength at $\sim$ 1,550 nm. The short coherence time makes the traditional HBT experiment [113] almost impossible, because we need to be able to resolve the events at timescales less than the coherence time. Current state of the art coincidence-counting equipment simply is not capable of doing that. Another experimental approach is to measure coherence with a streak camera [114], but there the problem with the emission wavelength comes up. Streak cameras that have resolution of 2 ps are highly inefficient at c-band wavelengths (equipment is mostly Si-based), and that makes the experiment more challenging.

7.1.3 Comparing optical losses of different metals

Metals, like most compounds, behave differently at various regions of the electromagnetic spectrum. While close to a perfect conductor at RF, they are become much lossier at higher frequencies. At optical frequencies, metals are still very reflective, but they have nonnegligible loss (imaginary part of permittivity ϵ) which gives rise to plasmonic behavior. There are a number of experimental methods [52, 115] used to determine the real (ϵ') and imaginary (ϵ'') parts of dielectric constant ($\epsilon = \epsilon' + i\epsilon''$).[1] Also, there are a number of reported values of the permittivity of noble metals, in particular [47, 52, 116–119], and for the most part they differ from author to author. One major issue is the preparation of the

---

[1] Sometimes instead of permittivity, the real and imaginary value of the refractive index are reported $n = n' + ik$

sample, as surface roughness and presence of impurities can have a large effect on the measurements.

Since the quality of the sample is so important, it would be best if we could measure the permittivity directly for the metals we use in sample fabrication. Our demonstrated ability to use wafer-bonding to fabricate nanolasers on silicone wafers enabled us also to use different metals for the shield (see Chapter 5). If we now create a several large disks on the same wafer, and sputter different metals on parts of this wafer, we can directly compare the performance of the devices whose only difference is the metal used as the shield. Large disk are necessary so that the effects of fabrication non-repeatability (addressed in Chapter 4) are minimized. We prepared such a sample with three large disks ($D_{core} = 10\,\mu\mathrm{m}$) covered with gold, silver and aluminum respectively. We then optically pumped them below the lasing threshold, and observed the photoluminescence. The resulting L-L figures are shown in Figure 7.4.

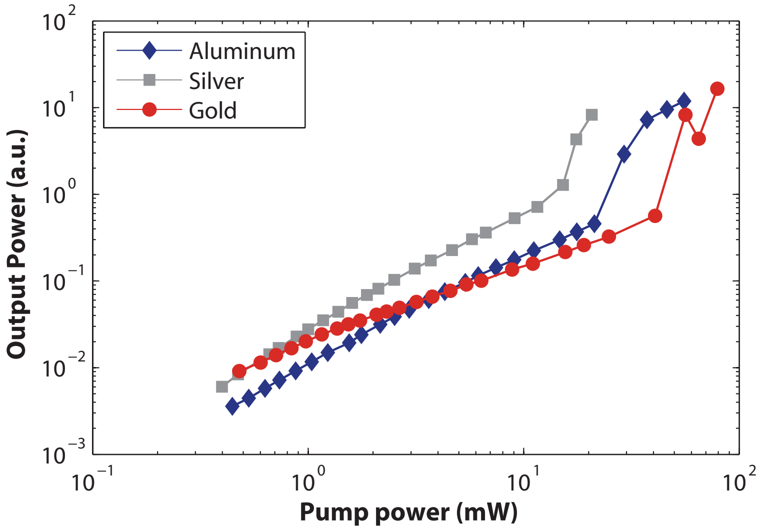

Figure 7.4: Comparison of the below-threshold performance of $D_{core} = 10\,\mu\mathrm{m}$ disk lasers covered with silver (gray squares), gold (red circles) and aluminum (blue diamonds). Silver shows 2.3 times better efficiency then aluminum.

We focus on photoluminescence only because, unlike lasing, it does not exhibit a well defined spatial mode, but it is uniformly distributed over the entire disk. This way we eliminate uncertainty stemming from lasing occurring at different modes for different samples. Furthermore, this spatial uniformity ensures large interaction between the metal shield and the optical field allowing us to extrapolate the losses in metal. If we go back to the empirical equation for luminescence power output $P_{out} = \eta P_{in}^{\alpha}$, or its logarithmic form $\log(P_{out}) = \log(\eta) + \alpha \log(P_{in})$ we can see that the efficiency η is responsible for the vertical placement of the particular L-L line of Figure 7.4. In turn, this efficiency in absolute terms depends on radiative loss, metal loss, detector efficiency, etc. but in relative terms, only the metal loss is different from sample to sample. It can be seen then from Figure 7.4 that silver has the best efficiency (the lowest loss). Additionally, when we quantitatively compare the η for silver and aluminum, we observe that silver has 2.3 times lower loss than aluminum, which is in agreement with published values [47, 52]. So far we are able to *compare* the loss parameters of metals one to another, but not to *measure* them directly. This could be achieved by doing numerical simulations in conjunction with this type of experiment, and this could offer a real insight into the optical properties of the *actual* metals we use in fabrication of nanolasers.

7.2 Conclusions

In this dissertation we examined both passive and active sub-wavelength resonant structures. We investigated the application of passive structures in creating a new class of materials (meta-materials) that have electromagnetic properties otherwise unattainable in nature. We developed a technique for characterization of negative index meta-materials by free-space measurement of the phase change in the meta-material. This technique gives an unambiguous proof of negative index of refraction, that is not limited to RF part of the spectrum.

We also investigated active resonant structures, specifically lasers, and their miniaturization down to sub-wavelength scale. We presented the first truly sub-wavelength nanolaser operating at room temperature and we investigated cryogenic operation of this laser design. We also offered a new fabrication approach, compatible with current silicon photonics, that could enable the integration of nanolasers in various silicon photonic devices. Our unique metal-dielectric resonator design is of great interest for a number of applications, such as on-chip communication, optical interconnects, sensing and storage.

We designed a coaxial nanolaser that offers some new and unique features for nanolasers. For one it is the first sub-wavelength laser that operates at continuous wave at room temperature. More importantly, it exhibits single-mode, thresholdless lasing at cryogenic temperatures. This is the first such result obtained from a sub-wavelength scale laser. Because of the single mode thresholdless behavior, these coaxial nanolasers pave the way towards in-depth study of the relatively unexplored physics of atom-field interaction and carrier dynamics in ultra-small lasers.

Further research on these topics will undoubtedly lead to electrically driven nanolasers, capable of operating at room temperature and ready for integration in future photonic devices.

Appendix A

Meta-material inspired sub-wavelength antenna

A.1 Introduction

In the years following their introduction [4, 5], meta-materials became an active field of study. Presently there are over 6,000 journal papers published on the topic, and the ability to tailor the electric (ϵ) and magnetic (μ) properties of the material found a number of potential applications. One of the more promising applications is the use of meta-materials for efficiency enhancement in small antennas [120–125]. The main idea is to encase a small electrical dipole (Hertzian dipole) radiator in a carefully designed meta-material shell to considerably improves antenna performance. Hertzian dipoles are inherently very poor radiators because of the very low radiation resistance, which leads to large impedance mismatch between the antenna and free space. This problem can be alleviated with the use of meta-materials. However, an additional challenge of driving such a small dipole radiator remains, as the impedance mismatch with the connecting coaxial cable is also quite large.

A.2 Design and simulation of a magnetic dipole antenna

Our solution to these challenges was to shy away from the Hertzian dipole as the driving source, and go to a small loop (magnetic dipole) antenna instead. The design goals set for this project were to design an efficient sub-wavelength antenna (hopefully $\lambda/d > 10$) operating at $\sim 1\,\mathrm{GHz}$. Uniformity of the radiation pattern was also a concern.

The meta-material that we were going to use for our antenna was based on split ring resonators, and initially used dual split ring resonators. We experimented with different design geometries including multi-layer cylinders (4 and 8 layer) as shown in Figure A.1a and multi-layer spheres (fabricated sample is shown in Figure A.1b). Spheres proved to be more challenging because each of the layers needed to be adequately designed to match the resonant frequency of other layers, while reducing the overall diameter of the layer to conform to the spherical shape (note that the oval appearance in Figure A.1b is due to Rexolite end caps placed on the antenna for structural stability). Design and simulation of the antenna was performed using Ansoft HFSS v.10 Maxwell equations solver (finite element method PDE solver). Figure A.1c shows the numerical simulation results for the radiated powers of spherical antenna (blue circles), 4-layer cylindrical antenna (red circles) and 8-layer cylindrical antenna (black circles). As a comparison we plot the radiation power of bare driving loops used to drive these antennae, 10 mm loop for the spherical antenna (blue diamonds) and 13 mm loop for cylindrical ones (black diamonds). It is important to note here that our driving loops are very well matched to the antennae. This is demonstrated by a very small value of $|S_{11}|$ (reflection) coefficient which in our simulations is shown to be less than $-20\,\mathrm{dB}$, meaning that less than one percent of the incident power is reflected back to the source (for additional details on S-parameters please see Appendix B). Everything else is either absorbed or reradiated by our antenna.

Improvements in radiated power brought by encasing the loops in meta-material are apparent at $\sim 40\,\mathrm{dB}$. However, maximum radiated power at the res-

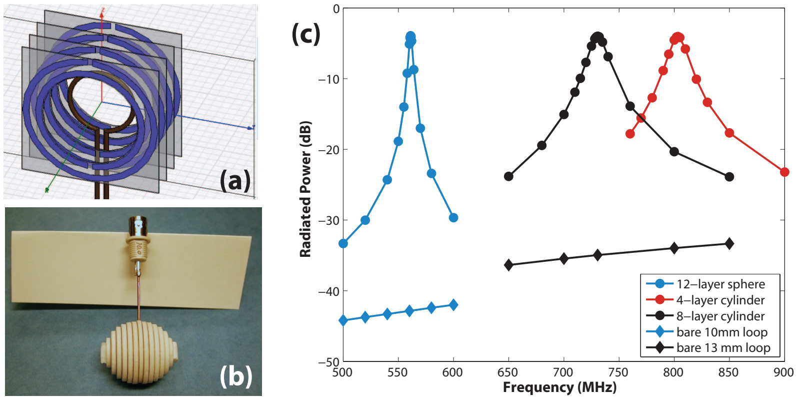

Figure A.1: Sub-wavelength antenna: **(a)** Design of 4-layer dual split-ring antenna with the driving loop in the middle; **(b)** Fabricated 12-layer spherical antenna; **(c)** Simulation results for radiated power of 12-layer spherical antenna, 4-layer cylindrical antenna and 8-layer cylindrical antenna compared to radiated power of bare driving loops.

onant frequency is still -4 dB, or $\sim 40\%$. Another important point is that the spherical antenna has a much narrower bandwidth which, depending on the application, can be undesirable. Radiated power however, paints only part of the picture of antenna performance, we need to look at the radiation pattern. Figure A.2a shows the simulated radiation pattern of a dual SRR 4-layer antenna (taken at the resonant frequency), and it is a typical magnetic dipole radiation pattern with null along the dipole (x). Orientation of the antenna is shown in the inset in the top left corner; important point is that the driving loop is placed in y-z plane, and that the gaps of the SRRs are aligned along the z axis. The radiation pattern that is shown is taken at $\theta = \pi/2$ i.e. along the z axis. We can see in Figure A.2c that the dual SRR configuration has azimuthal anisotropy of about 8 dB.

To improve this anisotropy we moved from the dual to the single SRR design, results of which are shown in Figure A.2b. The only difference in the two structures is the omission of the inner SRR, all other dimensions remained the same. As a result, azimuthal anisotropy improved from 8 dB to 0.64 dB. To explain this improvement we need to take a closer look at the radiation mechanism of the two antennae. Namely, the SRR can be viewed as a compound element consisting of a magnetic dipole (the metallic loop) and the electric dipole (across the small

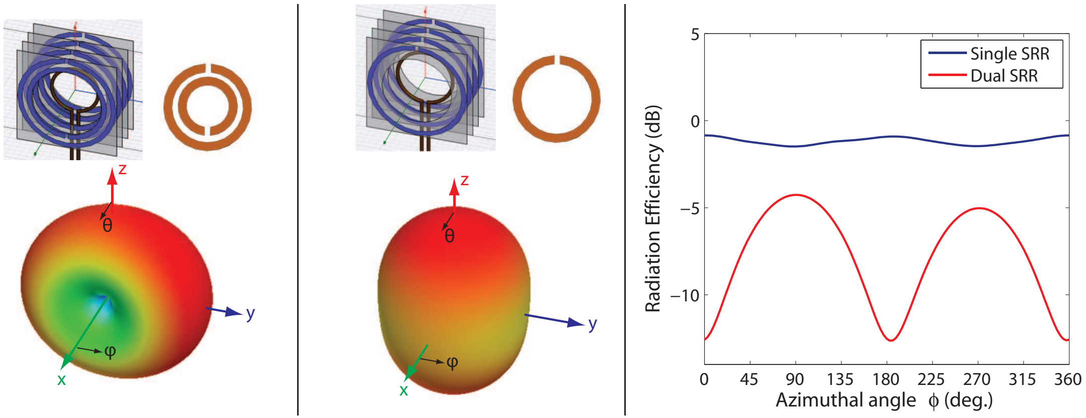

(a) **(b)** **(c)**

Figure A.2: Anisotropy of radiation pattern in azimuthal (ϕ) direction for **(a)** 4-layer *dual* split ring resonator antenna, and **(b)** 4-layer *single* split ring resonator antenna of same size. Note that the resonant frequency shifted from 800 MHz for a dual SRR antenna to 1.31 GHz. **(c)** Numerical simulation results showing improved azimuthal anisotropy.

gap), thus there are effectively *two* radiators contributing. In the case of the *dual* SRR design, magnetic dipoles for the two rings are aligned, but the two electric dipoles are exactly opposing one another, effectively canceling each other out.[1] This combination yields the effective radiation pattern we see in Figure A.2a — magnetic-dipole-like.

Conversely, in the case of the *single* SRR design, both magnetic dipole and the electric dipole constructively contribute to the total radiation of the antenna. The magnetic dipole has a radiation null along the x axis, while the electric dipole has a radiation null along the y axis. They both have radiation maxima along the z axis, which is precisely what leads to the much more uniform radiation pattern that can be observed in Figures A.2b and A.2c. Additionally, this also leads to improved radiation efficiency which is increased from 62% in the case of the dual SRR design to 87% for the single SRR design.

---

[1] One can also view this as a combination of a magnetic dipole and an electric quadrupole.

A.3 Fabrication and measurements

We fabricated the antenna samples using the rapid prototyping micro mill (LPKF ProtoMat C100/HF) from standard 14 oz copper on FR4 or Rexolite substrate. The individual SRR layers were then assembled using low-loss Rexolite rods and Rohacell spacers (see Figure A.1b). Measurements were performed in collaboration with our industry partners in an anechoic chamber equipped with cutting-edge antenna testing equipment. Figure A.3a shows a 2-layer single SRR antenna mounted in the center of an anechoic chamber encircled by polarization sensitive detectors (yellow crosses) arranged in a ring that loops over the antenna. The experimental results are presented in Figures A.3b and A.3c and are compared to the numerical simulations.

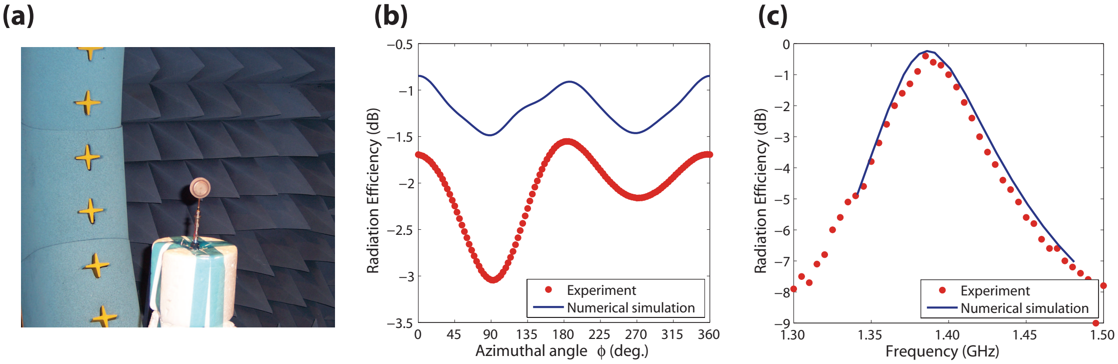

Figure A.3: **(a)** Testing the antenna in an anechoic chamber. Yellow crosses are polarization-sensitive detectors. **(b)** Azimuthal (ϕ) anisotropy of 4-layer single SRR antenna – simulated anisotropy is only 0.5 dB while the experimentally determined one is 1.5 dB. **(c)** Radiation efficiency of 4-layer single SRR antenna – over 90% efficiency was achieved. Note that the simulation data is shifted by 19 MHz to align the peaks.

Experimental results for the azimuthal anisotropy show 1.5 dB anisotropy compared to 0.5 dB shown in simulations. Additional anisotropy in the experimental results is probably due to fabrication imperfections. If the two SRRs are not aligned some additional anisotropy will ensue. Still, this is a great improvement over the dual SRR configuration which in *simulation* had 8 dB anisotropy (preliminary experiments showed $\sim$ 10 dB).

A.4 Conclusions and future directions

We have designed, fabricated and characterized a sub-wavelength ($\lambda/d \approx 8$) split-ring-resonator based antenna. The antenna is driven by a magnetic dipole radiator, and it has greater than 30 dB better radiation efficiency than the loop itself. Through careful engineering, we designed the antenna such that it does not require any balun transformers at the input but is directly matched to a 50 Ω (or 75 Ω) transmission line, with $|\mathrm{S}_{11}| < -20$ dB. Moreover, radiation efficiency ($P_{radiated}/P_{accepted}$) is over 90%. Besides the compact design, this antenna has a very uniform radiation pattern, but being resonant in nature, it has a finite bandwidth of ~ 60 MHz. Another feature of this design is that it does not require the presence of a ground plane (unlike many patch antennas) which makes it suitable for use in UAV and other applications where large metal surfaces are avoided to reduce a radar signature. We designed the antenna to operate at cell frequencies (~ 1 GHz) but there is nothing in the design to prevent scalability to other frequencies. In fact we simulated similar models operating at 25 GHz.

Future improvements to this design include making a thinner antenna with 2 instead of 4 layers. Namely, most of the losses we encounter happen in the dielectric substrate. By having many layers, we increase the losses. Our simulations show that the radiation patten is not adversely affected with the reduction of the number of layers. Further improvements we are currently working on include the tunability of the resonant frequency and multi-channel operation. Once developed these improvements will certainly broaden the possible applications and increase the appeal of this sub-wavelength antenna.

Appendix B

Permittivity (ϵ) and permeability (μ) retrieval from S-matrix parameters

B.1 Explanation of S–Matrix and S–parameters

A scattering matrix, often abbreviated as S-matrix, is a matrix that relates initial and the final state of a system that is undergoing the scattering process. The concept is widely used in physics (most notably in quantum mechanics and field theory), and electrical engineering (mainly in signal processing). For the purpose of this dissertation we will look into the electrical engineering aspect only. We use the S-matrix to relate the input and the output electric fields for a "black-box" device under test. This provides us with reflection and transmission coefficients which can be used to extract electromagnetic material properties of the material under test (namely permittivity ϵ and permeability μ).

Figure B.1 shows a schematic representation of a system with two inputs (x_1 and x_2) and two outputs (y_1 and y_2) for which we can write:

$$\begin{pmatrix} y_1 \\ y_2 \end{pmatrix} = \begin{pmatrix} S_{11} & S_{12} \\ S_{21} & S_{22} \end{pmatrix} \begin{pmatrix} x_1 \\ x_2 \end{pmatrix} \tag{B.1}$$

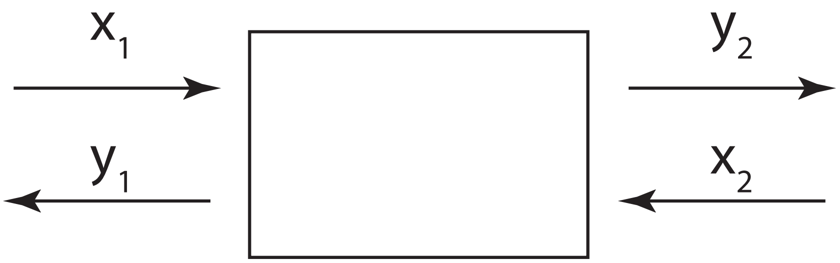

Figure B.1: Simple 2 × 2 network suitable for introduction and explanation of scattering matrix parameters (S-parameters)

This can be expanded to

$$y_1 = S_{11}x_1 + S_{12}x_2 \quad \text{and} \quad y_2 = S_{21}x_1 + S_{22}x_2 \tag{B.2}$$

If we think of four ports in Figure B.1 as counter propagating plane waves on either side of the device under test, it then becomes quite apparent that the elements of the scattering matrix represent reflection and transmission coefficients for the given system. It is also worth noting that if we are dealing with an ordinary linear system, the S-matrix is reciprocal, i.e. $S_{11} = S_{22}$ and $S_{12} = S_{21}$.

B.2 Retrieval of ϵ and μ from S-parameters

As mentioned above, S-parameters are a useful tool in analysis of simple electromagnetic systems. Moreover, sophisticated equipment such as Vector Network Analyzers (VNA) such as that used in the experiments described in Chapter 2, give us access to the full complex value of S-parameters (both magnitude and phase) and this information can then be used to fully characterize the material under the test, i.e. to determine its effective permittivity (ϵ_{eff}) and permeability (μ_{eff}) [126]. Often, a different set of parameters is used to describe the electromagnetic properties of a material, namely refractive index n and impedance Z. These parameters are interrelated by

$$\epsilon = \frac{n}{Z}, \qquad \mu = nZ, \qquad n = \sqrt{\mu\epsilon}, \qquad Z = \sqrt{\frac{\mu}{\epsilon}} \tag{B.3}$$

If we limit ourselves to normal incidence, the transfer matrix [127] for a one-dimensional slab of material of refractive index n, thickness d suspended in the air is given by

$$M = \begin{pmatrix} \cos(nkd) & \frac{1}{nk}\sin(nkd) \\ -nk\sin(nkd) & \cos(nkd) \end{pmatrix} \tag{B.4}$$

where k is a wave number for an incident wave (in vacuum) $k = \omega/c$. Following the treatment presented in [127] we can express transmission coefficient $t = S_{21}$ in terms of refractive index n and impedance Z as

$$\frac{1}{t} = \left[\cos(nkd) - \frac{i}{2}\left(Z + \frac{1}{Z}\right)\sin(nkd)\right] e^{ikd} \tag{B.5}$$

For clarity, it is useful here to define a normalized transmission coefficient as $t' = te^{ikd}$. In similar fashion we can then express the reflection coefficient $r = S_{11}$ in terms of n and Z as

$$\frac{r}{t'} = -\frac{i}{2}\left(Z - \frac{1}{Z}\right)\sin(nkd) \tag{B.6}$$

The above two equations can be inverted to

$$\cos(nkd) = \frac{1}{2t'}\left[1 - \left(r^2 - t'^2\right)\right] \tag{B.7}$$

and

$$Z = \pm\sqrt{\frac{(1+r)^2 - t'^2}{(1-r)^2 - t'^2}} \tag{B.8}$$

We can now express the index of refraction from the Equation B.7 by writing

$$\Re(n) = \pm\Re\left(\frac{\arccos\left(\frac{1}{2t'}\left[1 - (r^2 - t'^2)\right]\right)}{kd}\right) + \frac{2\pi m}{kd} \tag{B.9}$$

where m is an integer, and

$$\Im(n) = \pm\Im\left(\frac{\arccos\left(\frac{1}{2t'}\left[1 - (r^2 - t'^2)\right]\right)}{kd}\right) \tag{B.10}$$

It is very important to note that there is still some ambiguity left in these equations. These can be resolved by having some knowledge about the material in question. For instance, if we are dealing with the passive material (there is no gain), then we must have $\Re(Z) > 0$ and $\Im(n) > 0$. The first condition fixes the sign of the Equation B.8, and the second, in turn, fixes the sign of Equation B.10. Equation B.9 presents additional difficulty because of the correct choice of the branch for the arccos function (picking the value of integer m). As it can be seen, for large values of the thickness d, these branches become very close together, making it difficult to make a correct choice. For this reason the best results are obtained by using samples of small thickness. Even then it is necessary to measure at least two samples of different thicknesses, to make sure that the the choice of the branch gives consistent values of index n across the samples. This then yields unambiguous value and *sign* of the index of refraction n and impedance Z, from which, using the relations in Equation B.3 we can retrieve the full complex values of the permittivity ϵ and the permeability μ.

Appendix C

Optical setup for characterization of nanolasers

To characterize the nanolaser we had to build a custom high-performance imaging and spectroscopy optical setup (often called micro-PL setup) that is flexible, modular, and above all stable and sensitive. This required a lot of thought and compromises which are detailed in this appendix.

C.1 Setup design

To construct the micro-PL optical setup we had to consider several factors. Given the design of or devices we had to work in reflection mode, i.e. the same optics needs to be used for optical pumping and for the collection of the emitted light. We had to be able to illuminate and image the sample effectively so that we know which laser are we operating on. This meant large magnification. We also wanted the setup to be flexible enough so that we can expand and modify it without too much disruption. Lastly we needed to perform spectral measurements with high resolution (sub nm) with very little signal. These constraints led to a design depicted in the schematic show in Figure C.1.

The sample is first illuminated by 1.55 µm Super-luminescent Light Emitting diode (SLED) passed through a diffuser to reduce spatial coherence and provide uniform illumination (Figure C.2 a and b). It is then imaged via two cascaded

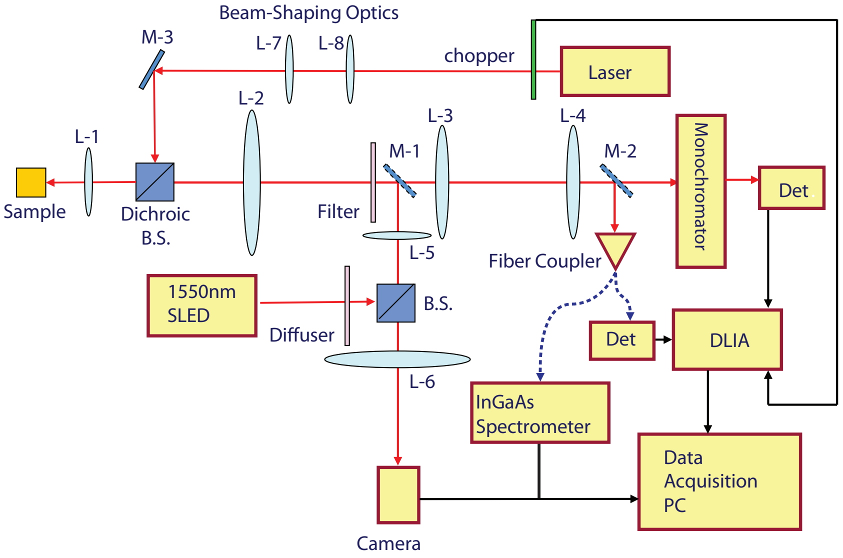

Figure C.1: Schematic of micro-PL characterization setup

4–f imaging systems (L1, L2, L5 and L6 in Figure C.1) to an InGaAs CCD camera (Indigo Alpha) with resolution of 252 × 316 pixels, and 30 µm pixel size. This enables us to locate the laser device of interest and position it in the center of the field of view for the pumping and characterization. We pump the nanolaser sample using a 1,064 nm pulsed fiber laser with 12 ns pulse width and 300 kHz repetition rate. We chose this combination of pulse width and repetition rate such that we have high enough peak power to create population inversion (short pulse). As for average power, it needs to be low enough such that thermal damage of the device under test is avoided, but sufficiently high to provide good signal to noise ration in detection.

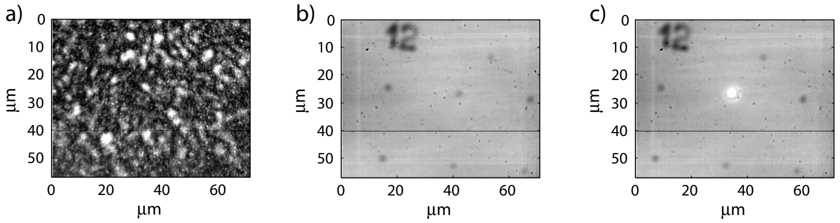

Figure C.2: Imaging of a nanolaser sample: without the use of the diffuser (a), with the diffuser (b), nanolaser emitting light (c)

The pump beam is delivered through the dichroic beam splitter into the microscope objective (Mitutoyo NIR ×20) and focused down on the sample to a spot size of $\approx 8 \times 8$µm. Since the pump is at 1,064 nm and the light emitted by the laser is at 1,500 nm this presents us with the problem of chromatic abberation. Namely, the focal plane is not in the same location for both wavelengths. To combat that, we introduce a telescope (lenses L7 and L8 in Figure C.1) with which we can adjust the divergence of the pump beam and thus make the focal planes for two wavelengths coincide. Now that the nanolaser is pumped and emitting (Figure C.2 c) we use a high-pass edge filter (Semrock RazorEdge) to remove the residual pump laser. At this point we have a few options on how to characterize the light output from the nanolaser, each with its advantages and disadvantages. We can do one of three things.

- By removing the mirror M1, and leaving mirror M2 in place, we re-image the laser through the 4–f imaging system comprised of lenses L3 and L4. We then couple the collected nanolaser light to the multi-mode optical fiber, and pass it to the InGaAs fixed-grating spectrometer, which gives us information about the spectrum of the light. The advantage of this spectrometer is that the measurement is fast, but that comes at the expense of SNR and, more importantly, the resolution of the spectrometer is limited to ~ 3 nm.

- Using the same mirror arrangement as above, we can couple the output of the nanolaser to a single-pixel thermoelectrically cooled InGaAs detector which gives us the total optical power emitted by the nanolaser, and is useful in generating light-light curves for a particular laser.

- Lastly, by removing both M1 and M2 mirrors, we can pass the the collected nanolaser light to the monochromator (CVI Digikröm DK480) which gives us excellent spectral resolution, down to 70 pm. The disadvantages of this approach is that monochromator by definition analyzes one wavelength at the time, thus making the measurement rather slow.

Because the light output of the nanolasers is on the order of few nanowatts, we employ the lock-in detection scheme to boost up the SNR. To achieve that we use the digital lock-in amplifier (Stanford Research System SR830) along with the mechanical chopper (Stanford Research System SR540) set at 1 kHz as a source of modulation we lock to. One could use the individual pulses from our pulsed laser for this purpose too. The problem is, however, that the detector we are using (EO Systems IGA-020-TE2-H) lacks the bandwidth necessary for that. Namely, because it is a very low noise detector, it has bandwidth of only 2 kHz, and our pulse train is at 300 kHz. So our detector sees this pulse train as a CW signal, and this is why the chopping is necessary. In this arrangement we are able to detect and spectrally characterize sub pW signals from the nanolaser.

C.2 Cryostat implementation

Our setup was primarily designed for room temperature characterization, but we built it in a such a way that it can be used for cryogenic measurements as well. This meant that optical components need to be positioned 21 cm above the table (Figure C.3), such that a cryostat on a 3-D translation stage would fit in the setup. This introduces some mechanical stability issues as components tend to vibrate more when mounted this high, so interferometric measurements would present a challenge in this setup. However, for imaging and spectroscopic purposes, this is not an issue at all. We use a continuous flow cryostat for microscopy applications (Janis ST–500) mounted on a custom fabricated vertical mounting plate, and attached to a 3–D translation stage. The cryostat can be used with either liquid nitrogen or liquid helium as a cryogen, and because of the integrated heating element inside the cryogenic chamber, we can fine-tune the temperature to a desired value via temperature controller (LakeShore 331).

C.2.1 Modifications for electrically pumped nanolasers

As it was noted elsewhere in this thesis, optical pumping was only a stepping stone to the ultimate goal, which was nanolasers with direct current injection (electrically pumped). In order to experimentally test these devices, some modi-

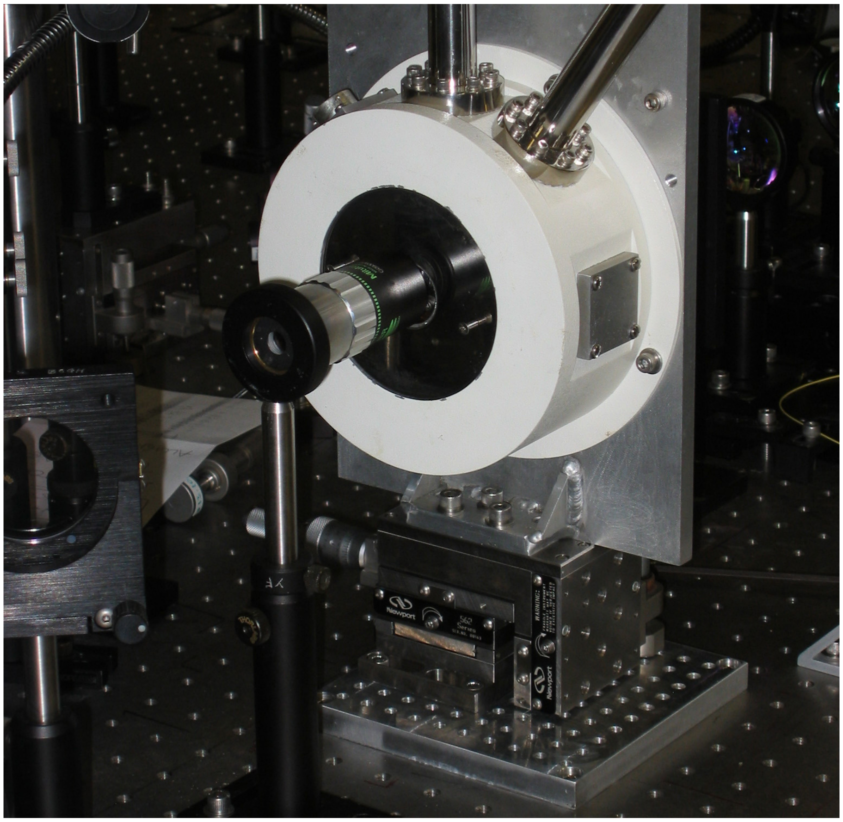

Figure C.3: Implementation of Janis ST–500 cryostat in the setup

fications to the setup were necessary. First and foremost, the cryostat had to be modified in two ways:

- New sample mount had to be designed and fabricated (machined)
- Cryostat chamber had to be modified with electrical feed-through connectors

Second, the mechanical chopper had to be moved between the edge-filter and mirror M-1. This is close to the imaging plane of the first 4–f imaging system (lenses L-1 and L-2), so the chopper does not interfere with the imaging. This allowed for accurate spectral measurements using the monochromator with lock-in amplifier in a low signal regime.

The first step in adaptation of the cryostat for the electrical pumping was design of the sample holder. This is challenging because on the wafer, metallic contacts are on the top side while laser emission is from the bottom. In order to

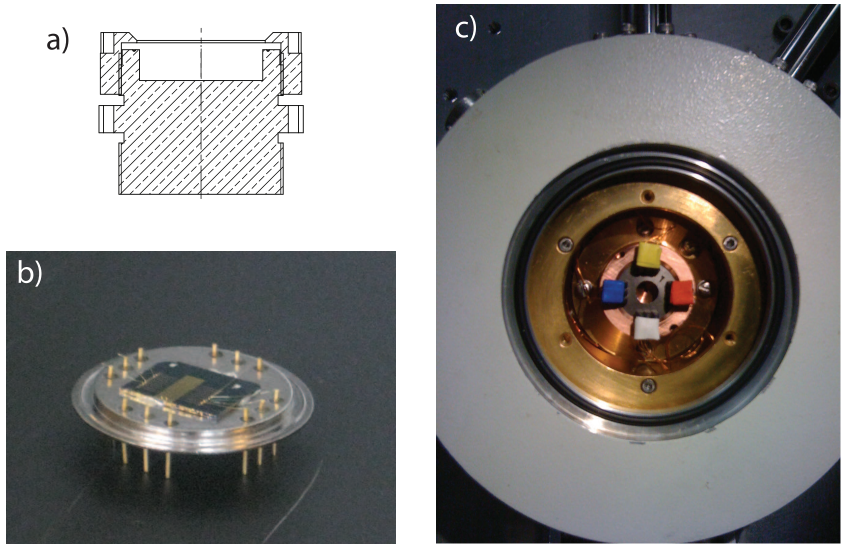

Figure C.4: Cryostat modification for electrical pumping: (a) cross section view of custom mount with a lid, (b) fabricated sample mounted on TO–8 chip-mount, (c) modified cryostat with everything in place (custom electrical connections, custom sample mount with test TO–8 package — no sample is present). The hole visible in the center of the mount is for allowing air to escape from the holder pocket during the vacuuming.

effectively cool the sample we need to provide thermal contact between the wafer and the sample holder, while leaving intact the metallic contacts and the wires used for driving the laser. We solved this problem by mounting the sample onto a TO–8 chip mount on which we drilled a 7 mm hole in the center (Figure C.4b). That way, the top of the wafer with all the contacts is accessible to be wire-bonded to the pins on the TO–8 mount, while laser emission is collected and analyzed through the hole on the mount.

As for the thermal contact, we designed a cryostat insert for that is comprised of two parts, holder and the screw-on lid which takes the TO–8 mount with the chip on it, and it holds it in place (Figure C.4a). The sample holder is directly screwed into the heat-exchanger in the cryostat. Thermal contact with the sample is achieved by clamping the edge of the TO–8 holder between the sample holder and its screw-on lid. Note that additional cryogenic thermal paste is added between the sample holder and the TO–8, and that we used epoxy impregnated with silver particles to mount the chip onto TO–8 mount for better thermal conduction.

When finally mounted in the cryostat, the legs of the TO–8 chip mount are facing outwards and we designed custom color-coded connectors to achieve the electrical contact between the sample and the outside of the cryostat. This, along with the 7 mm hole in the modified TO–8 mount can be seen in Figure C.4a (note that cryostat was opened and radiation shield windows removed for this photo).

C.3 Summary

We created a versatile, highly customizable, expandable modular micro-photo-luminescence (μPL) setup for use in room temperature as well as cryogenic conditions (both liquid He_2 and liquid N_2 can be used). The setup performs equally well in testing optically pumped lasers and direct current injection lasers. The modular nature of the setup allows for detailed characterization of the laser output including spectral analysis, near-field and far-field radiation patterns, polarization properties of the radiation pattern and possible future coherence measurements. This setup is primarily designed to work in the IR region of the spectrum (around 1.5 µm), but it is easily adaptable to operate in the visible region as well (again thanks to its modular nature). Due to use of the lock-in amplifier along with low-noise detectors, we are capable of spectrally analyzing signals as low as 50 fW.

One drawback is that absolute power measurements are impossible to perform. In the optical pumping, optical power meter cannot be used directly due to the pump laser leakage (despite the two stage filtering we have in place!). The next best thing is to integrate the spectrum as detected with a monochromator and lock-in amplifier. Here, pump leakage is not an issue due to the large spectral separation of the pump and the signal. However, because the monochromator relies on a grating for spectral decomposition of the input signal, there is an inherent problem in the design if the input light is polarized. Namely the grating efficiency is highly dependent on the polarization state of the input light, and the detected signal varies about 30% between the p-polarized and s-polarized signal, and since we generally don't know a priori the exact polarization state of the light, we have to live with this error when estimating the power output from the obtained spectra.

Appendix D

Analytical solution of electromagnetic modes in coaxial waveguide

D.1 Introduction

Despite the availability and popularity of different numerical methods for solutions of partial differential equations (namely Maxwell's equations), analytical solution, when possible, is a powerful tool to have. For one, numerical methods such as finite element method (FEM), finite difference time domain (FDTD), and finite difference frequency domain (FDFD) are all computationally rather expensive. This is in part due to the number of elements into which the geometry has to be divided (mesh size). These elements have to be smaller than the wavelength that we are solving for (at least $\lambda/3$) to have a good solution. The strength is that any arbitrary geometry can be solved, which is next to impossible to do analytically. However, in the simple cases where an analytical solution is attainable, it can yield much more complete results and it can be obtained much faster.

D.2 Solution of wave equation in cylindrical coordinates

One such example is that of a coaxial waveguide which we used as the basis for our coaxial nanolaser. Here, we can write the solution to the wave equation directly, and solve it using a rather straightforward numerical approach. In Figure D.1 we see a schematic representation of a coaxial waveguide. There are three distinct regions that we need to solve for. These are (I) metallic core, (II) dielectric (gain) center, and (III) metallic shell. Here we take that the outer edge of the shell region is at infinity. This is justified as long the thickness of the shell is more than a few skin-depths, which for a wavelength of $\lambda \approx 1{,}500\,\text{nm}$ means that the shell must be thicker than $\sim 200\,\text{nm}$.

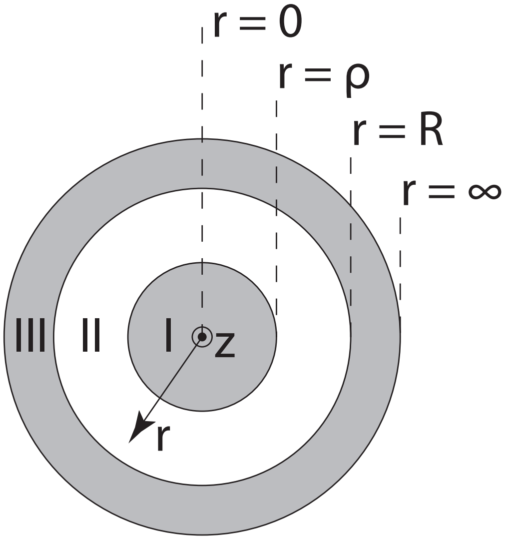

Figure D.1: Schematic representation of coaxial waveguide. There are 3 distinct regions: (I) metallic core, (II) dielectric (gain) center, and (III) metallic shell. Note that the outer boundary of the region III can be set to $r = \inf$ if the shell is more then a few skin-depths thick. For $\lambda \approx 1{,}500\,\text{nm}$ this means that shell needs to be more than $\sim 200\,\text{nm}$ thick.

We take propagation along the z axis, and then we can write the field components in the form of

$$\psi(r,\theta,z,t) = \psi(r,\theta)e^{i(\beta z - \omega t)} \tag{D.1}$$

where ψ can be any (r, θ, z) component of either $\mathbf{E}$ or $\mathbf{H}$ field, ω is angular frequency, and β is the propagation constant. Since in a waveguide one can express the transverse components of the fields in terms of z components [128], we only need to solve for E_z and H_z. Transverse fields are then given by

$$E_r = \frac{i\beta}{\omega^2\mu\epsilon - \beta^2}\left(\frac{\partial}{\partial r}E_z + \frac{\omega\mu}{\beta}\frac{1}{r}\frac{\partial}{\partial\theta}H_z\right) \tag{D.2}$$

$$E_\theta = \frac{i\beta}{\omega^2\mu\epsilon - \beta^2}\left(\frac{1}{r}\frac{\partial}{\partial\theta}E_z - \frac{\omega\mu}{\beta}\frac{\partial}{\partial r}H_z\right) \tag{D.3}$$

$$H_r = \frac{i\beta}{\omega^2\mu\epsilon - \beta^2}\left(\frac{\partial}{\partial r}H_z - \frac{\omega\epsilon}{\beta}\frac{1}{r}\frac{\partial}{\partial\theta}E_z\right) \tag{D.4}$$

$$H_\theta = \frac{i\beta}{\omega^2\mu\epsilon - \beta^2}\left(\frac{1}{r}\frac{\partial}{\partial\theta}H_z + \frac{\omega\epsilon}{\beta}\frac{\partial}{\partial r}E_z\right) \tag{D.5}$$

Now we can write the wave equation for the z component of the fields $E_z(r, \theta)$ and $H_z(r, \theta)$

$$\left[\nabla_t^2 + (\omega^2\mu\epsilon - \beta^2)\right]\psi = 0 \tag{D.6}$$

where ψ is the z component of either field, and ∇_t^2 is the tangential Laplacian operator given as $\nabla_t^2 = \nabla^2 - \partial^2/\partial z^2$. The general solution of the Equation D.6 has the form

$$E_z = (AJ_\nu(kr) + BY_\nu(kr))\cos(\nu\theta + \phi) \tag{D.7}$$

$$H_z = (CJ_\nu(kr) + DY_\nu(kr))\cos(\nu\theta + \zeta) \tag{D.8}$$

where A, B, C, D, ϕ and ζ are constants, ν is an integer (azimuthal mode number), and $k = \sqrt{\omega^2\mu\epsilon - \beta^2}$ is the wave number. J_ν and Y_ν are Bessel functions of first and second kind respectively. Here we need to note that although usually chosen, Bessel functions are only one of several possible choices for the eigenfunctions in the cylindrical coordinate system. One can also choose Hankel functions $H_\nu^{(1)}$ and $H_\nu^{(2)}$, as well as the modified Bessel functions I_ν and K_ν. The significance of the modified Bessel functions is that they are valid for complex values of arguments. The choice of the eigenfunctions to be used in our case then depends on the material in the region we are solving for, and care should be taken to properly select the eigen functions to avoid nonphysical solutions.

Looking at the Equation D.7 and applying continuity of E_z and H_z at a boundary between two materials at $r = r_0$, we get

$$\begin{aligned} &[A_1 J_\nu(k_1 r_0) + B_1 Y_\nu(k_1 r_0)] \cos(\nu\theta + \phi_1) \\ =&[A_2 J_\nu(k_2 r_0) + B_2 Y_\nu(k_2 r_0)] \cos(\nu\theta + \phi_2) \end{aligned} \tag{D.9}$$

and

$$\begin{aligned} &[C_1 J_\nu(k_1 r_0) + D_1 Y_\nu(k_1 r_0)] \cos(\nu\theta + \zeta_1) \\ =&[C_2 J_\nu(k_2 r_0) + D_2 Y_\nu(k_2 r_0)] \cos(\nu\theta + \zeta_2) \end{aligned} \tag{D.10}$$

Since the above two equations have to be satisfied for *all* values of θ, it follows that $\phi_1 = \phi_2 \equiv \phi$ and $\zeta_1 = \zeta_2 \equiv \zeta$. Continuity of the azimuthal component of the electric field E_θ (from the Equation D.3) then gives us

$$\begin{aligned} &\frac{1}{k_1^2}\Big(-\frac{\nu}{r_0}[A_1 J_\nu(k_1 r_0) + B_1 Y_\nu(k_1 r_0)] \sin(\nu\theta + \phi) \\ &-\frac{\omega\mu_1}{\beta} k_1 [C_1 J_\nu'(k_1 r_0) + D_1 Y_\nu'(k_1 r_0)] \cos(\nu\theta + \zeta)\Big) \\ =&\frac{1}{k_2^2}\Big(-\frac{\nu}{r_0}[A_2 J_\nu(k_2 r_0) + B_2 Y_\nu(k_2 r_0)] \sin(\nu\theta + \phi) \\ &-\frac{\omega\mu_2}{\beta} k_2 [C_2 J_\nu'(k_2 r_0) + D_2 Y_\nu'(k_2 r_0)] \cos(\nu\theta + \zeta)\Big) \end{aligned} \tag{D.11}$$

where prime quantities represent derivatives with respect to their own arguments. Observing the Equation D.11, and gathering terms with $\sin(\nu\theta + \phi)$ on one side, and $\cos(\nu\theta + \zeta)$ on the other side of the equation we can see that this equation has a solution only when

$$\sin(\nu\theta + \phi) = \pm\cos(\nu\theta + \zeta) \tag{D.12}$$

or in other words when $\phi = \zeta \pm \pi/2$. This uncovers the inherent degeneracy of solutions of the wave equation in cylindrical waveguide. The azimuthal component can be rotated by $\pi/2$ and the solution still remains valid. For this reason we can now rewrite the Equation D.7 as

$$E_z = (AJ_\nu(kr) + BY_\nu(kr))\sin(\nu\theta) \tag{D.13}$$

$$H_z = (CJ_\nu(kr) + DY_\nu(kr))\cos(\nu\theta) \tag{D.14}$$

or

$$E_z = (AJ_\nu(kr) + BY_\nu(kr))\cos(\nu\theta) \tag{D.15}$$

$$H_z = (CJ_\nu(kr) + DY_\nu(kr))\sin(\nu\theta) \tag{D.16}$$

We can now finally write the equations for the z components of both **E** and **H** fields in all 3 regions illustrated in Figure D.1

$$\left.\begin{aligned} E_z &= A_1 I_\nu(k_1 r)\cos(\nu\theta) \\ H_z &= C_1 I_\nu(k_1 r)\sin(\nu\theta) \end{aligned}\right\} \quad \text{region I} \tag{D.17}$$

$$\left.\begin{aligned} E_z &= [A_2 J_\nu(k_2 r) + B_2 Y_\nu(k_2 r)]\cos(\nu\theta) \\ H_z &= [C_2 J_\nu(k_2 r) + D_2 Y_\nu(k_2 r)]\sin(\nu\theta) \end{aligned}\right\} \quad \text{region II} \tag{D.18}$$

$$\left.\begin{aligned} E_z &= A_3 K_\nu(k_3 r)\cos(\nu\theta) \\ H_z &= C_3 K_\nu(k_3 r)\sin(\nu\theta) \end{aligned}\right\} \quad \text{region III} \tag{D.19}$$

where $k_i = \sqrt{\frac{\omega^2}{c^2}\epsilon_i\mu_i - \beta^2}$, and ϵ_i and μ_i are *relative* permittivity and permeability of the material in the given region. Also note that for the regions I and III we chose modified Bessel functions because of the negative values of ϵ_r for metal, which yields complex argument for the Bessel functions. Moreover, in region I we only choose a modified Bessel function of first kind as it is finite at the origin, and in the region III we choose a modified Bessel function of second kind as it vanishes at infinity.

D.3 Applying the boundary conditions

We are now finally ready to apply boundary conditions for our waveguide. We have two boundaries to deal with, $r = \rho$ and $r = R$, and four continuity conditions to satisfy, namely continuities of E_z, E_θ, H_z and H_θ. From continuity of E_z at the $r = \rho$ boundary we have

$$A_1 I_\nu(k_1\rho) - A_2 J_\nu(k_2\rho) - B_2 Y_\nu(k_2\rho) = 0 \tag{D.20}$$

Continuity of E_θ at $r = \rho$ boundary gives

$$\begin{aligned} A_1 \frac{\nu}{k_1^2 \rho} I_\nu(k_1\rho) + C_1 \frac{\omega\mu_1}{k_1\beta} I'_\nu(k_1\rho) - \frac{\nu}{k_2^2\rho}\left[A_2 J_\nu(k_2\rho) + B_2 Y_\nu(k_2\rho)\right] \\ - \frac{\omega\mu_2}{k_2\beta}\left[C_2 J'_\nu(k_2\rho) + D_2 Y'_\nu(k_2\rho)\right] = 0 \end{aligned} \tag{D.21}$$

Continuity of H_θ at $r = \rho$ gives

$$C_1 I_\nu(k_1\rho) - C_2 J_\nu(k_2\rho) - D_2 Y_\nu(k_2\rho) = 0 \tag{D.22}$$

Continuity of H_θ at $r = \rho$ is given by

$$\begin{aligned} A_1 \frac{\omega\epsilon_1}{k_1\beta} I'_\nu(k_1\rho) + C_1 \frac{\nu}{k_1^2\rho} I_\nu(k_1\rho) - \frac{\omega\epsilon_2}{k_2\beta}\left[A_2 J'_\nu(k_2\rho) + B_2 Y'_\nu(k_2\rho)\right] \\ - \frac{\nu}{k_2^2\rho}\left[C_2 J_\nu(k_2\rho) + D_2 Y_\nu(k_2\rho)\right] = 0 \end{aligned} \tag{D.23}$$

At the other boundary $(r = R)$ these equations look like

$$A_2 J_\nu(k_2R) + B_2 Y_\nu(k_2R) - A_3 K_\nu(k_3R) = 0 \tag{D.24}$$

$$\begin{aligned} \frac{\nu}{k_2^2 R}\left[A_2 J_\nu(k_2R) + B_2 Y_\nu(k_2R)\right] + \frac{\omega\mu_2}{k_2\beta}\left[C_2 J'_\nu(k_2R) + D_2 Y'_\nu(k_2R)\right] \\ - A_3 \frac{\nu}{k_3^2\rho} K_\nu(k_3R) - C_3 \frac{\omega\mu_3}{k_3\beta} K'_\nu(k_3R) = 0 \end{aligned} \tag{D.25}$$

$$C_2 J_\nu(k_3R) + D_2 Y_\nu(k_3R) - C_3 K_\nu(k_3R) = 0 \tag{D.26}$$

$$\begin{aligned} \frac{\omega\epsilon_2}{k_2\beta}\left[A_2 J'_\nu(k_2R) + B_2 Y'_\nu(k_2R)\right] + \frac{\nu}{k_2^2 R}\left[C_2 J_\nu(k_2R) + D_2 Y_\nu(k_2R)\right] \\ - A_3 \frac{\omega\epsilon_3}{k_3\beta} K'_\nu(k_3R) - C_3 \frac{\nu}{k_3^2 R} K_\nu(k_3R) = 0 \end{aligned} \tag{D.27}$$

This represents a homogeneous overdetermined system of linear equations which can be expressed in the matrix form as

$$\begin{pmatrix} A_1 \\ C_1 \\ A_2 \\ B_2 \\ C_2 \\ D_2 \\ A_3 \\ C_3 \end{pmatrix} = \mathbf{M} \begin{pmatrix} 0 \\ 0 \\ 0 \\ 0 \\ 0 \\ 0 \\ 0 \\ 0 \end{pmatrix} \tag{D.28}$$

and which has nontrivial solutions only if $\det(\mathbf{M}) = 0$. Matrix $\mathbf{M}$ consists of the coefficients next to the unknowns A_1, C_1, etc. and it looks like

$$\left(\begin{array}{cccc}
I_\nu(k_1\rho) & 0 & -A_2 J_\nu(k_2\rho) & -B_2 Y_\nu(k_2\rho) \\
\tfrac{\nu}{k_1^2\rho} I_\nu(k_1\rho) & \tfrac{\omega\mu_1}{k_1\beta} I'_\nu(k_1\rho) & -\tfrac{\nu}{k_2^2\rho} J_\nu(k_2\rho) & -\tfrac{\nu}{k_2^2\rho} Y_\nu(k_2\rho) \\
0 & I_\nu(k_1\rho) & 0 & 0 \\
\tfrac{\omega\epsilon_1}{k_1\beta} I'_\nu(k_1\rho) & C_1 \tfrac{\nu}{k_1^2\rho} I_\nu(k_1\rho) & -\tfrac{\omega\epsilon_2}{k_2\beta} J'_\nu(k_2\rho) & -\tfrac{\omega\epsilon_2}{k_2\beta} Y'_\nu(k_2\rho) \\
0 & 0 & J_\nu(k_2R) & Y_\nu(k_2R) \\
0 & 0 & \tfrac{\nu}{k_2^2R} J_\nu(k_2R) & \tfrac{\nu}{k_2^2R} Y_\nu(k_2R) \\
0 & 0 & 0 & 0 \\
0 & 0 & \tfrac{\omega\epsilon_2}{k_2\beta} J'_\nu(k_2R) & \tfrac{\omega\epsilon_2}{k_2\beta} Y'_\nu(k_2R)
\end{array}\right. \cdots$$

$$\cdots \left.\begin{array}{cccc}
0 & 0 & 0 & 0 \\
-\tfrac{\omega\mu_2}{k_2\beta} J'_\nu(k_2\rho) & -\tfrac{\omega\mu_2}{k_2\beta} Y'_\nu(k_2\rho) & 0 & 0 \\
-J_\nu(k_2\rho) & -Y_\nu(k_2\rho) & 0 & 0 \\
-\tfrac{\nu}{k_2^2\rho} J_\nu(k_2\rho) & -\tfrac{\nu}{k_2^2\rho} Y_\nu(k_2\rho) & 0 & 0 \\
0 & 0 & K_\nu(k_3R) & 0 \\
\tfrac{\omega\mu_2}{k_2\beta} J'_\nu(k_2R) & \tfrac{\omega\mu_2}{k_2\beta} Y'_\nu(k_2R) & -\tfrac{\nu}{k_3^2\rho} K_\nu(k_3R) & -\tfrac{\omega\mu_3}{k_3\beta} K'_\nu(k_3R) \\
J_\nu(k_3R) & Y_\nu(k_3R) & 0 & K_\nu(k_3R) \\
\tfrac{\nu}{k_2^2R} J_\nu(k_2R) & \tfrac{\nu}{k_2^2R} Y_\nu(k_2R) & -\tfrac{\omega\epsilon_3}{k_3\beta} K'_\nu(k_3R) & -\tfrac{\nu}{k_3^2R} K_\nu(k_3R)
\end{array}\right) \tag{D.29}$$

Now, the equation $\det(\mathbf{M}) = 0$ has two independent variables, azimuthal mode number ν, which is an integer, and the propagation constant β, which is in general a complex number. So in theory there are many pairs of values that satisfy the equation. The easiest approach is to fix the azimuthal mode number, and then solve for the propagation constant β. These values are then plugged back into Equation D.29 and then we solve Equation D.28 from which we obtain coefficients A_1, C_1, A_2 etc. which in turn gives us the full solution for electric field $\mathbf{E}$ and magnetic field $\mathbf{H}$ in all 3 regions of Figure D.1.

D.3.1 Special cases

There are two special cases that drastically simplify the problem. Those are the pure TE and TM modes for which $E_z = 0$ and $H_z = 0$ respectively. In TE case, matrix equation D.28 simplifies to

$$\begin{pmatrix} C_1 \\ C_2 \\ D_2 \\ C_3 \end{pmatrix} \begin{pmatrix} \frac{\omega\mu_1}{k_1\beta} I'_\nu(k_1\rho) & -\frac{\omega\mu_2}{k_2\beta} J'_\nu(k_2\rho) & -\frac{\omega\mu_2}{k_2\beta} Y'_\nu(k_2\rho) & 0 \\ I_\nu(k_1\rho) & -J_\nu(k_2\rho) & -Y_\nu(k_2\rho) & 0 \\ 0 & \frac{\omega\mu_2}{k_2\beta} J'_\nu(k_2R) & \frac{\omega\mu_2}{k_2\beta} Y'_\nu(k_2R) & -\frac{\omega\mu_3}{k_3\beta} K'_\nu(k_3R) \\ 0 & J_\nu(k_3R) & Y_\nu(k_3R) & K_\nu(k_3R) \end{pmatrix} = \begin{pmatrix} 0 \\ 0 \\ 0 \\ 0 \end{pmatrix}$$

while for the TM case we have

$$\begin{pmatrix} A_1 \\ A_2 \\ B_2 \\ A_3 \end{pmatrix} \begin{pmatrix} I_\nu(k_1\rho) & -A_2 J_\nu(k_2\rho) & -B_2 Y_\nu(k_2\rho) & 0 \\ \frac{\omega\epsilon_1}{k_1\beta} I'_\nu(k_1\rho) & -\frac{\omega\epsilon_2}{k_2\beta} J'_\nu(k_2\rho) & -\frac{\omega\epsilon_2}{k_2\beta} Y'_\nu(k_2\rho) & 0 \\ 0 & J_\nu(k_2R) & Y_\nu(k_2R) & K_\nu(k_3R) \\ 0 & \frac{\omega\epsilon_2}{k_2\beta} J'_\nu(k_2R) & \frac{\omega\epsilon_2}{k_2\beta} Y'_\nu(k_2R) & -\frac{\omega\epsilon_3}{k_3\beta} K'_\nu(k_3R) \end{pmatrix} = \begin{pmatrix} 0 \\ 0 \\ 0 \\ 0 \end{pmatrix}.$$

It is quite obvious that these are much simpler, and consequently much quicker equations to solve. However to be able to solve for the hybrid modes too, one must include all terms and go back to the full expression of equation D.29.

D.4 Numerical solver, results and discussion

The actual solution of the Equation D.28 is obtained numerically. First, we fix the azimuthal mode number ν to a desired value. Using MATLAB® software a code was written to find complex values of propagation constant β for which $|\det(\mathbf{M})| = 0$. The absolute value is needed because the elements of the matrix $\mathbf{M}$ are complex in general. This process is carried out using the constrained minimization (`fmincon`) function from the MATLAB® optimization toolbox. From here on the rest of the process is pretty trivial.

To compare the performance and accuracy of our solver, we chose a model geometry and solved it both using the custom written code in MATLAB®, and with the finite element method using COMSOL® Multiphysics with RF module. Comparison of the results is shown in Figure D.2. It is obvious that both the field profile and the effective index n_{eff} are in excellent agreement between the two solvers. Note that the propagation constant is given as $\beta = 2\pi/\lambda{\cdot}n_{\mathit{eff}}$ where λ is the wavelength. Because we are dealing with real metal, there is loss associated with field-metal interaction, and that is why n_{eff} has an imaginary part. We here adhere to the convention that positive sign of the imaginary part of index represents loss, while negative sign represents gain (active material). Since both solvers apparently produce the same results, we need to look at the strengths and weaknesses of each one. The main advantage of using the analytic approach is the speed with which the code runs. For the comparison example that was just mentioned, the FEM solver took ~ 200 seconds to complete (little over 3 min), while the analytical solver completed the task in ~ 20 seconds. But it is not until one tries to optimize the geometry for the best performance that this time saving really becomes apparent. Because in the process of optimization functions are evaluated thousands of times for varying parameters, these time savings really start to add up.

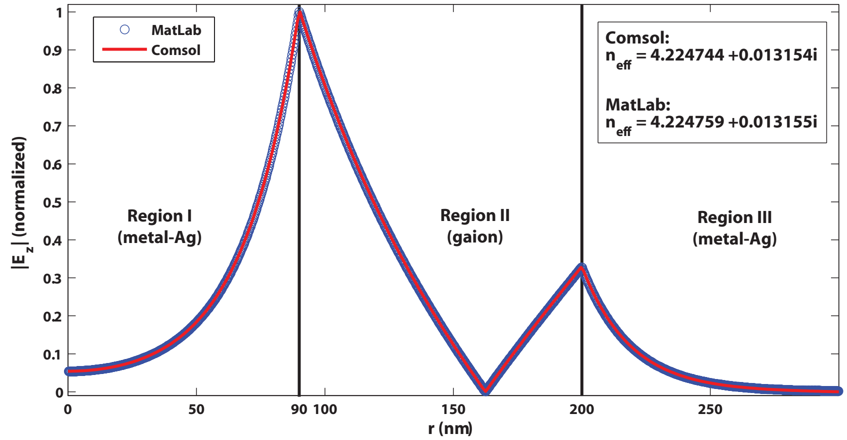

Figure D.2: Comparison of commercial FEM COMSOL® and custom MATLAB® solver. Profile of the normalized E_z for coaxial structure depicted in Figure D.1 with $\rho = 90\,\mathrm{nm}$ and $R = 200\,\mathrm{nm}$.

Conversely, the weakness of the analytic code is that it is capable of solving only very limited set of problems. For instance, if we introduce some ellipticity in our design, our analytic code becomes useless. This is a serious issue if we try to simulate the actual fabricated samples, as all of them suffer from small imperfections which can't be ignored at this scale ($\sim 500\,\mathrm{nm}$). Moreover, the code in its present form is limited to 2D problems i.e. it treats the design as infinite along the z axis.[1] The analytic approach for the realistic (rather than ideal) coaxial nanolasers is impractical. One difficulty is the Finite z dimension, but the radiative boundary conditions at the edge of the metal, where device ends, are quite difficult to do in closed form such as we proposed here. This analytical tool should be seen as a way to reasonaby quickly optimize the geometry of the device, and then employ full 3D FEM solver, such as COMSOL ®, for final analysis.

---

[1] Because of the 2D nature of this approach it makes it perfectly suitable for treatment of optical fibers. As a matter of fact, very similar matrix approach is used to successfully treat multi-layer Bragg fibers [129, 130].

Appendix E

Explanation of the Purcell effect

Throughout this dissertation we mention the Purcell effect quite often, without fully explaining what it is. Here, we will discuss the Purcell effect in a little more detail. In his seminal work [88] Edward Purcell discovered that the spontaneous emission rate depends not only on the atom, but on the environment in which an atom is placed as well. It is truly fascinating that a work of this magnitude is so concisely written, so we are reproducing his text below for the interest of the reader.

> For nuclear magnetic moment transitions at radio frequencies the probability of spontaneous emission, computed from
>
> $$A_\nu = (8\pi\nu^2/c^3)h\nu(8\pi^3\mu^2/3h^2)\,\text{sec.}^{-1}$$
>
> is so small that this process is not effective in bringing a spin system into thermal equilibrium with its surroundings. At 300 K, for $\nu = 10^7\,\text{sec.}^{-1}$, $\mu = 1$ nuclear magneton, the corresponding relaxation time would be 5×10^{21} seconds! However, for a system coupled to a resonant electrical circuit, the factor $8\pi\nu^2/c^3$ no longer gives correctly the number of radiation oscillators per unit volume, in unit frequency range, there being now *one* oscillator in the frequency range ν/Q associated with the circuit. The spontaneous emission probability is thereby increased, and the relaxation time reduced, by a factor $f = 3Q\lambda^3/4\pi^2V$, where V is the volume of the resonator. If a is a dimension characteristic of the circuit so that $V \sim a^3$, and if δ is the skin-depth at frequency ν, $f \sim \lambda^3/a^2\delta$. For a non-resonant circuit $f \sim \lambda^3/a^3$, and for $a < \delta$ it can be shown that $f \sim \lambda^3/a\delta^2$. If small metallic particles, of diameter

> 10^{-3} cm are mixed with a nuclear-magnetic medium at room temperature, spontaneous emission should establish thermal equilibrium in a time of the order of minutes, for $\nu = 10^7$ sec.$^{-1}$.

Although inspired by nuclear magnetic resonance (NMR), this effect is quite applicable in nano-optics, especially in the field of nanolasers. To better understand its significance and meaning for nanolasers we must discuss spontaneous emission of photons (luminescence) by optical gain materials. Spontaneous emission of a photon occurs when an electron transitions from a higher to lower energy state without the aid of an incident photon. These transitions are governed by Fermi's golden rule, and they are allowed or not depending on the initial and the final states of the electron in question. So then the collection of *all* possible transitions (all possible photon energies) forms a luminescence spectrum of the gain medium, which is usually broad (see Figure 4.1 for example). So far we assumed that the gain material sits in free space. What changes when we place this material in a resonant cavity? Now, only the transitions whose frequency satisfies the resonance condition of the cavity are allowed. In other words, only part of the luminescence spectrum is allowed. In lasers with large cavities, the free spectral range is really short (recall $\Delta\nu \approx c/2nL$) so the luminescence spectrum looks like a fine comb, which, after we take into account broadening, is essentially identical to the free-space luminescence spectrum. In contrast, if we have a very small cavity with sparse number of possible modes, then the luminescence spectrum is much different, and emission is allowed only in one of the cavity modes. This is essentially the meaning of the Purcell effect. Spontaneous emission into the free-space modes is suppressed in favor of emission into cavity mode(s) by a factor

$$F = \frac{3}{4\pi^2}\left(\frac{\lambda_0}{n}\right)^3 \frac{Q}{V}$$

where λ_0/n is the wavelength in the medium, Q is the quality factor and V is the volume of the cavity. Depending on the intention, one can design a cavity that supports only the modes which do not overlap with the gain spectrum at all, thereby suppressing the spontaneous emission altogether.[1] Conversely, we can design the

---

[1] Actually, one needs to be careful about statements like this one since emission into free-space modes is possible via leaky reflectors of the cavity — essentially the Q of the cavity.

cavity in such a way to favor the emission into the lasing mode, thereby reducing the threshold gain requirements. Up until a few years ago, direct observations of the Purcell effect were impossible, and only now with the advancements in the field of nanolasers experimental verification has become a reality [78].

Appendix F

Second order coherence $g^{(2)}$

F.1 Background information on coherence

Coherence is one of the fundamental properties of laser light. It is usually defined as the ability of two waves to form stationary (in time) fringes. What this means is that there is a well defined phase relationship between the two waves. The degree to which two waves are coherent is measured in fringe visibility v

$$v = \frac{Amplitude}{Average} = \frac{I_{max} - I_{min}}{\frac{I_{max}+I_{min}}{2}} = \frac{2\sqrt{I_1 I_2}}{I_1 + I_2} \tag{F.1}$$

where I_{min} and I_{max} are the minimum and the maximum intensity in the fringes, and I_1 and I_2 are the respective intensities of the two interfering waves (which need not be equal). Another important distinction is between spatial and temporal coherence. Spatial coherence represents a measure of constant phase relation between two points on the wavefront. Temporal coherence on the other hand is a measure of constant phase relation between the wave at times t and $t + \tau$. In this section we are discussing temporal coherence, which is also related to monochromaticity of the wave as $t_c \Delta\nu \approx 1$, where t_c is the coherence time and $\Delta\nu$ frequency bandwidth.

F.2 Quantum (QED) treatment of coherence

It should be obvious from the above paragraph that the coherence is related to, and can be represented as correlation. We will now establish this connection quite clearly by looking into the electric field detection process and its relation to correlation. It is convenient to do so by looking at the quantum (QED) representation of the electric field–matter interaction. Following the treatment of Glauber who developed the quantum theory of coherence [131], we introduce here the photon creation operator $\mathbf{E}^{(-)}$ and photon annihilation operator $\mathbf{E}^{(+)}$ (for the more comprehensive, textbook treatment of the quantum approach to coherence see [132]). The transition probability of a detector absorbing a photon at a position $\mathbf{r}$ and time t is then $T_{if} = \left|\langle f|\mathbf{E}^{(+)}(\mathbf{r},t)|i\rangle\right|^2$ where $|i\rangle$ and $|f\rangle$ are initial and final states of the photon. So to get the total average field intensity, we need to sum over all possible final states

$$I(\mathbf{r},t) = \sum_f \langle i|\mathbf{E}^{(-)}(\mathbf{r},t)|i\rangle\langle f|\mathbf{E}^{(+)}(\mathbf{r},t)|i\rangle = \langle i|\mathbf{E}^{(-)}(\mathbf{r},t)\mathbf{E}^{(+)}(\mathbf{r},t)|i\rangle \tag{F.2}$$

where we assume that the electric field is initially in a pure $|i\rangle$ state. This is oversimplification that can be remedied by averaging over all initial states and assigning them each probability P_i.

$$I(\mathbf{r},t) = \sum_i P_i\langle i|\mathbf{E}^{(-)}(\mathbf{r},t)\mathbf{E}^{(+)}(\mathbf{r},t)|i\rangle = \mathrm{Tr}\left\{\rho\mathbf{E}^{(-)}(\mathbf{r},t)\mathbf{E}^{(+)}(\mathbf{r},t)\right\} \tag{F.3}$$

Here $\rho = \sum_i P_i|i\rangle\langle i|$ is the probability density operator. Now if we define two space-time points $x = (\mathbf{r},t)$ and $x' = (\mathbf{r},t')$ we can write a fist order correlation function between those two points as

$$G^{(1)}(x,x') = \mathrm{Tr}\left\{\rho\mathbf{E}^{(-)}(x)\mathbf{E}^{(+)}(x')\right\} \tag{F.4}$$

and this can then be generalized to the n^{th} order as follows

$$G^{(n)}(x_1\ldots x_n, x_{n+1}\ldots x_{2n}) = \mathrm{Tr}\left\{\rho\mathbf{E}^{(-)}(x_1)\ldots\mathbf{E}^{(-)}(x_n)\mathbf{E}^{(+)}(x_{n+1})\ldots\mathbf{E}^{(+)}(x_{2n})\right\} \tag{F.5}$$

The crucial thing to note here is the difference between classical and quantum interpretation of Equation F.5. In classical terms, $\mathbf{E}^{(-)}$ and $\mathbf{E}^{(+)}$ represent positive and negative frequency components of the electric field, and those quantities *commute*. In the quantum interpretation, those are photon creation and annihilation operators and they in general *do not commute*. One way to think about that is that we have to create a photon first before we can detect it by annihilating it in the detector. This stark contrast between the two interpretations is what yields the different meaning of *coherent light* in classical and the quantum sense of the word, and it will become more apparent in the following section.

F.3 Young's double slit experiment and $g^{(1)}$

To show now how all of the elements developed thus far fall in place together we will look at the classical Young's double slit experiment schematically represented in Figure F.1. The detection of a photon at position $\mathbf{r}$ now depends on fields emanating from points $\mathbf{r}_1$ and $\mathbf{r}_2$ and is given as

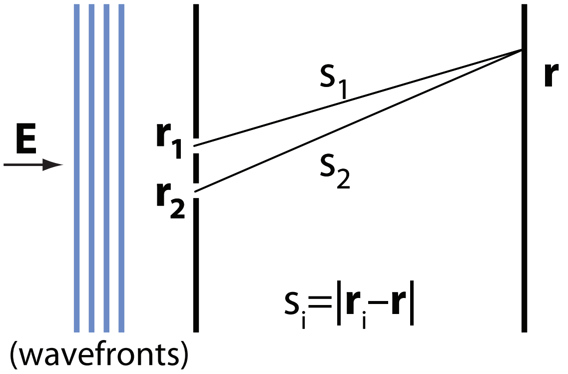

Figure F.1: Schematic representation of Young's double slit experiment.

$$\mathbf{E}^{(+)}(\mathbf{r},t) = \sum_i \mathbf{E}_i^{(+)}\left(\mathbf{r}_i, t - \frac{s_i}{c}\right)\left(\frac{1}{s_i}\right) e^{j(k-\omega/c)} \tag{F.6}$$

which can be further simplified by assuming spherical wavefronts ($k = \omega/c$) which drops the exponent. Also if we assume that the two slits are close together compared to the distance to the screen, i.e. $s_1 \approx s_2 \equiv R$, the equation becomes

$$\mathbf{E}^{(+)}(\mathbf{r},t) = \frac{1}{R}\left[\mathbf{E}_1^{(+)}(x_1) + \mathbf{E}_2^{(+)}(x_2)\right] \qquad \text{where} \qquad x_i = (\mathbf{r}_i, t - s_i/c) \tag{F.7}$$

If we now combine equations F.3, F.4 and F.7 we get the expression for intensity at position **r** in terms of first order correlation function

$$I = G^{(1)}(x_1, x_1) + G^{(1)}(x_2, x_2) + 2\Re\left\{G^{(1)}(x_1, x_2)\right\} \tag{F.8}$$

and if we rewrite $G^{(1)}(x_1, x_2) = \left|G^{(1)}(x_1, x_2)\right| e^{i\phi(x_1,x_2)}$ then equation F.8 becomes

$$I = G^{(1)}(x_1, x_1) + G^{(1)}(x_2, x_2) + 2\left|G^{(1)}(x_1, x_2)\right| \cos[\phi(x_1, x_2)] \tag{F.9}$$

where the last term of the equation is the familiar interference term, while the first two terms represent baseline offset. We can now introduce the normalized first order coherence function

$$g^{(1)}(x_1, x_2) = \frac{G^{(1)}(x_1, x_2)}{\left[G^{(1)}(x_1, x_1)G^{(1)}(x_2, x_2)\right]^{1/2}} \tag{F.10}$$

whose magnitude is always less than one due to Cauchy-Schwartz inequality $\left|G^{(1)}(x_1, x_2)\right| \leq \left[G^{(1)}(x_1, x_1)G^{(1)}(x_2, x_2)\right]^{1/2}$. Looking back at the visibility equation F.1, we can now rewrite it [132] as

$$v = \left|g^{(1)}\right| \frac{2\sqrt{I_1 I_2}}{I_1 + I_2} \qquad \text{and if } I_1 = I_2 \text{ then} \qquad v = \left|g^{(1)}\right| \tag{F.11}$$

from which it follows that maximum visibility is achieved when the first order coherence function is equal to 1. So first order coherence is enough to explain all Young's-type interference experiments as well as Michelson-Morley-type experiments. This means that such experiments are simply inadequate to distinguish quantum light (such as laser) from classical light (collision broadened). This is not in any way surprising because historically, the Michelson-Morley experiment was performed with classical light (sunlight). In order to make that distinction between classical and quantum light, we must look into higher order coherence functions

$$g^{(n)}(x_1 \ldots x_{2n}) = \frac{G^{(n)}(x_1 \ldots x_{2n})}{\prod_{j=1}^{2n} \left[G^{(1)}(x_j, x_j)\right]^{1/2}}. \tag{F.12}$$

Note that for light to be *truly* coherent in the quantum sense, we must have $|g^{(n)}| = 1$ for all values of n.

F.4 Second order coherence function — $g^{(2)}$

As we saw, QED is not needed to treat first order coherence as the above results can be exactly derived in completely classical terms. So wee need to look at higher order coherence functions to contrast the classical and QED treatment. The lowest *higher order* coherence function, and the simplest to treat mathematically is the second order function $g^{(2)}$. Following Equation F.12 we can write

$$g^{(2)}(\mathbf{r}_1,t_1,\mathbf{r}_2,t_2;\mathbf{r}_2,t_2,\mathbf{r}_1,t_1) = \frac{\left\langle \mathbf{E}^{(-)}(\mathbf{r}_1,t_1)\mathbf{E}^{(-)}(\mathbf{r}_2,t_2)\mathbf{E}^{(+)}(\mathbf{r}_2,t_2)\mathbf{E}^{(+)}(\mathbf{r}_1,t_1)\right\rangle}{\left\langle \mathbf{E}^{(-)}(\mathbf{r}_1,t_1)\mathbf{E}^{(+)}(\mathbf{r}_1,t_1)\right\rangle \left\langle \mathbf{E}^{(-)}(\mathbf{r}_2,t_2)\mathbf{E}^{(+)}(\mathbf{r}_2,t_2)\right\rangle} \tag{F.13}$$

where angle brackets represent the ensemble average and $\mathbf{E}^{(-)}$ and $\mathbf{E}^{(+)}$ are creation and annihilation operators as before. It is *crucial* to note again that these *do not* necessarily commute. If we make the assumptions that two position vectors $\mathbf{r}_1$ and $\mathbf{r}_2$ are parallel and propagate along the z axis, then the two space-time arguments of $g^{(2)}$ can be redefined as $\tau = t_2 - t_1 + (z_1 - z_2)/c$ we can rewrite the equation F.13 as

$$g^{(2)}(\tau) = \frac{\left\langle \mathbf{E}^{(-)}(t)\mathbf{E}^{(-)}(t+\tau)\mathbf{E}^{(+)}(t+\tau)\mathbf{E}^{(+)}(t)\right\rangle}{\left\langle \mathbf{E}^{(-)}(t)\mathbf{E}^{(+)}(t)\right\rangle \left\langle \mathbf{E}^{(-)}(t+\tau)\mathbf{E}^{(+)}(t+\tau)\right\rangle} \tag{F.14}$$

If we for now restrict ourselves to classical light, we could show [132] that $g^{(2)}(\tau) = 1 + \left|g^{(1)}(\tau)\right|^2$ which limits its values between 1 for incoherent to 2 for coherent light (here we talk about *first order coherence* only!). So the condition for what we labeled "truly coherent light in the QED sense" is not met (not surprisingly). Furthermore, if we consider the classical electric field to have amplitude (ε) fluctuation, and we assign a probability distribution $P(\varepsilon)$, then the electric field can be written in the form $E(\varepsilon, t) \sim \varepsilon e^{-i\omega t}$ and for zero time delay $g^{(2)}$ becomes

$$g^{(2)}(0) = 1 + \frac{\int P(\varepsilon)\left(|\varepsilon|^2 - \left\langle |\varepsilon|^2 \right\rangle\right)^2}{\left(\left\langle |\varepsilon|^2 \right\rangle\right)^2} \tag{F.15}$$

which obviously *can not* have a value outside of interval $[1, 2]$ since probability distribution P always has values between 0 and 1. This essentially proves that for classical fields $g^{(2)}(0) > 1$.

In contrast, if we look at single mode light (such as laser) in the quantum representation, $g^{(2)}$ becomes [132]

$$g^{(2)}(0) = \frac{\langle n(n-1)\rangle}{\langle n\rangle^2} \tag{F.16}$$

from which it is immediately apparent that for a large number of photons $g^{(2)}(0) = 1$ contrary to the case of classical light. Furthermore, if we have very few photons $g^{(2)}(0) < 1$, and for a single photon (like a single-atom laser [133]) $g^{(2)}(0) = 0$! As we saw before, there is no classical explanation for this behavior. The only question is how do we observe it?

F.5 Measuring second order coherence — $g^{(2)}(0)$

F.5.1 Hanbury Brown and Twiss experiment

The first measurements of second order correlation were performed by Hanbury Brown and Twiss (HBT)in 1956 [113], before the invention of the maser or laser and before QED. Their experimental setup was rather simple. It consisted of two detectors, separated some distance apart, connected to a coincidence counter. Both detectors were pointing at the photon source that was emitting ~ 1 photon at the time (they used the light from a distant star).[1] Because the light was coming from a star many lightyears away, the distance between the detectors was insignificant, and the measured correlation was thus $g^{(2)}(0)$. An updated HBT experiment (schematic presented in Figure F.2) uses a beam splitter to separate an incoming beam of light into two parts, sending each one to a separate detector. Here, one must make sure that the optical path lengths between the beam splitter and the two detectors are identical (within a coherence length).

In their original experiment, Hanbury Brown and Twiss expected to see no correlation between the two detector signals. After all, they were dealing with the signal of ~ 1 photon at the time, so it is logical to expect that said photon would

---

[1] Although we are discussing temporal coherence here, the original HBT experiment was, strictly speaking, measuring *spatial* coherence of the light. It was looking at two points on the wavefront (two detectors separaed some distance apart). This does not change validity of the arguments presented here. We are only noting it for the sake of historical accuracy.

land either on detector D1 or on the detector D2. Much to their surprise, HB&T measured $g^{(2)}(0) = 2$. This meant that photons were arriving at the detectors in pairs, and if one detector registered a photon, there was large probability that the other one registered it too at the same time. This phenomenon is called "photon bunching" or the Hanbury Brown-Twiss effect. The same experimental principle with a modified setup (as in Figure F.2) was used recently to measure $g^{(2)}(\tau)$ of micro-disk lasers [134]. Their work verifies the predictions we made in this appendix, that when laser is actually lasing, $g^{(2)}(0) = 1$. This is a really powerful and unambiguous way to confirm the light emitted by a laser is actually stimulated, and not spontaneous emission.

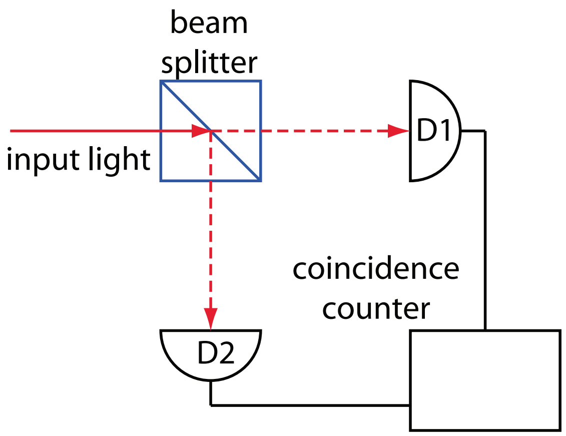

Figure F.2: Schematic representation of modified Hanbury Brown Twiss experiment.

Unfortunately, we cannot use this approach in our nanolasers. The problem is primarily that our lasers in general suffer from a poor Q factor (depending on the design anywhere from ~ 20 to $\sim 1{,}500$) which in turn makes their linewidth rather broad (typically over 1 nm). Linewidth is related to coherence time as $t_c \approx \lambda_0^2/c\Delta\lambda$ which for the central wavelength of 1.5 µm amounts to $t_c \sim 10\,\mathrm{ps}$, and this is a best case scenario (some of the lasers have coherence time below a picosecond). Thus we must be able to detect coincidences with a resolution much better then a picosecond, and that is simply not possible with. Current state of the art equipment is able to do this with resolution of about 500 ps, which for our purposes this is too slow.

F.5.2 Streak camera approach

Another approach to measure the second (and higher!) order coherence function is to use a streak camera. A streak camera is a device that consists of a photocathode followed by parallel plate capacitor and a phosphorus screen. When photons are incident on the photocathode they get converted into electrons, accelerated and then deflected with the electric field from the parallel plate capacitor, after which they land onto the phosphorous screen, and then a snapshot is taken with a CCD camera. What this allows is to look at the pulses of a pulsed laser source, and then spread them such that we temporally resolve individual photons in each pulse. We then have a complete record of times of arrival for individual photons within each pulse, and we can look for coincident pairs of photons and compute second order correlation. We can also look for coincident triplets for third order correlation and so on. This method was proposed and carried out in [114].

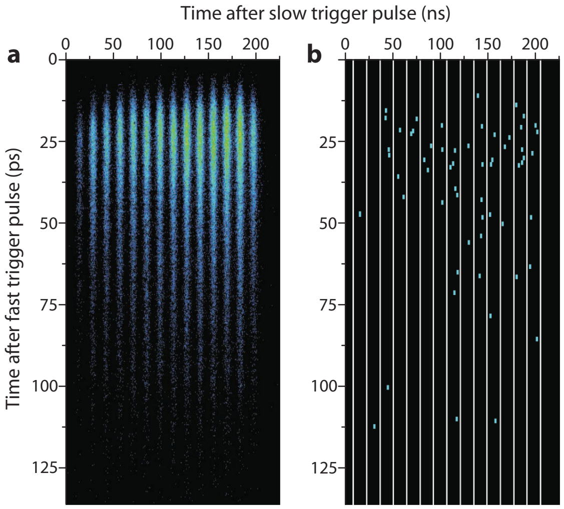

Figure F.3: Figure taken from [114]. Using a streak camera to measure $g^{(2)}(\tau)$ **(a)** aggregate data of 60,000 screens. **(b)** a typical screen taken from **(a)** each of the vertical bins represents a separate laser pulse, separated by 13.2 ns along the horizontal (slow) axis. Each individual pulse is spread out over the fast axis, and each dot represents a single event (electron lending to a phosphorus screen). This provides us with an exact time record of arrival of each individual photon, from which we can compute $g^{(2)}(\tau)$ and even higher order coherence functions.

The benefits of this method are first and foremost greatly improved temporal resolution (it is down to 2 ps from 500 ps in HBT method). This method also allows for measurement of even higher order coherence functions. The disadvantages for applications with our lasers are that current streak camera technology relies on Si based photocathodes, and this means that wavelengths of $\sim 1.5\,\mu\text{m}$ are simply out of the question, as the efficiency of the photocathode at these wavelength is down by more then 5 orders of magnitude [135] compared to the efficiency at 800 nm. In other words, the technology is unfortunately not yet available to be able to characterize our lasers in this manner.

Bibliography

[1] S. Drake, N. Swerdlow, and T. Levere, *Essays on Galileo and the History and Philosophy of Science*, vol. 1. University of Toronto Press, 1999.

[2] L. de Broglie, "Recherches sur la théorie des quanta (researches on the quantum theory)," *Ann. Phys.(Paris)*, vol. 3, p. 22, 1925.

[3] J. Pendry, A. Holden, D. Robbins, and W. Stewart, "Magnetism from conductors and enhanced nonlinear phenomena," *IEEE Transactions on Microwave Theory and Techniques*, vol. 47, no. 11, pp. 2075–2084, 1999.

[4] D. R. Smith, W. J. Padilla, D. C. Vier, S. C. Nemat-Nasser, and S. Schultz, "Composite medium with simultaneously negative permeability and permittivity," *Physical Review Letters*, vol. 84, p. 4184, May 2000.

[5] R. A. Shelby, D. R. Smith, and S. Schultz, "Experimental verification of a negative index of refraction," *Science*, vol. 292, pp. 77 –79, Apr. 2001.

[6] T. Yen, W. Padilla, N. Fang, D. Vier, D. Smith, J. Pendry, D. Basov, and X. Zhang, "Terahertz magnetic response from artificial materials," *Science*, vol. 303, no. 5663, p. 1494, 2004.

[7] S. Zhang, W. Fan, B. Minhas, A. Frauenglass, K. Malloy, and S. Brueck, "Midinfrared resonant magnetic nanostructures exhibiting a negative permeability," *Physical review letters*, vol. 94, no. 3, p. 37402, 2005.

[8] S. Linden, C. Enkrich, M. Wegener, J. Zhou, T. Koschny, and C. Soukoulis, "Magnetic response of metamaterials at 100 terahertz," *Science*, vol. 306, no. 5700, p. 1351, 2004.

[9] A. Grigorenko, A. Geim, H. Gleeson, Y. Zhang, A. Firsov, I. Khrushchev, and J. Petrovic, "Nanofabricated media with negative permeability at visible frequencies," *Nature Photonics*, vol. 438, no. 7066, p. 335, 2005.

[10] A. Kildishev, W. Cai, U. Chettiar, H. Yuan, A. Sarychev, V. Drachev, and V. Shalaev, "Negative refractive index in optics of metal-dielectric composites," *JOSA B*, vol. 23, no. 3, pp. 423–433, 2006.

[11] C. Enkrich, M. Wegener, S. Linden, S. Burger, L. Zschiedrich, F. Schmidt, J. Zhou, T. Koschny, and C. Soukoulis, “Magnetic metamaterials at telecommunication and visible frequencies,” *Physical review letters*, vol. 95, no. 20, p. 203901, 2005.

[12] J. Pendry, “Negative refraction makes a perfect lens,” *Physical Review Letters*, vol. 85, no. 18, pp. 3966–3969, 2000.

[13] J. Pendry, D. Schurig, and D. Smith, “Controlling electromagnetic fields,” *Science*, vol. 312, no. 5781, p. 1780, 2006.

[14] U. Leonhardt, “Optical conformal mapping,” *Science*, vol. 312, no. 5781, p. 1777, 2006.

[15] D. Schurig, J. Mock, B. Justice, S. Cummer, J. Pendry, A. Starr, and D. Smith, “Metamaterial electromagnetic cloak at microwave frequencies,” *Science*, vol. 314, no. 5801, p. 977, 2006.

[16] M. Nathan, W. Dumke, G. Burns, F. Dill, and G. Lasher, “Stimulated emission of radiation from gaas p-n junctions,” *Applied Physics Letters*, vol. 1, no. 3, pp. 62–64, 1962.

[17] R. Hall, G. Fenner, J. Kingsley, T. Soltys, and R. Carlson, “Coherent light emission from gaas junctions,” *Physical Review Letters*, vol. 9, no. 9, pp. 366–368, 1962.

[18] H. Soda, K. Iga, C. Kitahara, and Y. Suematsu, “Gainasp/inp surface emitting injection lasers,” *Japanese journal of applied physics*, vol. 18, no. 12, pp. 2329–2330, 1979.

[19] F. Koyama, S. KINOSHITA, and K. IGA, “Room temperature cw operation of gaas vertical cavity surface emitting laser,” *IEICE TRANSACTIONS*, vol. 1976, 1988.

[20] S. McCall, A. Levi, R. Slusher, S. Pearton, and R. Logan, “Whispering-gallery mode microdisk lasers,” *Applied physics letters*, vol. 60, no. 3, pp. 289–291, 1992.

[21] P. Jin Shan, C. Po Hsiu, L. Tsin Dong, L. Yinchieh, and T. Kuochou, “0.66 µm InGaP/InGaAlP single quantum well microdisk lasers,” *Japanese Journal of Applied Physics, Part 2*, vol. 37, pp. L643–L645, 1998.

[22] V. Sandoghdar, F. Treussart, J. Hare, V. Lefevre-Seguin, J. Raimond, and S. Haroche, “Very low threshold whispering-gallery-mode microsphere laser,” *Physical Review A*, vol. 54, no. 3, pp. 1777–1780, 1996.

[23] O. Painter, R. Lee, A. Scherer, A. Yariv, J. O'brien, P. Dapkus, and I. Kim, "Two-dimensional photonic band-gap defect mode laser," *Science*, vol. 284, no. 5421, p. 1819, 1999.

[24] H. Park, S. Kim, S. Kwon, Y. Ju, J. Yang, J. Baek, S. Kim, and Y. Lee, "Electrically driven single-cell photonic crystal laser," *Science*, vol. 305, no. 5689, p. 1444, 2004.

[25] M. Hill, Y. Oei, B. Smalbrugge, Y. Zhu, T. De Vries, P. van Veldhoven, F. van Otten, T. Eijkemans, J. Turkiewicz, H. de Waardt, *et al.*, "Lasing in metallic-coated nanocavities," *Nature Photonics*, vol. 1, no. 10, pp. 589–597, 2007.

[26] D. A. G. Bruggemann, "Berechnung verschiedener physikalischer Konstanten von heterogenen Substanzen. I. Dielectrizitätkonstanten und Leitfähigkeiten der Mischkörper aus isotropen Substanzen," *Annalen der Physik (1900)*, vol. 22, pp. 636–679, 1935.

[27] D. A. G. Bruggemann, "Berechnung verschiedener physikalischer Konstanten von heterogenen Substanzen. III. Die elastische Konstanten der Quasiisotropen Mischkörper aus isotropen Substanzen," *Annalen der Physik (1900)*, vol. 29, pp. 160–178, 1937.

[28] J. Pendry, A. Holden, W. Stewart, and I. Youngs, "Extremely low frequency plasmons in metallic mesostructures," *Physical Review Letters*, vol. 76, no. 25, pp. 4773–4776, 1996.

[29] V. Veselago, "Electrodynamics of substances with simultaneously negative values of σ and μ," *Soviet Physics Uspekhi - USSR*, vol. 10, no. 4, pp. 509–514, 1968.

[30] S. Schuster, *An introduction to the theory of optics.* E. Arnold, 1904.

[31] H. Lamb, "On group-velocity," *Proceedings of the London Mathematical Society*, vol. 2, no. 1, p. 473, 1904.

[32] L. Mandel'shtam, "Group velocity in a crystal lattice," *JETP*, vol. 15, p. 475, 1945.

[33] D. Sivukhin, "The energy of electromagnetic waves in dispersive media," *Optics and Spectroscopy*, vol. 3, pp. 308–312, 1957.

[34] V. Shalaev, "Optical negative-index metamaterials," *Nature Photonics*, vol. 1, no. 1, pp. 41–48, 2007.

[35] M. Bayindir, K. Aydin, E. Ozbay, P. Markoš, and C. Soukoulis, "Transmission properties of composite metamaterials in free space," *Applied Physics Letters*, vol. 81, p. 120, 2002.

[36] R. Greegor, C. Parazzoli, K. Li, B. Koltenbah, and M. Tanielian, “Experimental determination and numerical simulation of the properties of negative index of refraction materials,” *Optics Express*, vol. 11, pp. 688–695, Apr. 2003.

[37] C. Li, “Negative lateral shift of a light beam transmitted through a dielectric slab and interaction of boundary effects,” *Physical review letters*, vol. 91, no. 13, p. 133903, 2003.

[38] X. Chen and C. Li, “Lateral shift of the transmitted light beam through a left-handed slab,” *Physical Review E*, vol. 69, no. 6, p. 066617, 2004.

[39] N. Engheta, “An idea for thin subwavelength cavity resonators using metamaterials with negative permittivity and permeability,” *Antennas and Wireless Propagation Letters, IEEE*, vol. 1, pp. 10–13, 2002.

[40] S. A. Cummer and B. Popa, “Wave fields measured inside a negative refractive index metamaterial,” *Applied Physics Letters*, vol. 85, no. 20, p. 4564, 2004.

[41] M. Zain, N. Johnson, M. Sorel, and R. De La Rue, “High quality-factor 1-D-suspended photonic crystal/photonic wire silicon waveguide micro-cavities,” *Photonics Technology Letters, IEEE*, vol. 21, no. 24, pp. 1789–1791, 2009.

[42] Y. Akahane, T. Asano, B. Song, and S. Noda, “High-Q photonic nanocavity in a two-dimensional photonic crystal,” *Nature*, vol. 425, no. 6961, pp. 944–947, 2003.

[43] Q. Song, H. Cao, S. Ho, and G. Solomon, “Near-IR subwavelength microdisk lasers,” *Applied Physics Letters*, vol. 94, p. 061109, 2009.

[44] E. Smotrova, A. Nosich, T. Benson, and P. Sewell, “Optical coupling of whispering-gallery modes of two identical microdisks and its effect on photonic molecule lasing,” *IEEE Journal of Selected Topics in Quantum Electronics*, vol. 12, no. 1, pp. 78–85, 2006.

[45] M. Nezhad, K. Tetz, and Y. Fainman, “Gain assisted propagation of surface plasmon polaritons on planar metallic waveguides,” *Optics Express*, vol. 12, no. 17, pp. 4072–4079, 2004.

[46] B. Min, E. Ostby, V. Sorger, E. Ulin-Avila, L. Yang, X. Zhang, and K. Vahala, “High-Q surface-plasmon-polariton whispering-gallery microcavity,” *Nature*, vol. 457, no. 7228, pp. 455–458, 2009.

[47] P. Johnson and R. Christy, “Optical constants of the noble metals,” *Physical Review B*, vol. 6, no. 12, pp. 4370–4379, 1972.

[48] E. Goebel, G. Luz, and E. Schlosser, “Optical gain spectra of InGaAsP/InP double heterostructures,” *IEEE Journal of Quantum Electronics*, vol. 15, no. 8, pp. 697–700, 1979.

[49] M. Körbl, A. Gröning, H. Schweizer, and J. Gentner, “Gain spectra of coupled InGaAsP/InP quantum wells measured with a segmented contact traveling wave device,” *Journal of Applied Physics*, vol. 92, p. 2942, 2002.

[50] M. Hill, M. Marell, E. Leong, B. Smalbrugge, Y. Zhu, M. Sun, P. van Veldhoven, E. Geluk, F. Karouta, Y. Oei, *et al.*, “Lasing in metal-insulator-metal sub-wavelength plasmonic waveguides,” *Optics Express*, vol. 17, no. 13, pp. 11107–11112, 2009.

[51] A. Mizrahi, V. Lomakin, B. Slutsky, M. Nezhad, L. Feng, and Y. Fainman, “Low threshold gain metal coated laser nanoresonators,” *Optics Letters*, vol. 33, no. 11, pp. 1261–1263, 2008.

[52] E. Palik and G. Ghosh, *Handbook of optical constants of solids: five-volume set*. Academic press, 1998.

[53] B. Bennett, R. Soref, and J. Del Alamo, “Carrier-induced change in refractive index of InP, GaAs, and InGaAsP,” *IEEE Journal of Quantum Electronics*, vol. 26, no. 1, 1990.

[54] C. Chua, R. Thornton, D. Treat, and R. Donaldson, “Independently addressable VCSEL arrays on 3 μm pitch,” *IEEE Photonics Technology Letters*, vol. 10, no. 7, pp. 917–919, 1998.

[55] A. Kroner, F. Rinaldi, R. Rosch, and R. Michalzik, “Optical particle manipulation by application-specific densely packed VCSEL arrays,” *Electronics Letters*, vol. 44, no. 5, pp. 353–354, 2008.

[56] R. Oulton, V. Sorger, T. Zentgraf, R. Ma, C. Gladden, L. Dai, G. Bartal, and X. Zhang, “Plasmon lasers at deep subwavelength scale,” *Nature*, vol. 461, no. 7264, pp. 629–632, 2009.

[57] D. Hatice Altug *et al.*, “Ultrafast photonic crystal nanocavity laser,” *Nature Physics*, vol. 2, no. 7, pp. 484–488, 2006.

[58] Z. Rao, L. Hesselink, and J. Harris, “High-intensity bowtie-shaped nano-aperture vertical-cavity surface-emitting laser for near-field optics,” *Optics Letters*, vol. 32, no. 14, pp. 1995–1997, 2007.

[59] B. Jensen and A. Torabi, “Refractive index of quaternary InGaAsP lattice matched to InP,” *Journal of Applied Physics*, vol. 54, p. 3623, 1983.

[60] C. Genet and T. Ebbesen, “Light in tiny holes,” *Nature*, vol. 445, no. 7123, pp. 39–46, 2007.

[61] K. Stubkjaer, M. Asada, S. Arai, and Y. Suematsu, “Spontaneous recombination, gain and refractive index variation for 1.6 microns wavelength InGaAsP/InP lasers,” *Japanese Journal of Applied Physics*, vol. 20, pp. 1499–1505, 1981.

[62] A. Goi, K. Syassen, and M. Cardona, “Effect of pressure on the refractive index of Ge and GaAs,” *Physical Review B*, vol. 41, no. 14, pp. 10104–10110, 1990.

[63] G. Theodorou and G. Tsegas, “Piezooptical Properties of GaAs and InP,” *Physica Status Solidi (b)*, vol. 211, no. 2, pp. 847–868, 1999.

[64] J. Gerard and B. Gayral, “Strong Purcell effect for InAs quantum boxes in three-dimensional solid-state microcavities,” *Journal of Lightwave Technology*, vol. 17, no. 11, pp. 2089–2095, 2002.

[65] A. Delan, M. Rennau, S. Schulz, and T. Gessner, “Thermal conductivity of ultra low-k dielectrics,” *Microelectronic engineering*, vol. 70, no. 2-4, pp. 280–284, 2003.

[66] T. Keating, X. Jin, S. Chuang, and K. Hess, “Temperature dependence of electrical and optical modulation responses of quantum-well lasers,” *Quantum Electronics, IEEE Journal of*, vol. 35, no. 10, pp. 1526–1534, 1999.

[67] D. Smith and F. Fickett, “Low-temperature properties of silver,” *Journal Of Research-National Institute Of Standards And Technology*, vol. 100, pp. 119–119, 1995.

[68] J. Piprek, Y. Akulova, D. Babic, L. Coldren, and J. Bowers, “Minimum temperature sensitivity of 1.55 μm vertical-cavity lasers at- 30 nm gain offset,” *Applied physics letters*, vol. 72, p. 1814, 1998.

[69] Y. Varshni, “Temperature dependence of the energy gap in semiconductors,” *Physica*, vol. 34, no. 1, pp. 149–154, 1967.

[70] I. Vurgaftman, J. Meyer, and L. Ram-Mohan, “Band parameters for iii–v compound semiconductors and their alloys,” *Journal of applied physics*, vol. 89, p. 5815, 2001.

[71] Y. Chang, H. Kuo, F. Lai, Y. Chang, C. Lu, L. Laih, and S. Wang, “Fabrication and characteristics of high-speed oxide-confined vcsels using ingaasp-ingap strain-compensated mqws,” *Lightwave Technology, Journal of*, vol. 22, no. 12, pp. 2828–2833, 2004.

[72] K. Satzke, G. Weiser, R. Hoger, and W. Thulke, “Absorption and electroabsorption spectra of an in1-xgaxp1-yasy/inp double heterostructure,” *Journal of applied physics*, vol. 63, no. 11, pp. 5485–5490, 1988.

[73] H. Rong, R. Jones, A. Liu, O. Cohen, D. Hak, A. Fang, and M. Paniccia, “A continuous-wave Raman silicon laser,” *Nature*, vol. 433, no. 7027, pp. 725–728, 2005.

[74] L. Dal Negro, “Light emission from silicon nanostructures: Past, present and future perspectives,” in *Conference on Lasers and Electro-Optics and Conference on Quantum electronics and Laser Science (CLEO/QELS) 2009.*, pp. 1–2, IEEE, 2009.

[75] A. Fang, H. Park, O. Cohen, R. Jones, M. Paniccia, and J. Bowers, “Electrically pumped hybrid AlGaInAs-silicon evanescent laser,” *Optics Express*, vol. 14, no. 20, pp. 9203–9210, 2006.

[76] K. Yu, A. Lakhani, and M. Wu, “Subwavelength metal-optic semiconductor nanopatch lasers,” *Optics Express*, vol. 18, no. 9, pp. 8790–8799, 2010.

[77] M. Nezhad, A. Simic, O. Bondarenko, B. Slutsky, A. Mizrahi, L. Feng, V. Lomakin, and Y. Fainman, “Room-temperature subwavelength metallo-dielectric lasers,” *Nature Photonics*, vol. 4, no. 6, pp. 395–399, 2010.

[78] R. Ma, R. Oulton, V. Sorger, G. Bartal, and X. Zhang, “Room-temperature sub-diffraction-limited plasmon laser by total internal reflection,” *Nature Materials*, vol. 10, no. 2, pp. 110–113, 2010.

[79] D. Van Thourhout, G. Roelkens, R. Baets, W. Bogaerts, J. Brouckaert, P. Debackere, P. Dumon, S. Scheerlinck, J. Schrauwen, D. Taillaert, *et al.*, “Coupling mechanisms for a heterogeneous silicon nanowire platform,” *Semiconductor Science and Technology*, vol. 23, p. 064004, 2008.

[80] F. Niklaus, G. Stemme, J. Lu, and R. Gutmann, “Adhesive wafer bonding,” *Journal of Applied Physics*, vol. 99, p. 031101, 2006.

[81] D. Liang, J. Bowers, D. Oakley, A. Napoleone, D. Chapman, C. Chen, P. Juodawlkis, and O. Raday, “High-quality 150 mm InP-to-silicon epitaxial transfer for silicon photonic integrated circuits,” *Electrochemical and Solid-state Letters*, vol. 12, p. H101, 2009.

[82] D. Liang, A. Fang, H. Park, T. Reynolds, K. Warner, D. Oakley, and J. Bowers, “Low-Temperature, Strong SiO_2-SiO_2 Covalent Wafer Bonding for III–V Compound Semiconductors-to-Silicon Photonic Integrated Circuits,” *Journal of Electronic Materials*, vol. 37, no. 10, pp. 1552–1559, 2008.

[83] D. Pasquariello and K. Hjort, "Plasma-assisted InP-to-Si low temperature wafer bonding," *IEEE Journal of Selected Topics in Quantum Electronics*, vol. 8, no. 1, pp. 118–131, 2002.

[84] L. Coldren, S. Corzine, and L. Coldren, *Diode lasers and photonic integrated circuits*. Wiley New York, 1995.

[85] M. Osinski and J. Buus, "Linewidth broadening factor in semiconductor lasers–An overview," *Quantum Electronics, IEEE Journal of*, vol. 23, no. 1, pp. 9–29, 1987.

[86] T. Baba and D. Sano, "Low-threshold lasing and Purcell effect in microdisk lasers at room temperature," *Selected Topics in Quantum Electronics, IEEE Journal of*, vol. 9, no. 5, pp. 1340–1346, 2003.

[87] K. Srinivasan, M. Borselli, O. Painter, A. Stintz, and S. Krishna, "Cavity Q, mode volume, and lasing threshold in small diameter AlGaAs microdisks with embedded quantum dots," *Optics Express*, vol. 14, no. 3, pp. 1094–1105, 2006.

[88] E. Purcell, "Spontaneous emission probabilities at radio frequencies," *Physical Review*, vol. 69, p. 681, 1946.

[89] H. Yokoyama, "Physics and device applications of optical microcavities," *Science*, vol. 256, no. 5053, p. 66, 1992.

[90] S. Noda, "Seeking the ultimate nanolaser," *Science*, vol. 314, no. 5797, p. 260, 2006.

[91] K. Iga, "Surface-emitting laser-its birth and generation of new optoelectronics field," *Selected Topics in Quantum Electronics, IEEE Journal of*, vol. 6, no. 6, pp. 1201–1215, 2000.

[92] S. Strauf, K. Hennessy, M. Rakher, Y. Choi, A. Badolato, L. Andreani, E. Hu, P. Petroff, and D. Bouwmeester, "Self-tuned quantum dot gain in photonic crystal lasers," *Physical review letters*, vol. 96, no. 12, p. 127404, 2006.

[93] D. Bergman and M. Stockman, "Surface plasmon amplification by stimulated emission of radiation: quantum generation of coherent surface plasmons in nanosystems," *Physical review letters*, vol. 90, no. 2, p. 27402, 2003.

[94] M. Noginov, G. Zhu, A. Belgrave, R. Bakker, V. Shalaev, E. Narimanov, S. Stout, E. Herz, T. Suteewong, and U. Wiesner, "Demonstration of a spaser-based nanolaser," *Nature*, vol. 460, no. 7259, pp. 1110–1112, 2009.

[95] S. Yamashita and M. Makimoto, "Miniaturized coaxial resonator partially loaded with high-dielectric-constant microwave ceramics," *Microwave Theory and Techniques, IEEE Transactions on*, vol. 31, no. 9, pp. 697–703, 1983.

[96] F. Baida, A. Belkhir, D. Van Labeke, and O. Lamrous, "Subwavelength metallic coaxial waveguides in the optical range: Role of the plasmonic modes," *Physical Review B*, vol. 74, no. 20, p. 205419, 2006.

[97] E. Feigenbaum and M. Orenstein, "Ultrasmall volume plasmons, yet with complete retardation effects," *Physical review letters*, vol. 101, no. 16, p. 163902, 2008.

[98] R. Benzaquen, S. Charbonneau, N. Sawadsky, A. Roth, R. Leonelli, L. Hobbs, and G. Knight, "Alloy broadening in photoluminescence spectra of gaxin1-xasyp1-y lattice matched to inp," *Journal of applied physics*, vol. 75, no. 5, pp. 2633–2639, 1994.

[99] H. Tanobe, Y. Kondo, Y. Kadota, K. Okamoto, and Y. Yoshikuni, "Temperature dependence of refractive index in ingaasp/inp for the design of a temperature insensitive arrayed waveguide grating (ti-awg)," in *Lasers and Electro-Optics, 1997. CLEO/Pacific Rim'97., Pacific Rim Conference on*, pp. 283–284, IEEE, 1997.

[100] M. Bayer, T. Reinecke, F. Weidner, A. Larionov, A. McDonald, and A. Forchel, "Inhibition and enhancement of the spontaneous emission of quantum dots in structured microresonators," *Physical Review Letters*, vol. 86, no. 14, pp. 3168–3171, 2001.

[101] I. Maksymov, M. Besbes, J. Hugonin, J. Yang, A. Beveratos, I. Sagnes, I. Robert-Philip, and P. Lalanne, "Metal-coated nanocylinder cavity for broadband nonclassical light emission," *Physical review letters*, vol. 105, no. 18, p. 180502, 2010.

[102] Y. Yamamoto, S. Machida, and G. Björk, "Microcavity semiconductor laser with enhanced spontaneous emission," *Physical Review A*, vol. 44, no. 1, p. 657, 1991.

[103] G. Björk, A. Karlsson, and Y. Yamamoto, "Definition of a laser threshold," *Physical Review A*, vol. 50, no. 2, p. 1675, 1994.

[104] A. Schawlow and C. Townes, "Infrared and optical masers," *Physical Review*, vol. 112, no. 6, p. 1940, 1958.

[105] C. Henry, "Theory of the linewidth of semiconductor lasers," *Quantum Electronics, IEEE Journal of*, vol. 18, no. 2, pp. 259–264, 1982.

[106] G. Björk, A. Karlsson, and Y. Yamamoto, “On the linewidth of microcavity lasers,” *Applied physics letters*, vol. 60, no. 3, pp. 304–306, 1992.

[107] P. Rice and H. Carmichael, “Photon statistics of a cavity-qed laser: A comment on the laser–phase-transition analogy,” *Physical Review A*, vol. 50, no. 5, p. 4318, 1994.

[108] L. Pedrotti, M. Sokol, and P. Rice, “Linewidth of four-level microcavity lasers,” *Physical Review A*, vol. 59, no. 3, p. 2295, 1999.

[109] M. Rosenzweig, M. Mohrle, H. Duser, and H. Venghaus, “Threshold-current analysis of ingaas-ingaasp multiquantum well separate-confinement lasers,” *Quantum Electronics, IEEE Journal of*, vol. 27, no. 6, pp. 1804–1811, 1991.

[110] R. Yan, S. Corzine, L. Coldren, and I. Suemune, “Corrections to the expression for gain in gaas,” *Quantum Electronics, IEEE Journal of*, vol. 26, no. 2, pp. 213–216, 1990.

[111] M. Fukuda, “Current drift associated with surface recombination current in ingaasp/inp optical devices,” *Journal of applied physics*, vol. 59, no. 12, pp. 4172–4176, 1986.

[112] D. Garbuzov, V. Agaev, Z. Sokolova, V. Khalfin, and V. Chalyi, “Recombination processes in InGaAsP/InP double heterostructures emitting at $\lambda = 1 - 1.5\,\mu\text{m}$,” *Soviet Physics – Semiconductors*, vol. 18, no. 6, pp. 665–669, 1984.

[113] R. Hanbury Brown and R. Twiss, “Correlation between photons in two coherent beams of light,” *Nature*, vol. 177, no. 4497, pp. 27–29, 1956.

[114] J. Wiersig, C. Gies, F. Jahnke, M. Aßmann, T. Berstermann, M. Bayer, C. Kistner, S. Reitzenstein, C. Schneider, S. Höfling, *et al.*, “Direct observation of correlations between individual photon emission events of a microcavity laser,” *Nature*, vol. 460, no. 7252, pp. 245–249, 2009.

[115] J. Beattie, “Optical constants of metals in the infra-red âĂŤ– experimental methods,” *Philos. Mag*, vol. 46, pp. 235–245, 1955.

[116] L. Schulz and F. Tangherlini, “Optical constants of silver, gold, copper, and aluminum. ii. the index of refraction n,” *JOSA*, vol. 44, no. 5, pp. 362–367, 1954.

[117] M. Ordal, L. Long, R. Bell, S. Bell, R. Bell, R. Alexander Jr, and C. Ward, “Optical properties of the metals Al, Co, Cu, Au, Fe, Pb, Ni, Pd, Pt, Ag, Ti, and W in the infrared and far infrared,” *Applied Optics*, vol. 22, no. 7, pp. 1099–1119, 1983.

[118] P. Winsemius, F. Kampen, H. Lengkeek, and C. Went, "Temperature dependence of the optical properties of Au, Ag and Cu," *Journal of Physics F: Metal Physics*, vol. 6, p. 1583, 1976.

[119] B. Dold and R. Mecke, "Optische Eigenschaften von Edelmetallen, Übergangsmetallen und deren Legierungen im Infrarot 1. Teil," *Optik*, vol. 22, pp. 435–446, 1965.

[120] A. Erentok, P. Luljak, and R. Ziolkowski, "Characterization of a volumetric metamaterial realization of an artificial magnetic conductor for antenna applications," *Antennas and Propagation, IEEE Transactions on*, vol. 53, no. 1, pp. 160–172, 2005.

[121] B. Wu, W. Wang, J. Pacheco, X. Chen, T. Grzegorczyk, and J. Kong, "A study of using metamaterials as antenna substrate to enhance gain," *Progress In Electromagnetics Research*, vol. 51, pp. 295–328, 2005.

[122] I. Bulu, H. Caglayan, K. Aydin, and E. Ozbay, "Compact size highly directive antennas based on the srr metamaterial medium," *New Journal of Physics*, vol. 7, p. 223, 2005.

[123] R. Ziolkowski, "Antennas and propagation in the presence of metamaterials and other complex media: Computational electromagnetic advances and challenges," *IEICE Trans. Electron*, vol. 88, pp. 2230–2238, 2005.

[124] R. Ziolkowski and A. Kipple, "Reciprocity between the effects of resonant scattering and enhanced radiated power by electrically small antennas in the presence of nested metamaterial shells," *Physical Review E*, vol. 72, no. 3, p. 036602, 2005.

[125] R. Ziolkowski and A. Erentok, "Metamaterial-based efficient electrically small antennas," *Antennas and Propagation, IEEE Transactions on*, vol. 54, no. 7, pp. 2113–2130, 2006.

[126] D. Smith, S. Schultz, P. Markoš, and C. Soukoulis, "Determination of effective permittivity and permeability of metamaterials from reflection and transmission coefficients," *Physical Review B*, vol. 65, no. 19, p. 195104, 2002.

[127] M. Born, E. Wolf, and A. Bhatia, *Principles of optics*, vol. 10. Pergamon Pr., 1975.

[128] J. Stratton, *Electromagnetic theory.* Wiley-IEEE Press, 2007.

[129] P. Yeh, A. Yariv, and E. Marom, "Theory of bragg fiber," *JOSA*, vol. 68, no. 9, pp. 1196–1201, 1978.

[130] Y. Xu, G. Ouyang, R. Lee, and A. Yariv, "Asymptotic matrix theory of bragg fibers," *Journal of lightwave technology*, vol. 20, no. 3, p. 428, 2002.

[131] R. Glauber, "The quantum theory of optical coherence," *Physical Review*, vol. 130, no. 6, p. 2529, 1963.

[132] R. Loudon, *The quantum theory of light.* Oxford University Press, USA, 2000.

[133] F. Dubin, C. Russo, H. Barros, A. Stute, C. Becher, P. Schmidt, and R. Blatt, "Quantum to classical transition in a single-ion laser," *Arxiv preprint arXiv:1002.3621*, 2010.

[134] S. Ulrich, C. Gies, S. Ates, J. Wiersig, S. Reitzenstein, C. Hofmann, A. L "offler, A. Forchel, F. Jahnke, and P. Michler, "Photon statistics of semiconductor microcavity lasers," *Physical review letters*, vol. 98, no. 4, p. 43906, 2007.

[135] Hamamatsu Photonics, "Universal streak camera c10910 series," 2010.